Line Fault Location in Emerging HVDC Transmission Systems

By

Obada Mudalige Kasun Kavinda Nanayakkara

A thesis submitted to the
Faculty of Graduate Studies
of the
University of Manitoba
in partial fulfilment of the requirements for the degree of

Doctor of Philosophy

Department of Electrical and Computer Engineering
University of Manitoba
Winnipeg, Manitoba, Canada

Abstract

The current technology used for location of permanent faults in high voltage direct current (HVDC) transmission lines and cables is based on the travelling-wave principle. This technology has served well for the conventional point-to-point HVDC systems, but is inadequate to handle emerging HVDC transmission configurations such as schemes with very long overhead lines or cables, schemes with a combination of cables and overhead line segments, and multi-terminal HVDC (MTHVDC) schemes. This research investigated accurate and economical ways to locate the faults on dc transmission lines in the aforementioned emerging HVDC transmission configurations.

The accuracy of travelling-wave based fault location methods is highly dependent on the accuracy of measuring the time of arrival of the fault generated travelling waves. Investigations showed that post-processing of detection signals such as the line terminal voltages or surge capacitor currents with continuous wavelet transform yields consistent and accurate fault location results. This method was applied for fault location in HVDC systems with extra-long overhead lines and cables using only the terminal measurements. Simulation results verified the effectiveness of this method in locating the faults in a 2400 km long overhead line and a 300 km long underground cable.

A new algorithm was proposed to locate the faults in a two-terminal HVDC system consisting of multiple segments of overhead lines and cables, using only the terminal measurements. The application of the proposed algorithm was analysed through detailed simulations. Correct performance was verified under various scenarios.

A new algorithm was developed for locating the faults in a star-connected MTHVDC network. This algorithm also required only the terminal measurements. Its effectiveness was verified through detailed simulations.

Finally, a novel measurement scheme for the detection of travelling-wave arrival times was proposed. A prototype of this measurement scheme which uses a Rogowski coil to measure the transient currents through the surge capacitors at the line terminals was implemented. Its effectiveness was validated through field tests in a real HVDC transmission system. The proposed measurement scheme could capture significantly clean signals in an actual substation environment, confirming the practicability of implementing the newly proposed algorithms.

Acknowledgments

I would like to express my sincere thanks to Dr. Athula Rajapakse for his continuous advice, guidance and encouragement throughout the course of this research. I consider myself privileged to have had the opportunity to work under his guidance. I would also like to thank Randy Wachal, Jean Sebestian and Warren Erickson at Manitoba Hydro International for their support with providing resources, technical support and, feedback throughout the research. The technical support received from the technical staff of the University of Manitoba is highly appreciated. I also would like to extend my gratitude to the Advisory Committee members for their comments and feedback to improve the quality of the thesis. The financial support received from the Natural Science and Engineering Research Council, Manitoba Hydro, University of Manitoba Graduate Fellowship (UMGF) and Manitoba Hydro International is gratefully acknowledged.

Special thanks to Gerald R. Brown and Yasas Rajapakse for the comments made to improve my writing. Thanks to the staff and all of my colleagues in the Department of Electrical and Computer Engineering for their continuous encouragement, and for making my years at the University of Manitoba a pleasant experience. This acknowledgement would not be complete without thanking my family. I extend my heartfelt gratitude to my beloved parents, my wife and my brother.

O.M. Kasun Kavinda Nanayakkara

Dedication

To mother, father, brother and wife.

Contents

Front Matter

Abstract i

Contents v

List of Tables x

List of Figures xii

List of Symbols xviii

List of Abbreviations xx

1 Introduction **1**

1.1 Background 1

1.2 Motivation 3

1.3 Objectives 8

1.4 Thesis Overview 8

2 Travelling-wave based fault-location in HVDC systems using wavelet transform **11**

2.1 Introduction 11

2.2 Travelling-wave based fault-location 12

2.3 Wavelet transform 18

2.3.1 Discrete wavelet transform 20

2.4 Wavelet transform applications in power systems 21

3 **DC line fault-location in HVDC systems with an extra-long dc line** **23**
3.1 Introduction 23
3.2 Test networks used for simulation studies 24
3.2.1 HVDC test network with 2400 km long OH dc line 27
3.2.2 HVDC test network with 300 km long UG cable dc line 28
3.3 Wavelet based surge-arrival time detection 29
3.3.1 Proposed fault-location algorithm 30
3.3.2 Discrete Wavelet Transform (DWT) and Continuous Wavelet Transform (CWT) 31
3.3.3 Application to a sample waveform 32
3.3.4 Effect of mother-wavelet type 38
3.3.5 Effect of sampling frequency 40
3.3.6 Determination of propagation velocity 42
3.4 Simulation results for HVDC systems with extra-long dc line 44
3.4.1 Simulation results: HVDC test network - 2400 km OH line .. 44
3.4.2 Simulation results: HVDC test network - 300 km UG cable .. 49
3.5 Effect of the noise in the input signal 54
3.5.1 Performance with noisy inputs: HVDC test network with 2400 km long OH dc line 55
3.5.2 Performance with noisy inputs: HVDC test network with 300 km long UG cable dc line 57
3.6 Concluding remarks 59

4 **Fault-location in conventional HVDC schemes with multiple segments** **61**
4.1 Introduction 61
4.2 Development of the fault-location algorithm for an HVDC transmission system with three line segments 62
4.3 Identification of the faulty line segment 64
4.4 Calibration of the system 66
4.5 Identification of the fault arrival time 67

4.6 Simulated case study 68
4.6.1 Monitored signals 69
4.6.2 Identification: Faulty-line segment using simulation results. 70
4.6.3 Fault-location results 71
4.7 Fault-location with noisy inputs 73
4.8 Fault-location performance for high impedance faults 76
4.9 Theoretical extension of the algorithm to an '*n*'-segment HVDC transmission system 77
4.10 Concluding remarks 79

5 Fault-location in star-connected multi-terminal HVDC schemes 81
5.1 Introduction 81
5.2 Development of the algorithm for fault-location method in star connected three terminal HVDC transmission system 83
5.3 Identification: Correct faulty dc line 87
5.4 Calibration of the system 90
5.5 Identification of the fault arrival time 91
5.6 Simulated case study 93
5.6.1 Simulation model 93
5.6.2 Simulation results 95
5.6.3 Identification of the faulty line segment using the simulation results 97
5.7 Theoretical extension of the algorithm to star-connected network with *n*-number of terminals 98
5.8 Concluding remarks 102

6 Implementation and field validation of a travelling-wave arrival-time measurement scheme 103
6.1 Introduction 103
6.2 Arrangement of the surge-arrival time measurement system 105

6.3 Rogowski coil 106
6.4 Layout of the prototype measurement unit 108
6.4.1 Specifications of the Rogowski coil 109
6.4.2 Surge protection unit and trigger pulse generating circuit .. 113
6.4.3 Data acquisition hardware 115
6.4.4 Specifications: GPS (Global Positioning System) 116
6.4.5 Specifications: Personal computer and the wireless communication module 117
6.4.6 Software for capturing waveforms 119
6.4.7 Rogowski coil placement at the converter station 120
6.5 Summary of the recorded events 122
6.5.1 Lightning strike caused event 126
6.5.2 Identification of a disturbance occurred in pole 3 127
6.6 Simulation study 128
6.6.1 Test network 129
6.6.2 Rogowski coil simulation model 130
6.6.3 Simulation results 131
6.6.4 Rogowski coil and 'Haar' wavelet transform 134
6.6.5 Fault-location results 135
6.7 Concluding remarks 136

7 Conclusions and contributions 138

7.1 Conclusions 138
7.2 Contributions 141
7.3 Suggestions for future research 143

Appendix A: Wavelet Transform 145

A.1 Introduction 145
A.2 Haar wavelet 146
A.3 Example calculation of Haar wavelet coefficients 149

Appendix B: Steps to set up GPS unit **151**

B.1 Enable TIM-TM2 messages in the UART port 151

B.2 Configuration of the GPS unit's UART port data transmitting protocol settings 152

B.3 Enable TIM-TM2 type messages in the GPS unit............................ 152

B.4 Location calibration of the GPS unit 153

References **155**

List of Tables

Table 3-1 - Calibrated propagation constant values for OH line HVDC test network 43

Table 3-2 - Calibrated propagation constant values for UG cable HVDC test network... 43

Table 3-3 - Fault-location results with different CWT coefficients (scales 4, 8, 16, and 32) of the terminal voltages 45

Table 3-4 - Fault-location results with different CWT coefficients (scale 4, 8, 16, and 32) of the surge capacitor currents 46

Table 3-5 - Fault-location results with different DWT coefficients (levels 2, 3, 4, and 5) of the terminal voltages.. 47

Table 3-6 - Fault-location results with different DWT coefficients (levels 2, 3, 4, and 5) of the surge capacitor currents 48

Table 3-7 - Fault-location results with different CWT coefficients (scales 4, 8, 16, and 32) of the terminal voltages 50

Table 3-8 - Fault-location results with different CWT coefficients (scales 4, 8, 16, and 32) of the surge capacitor currents.. 51

Table 3-9 - Fault-location results with different DWT coefficients (levels 2, 3, 4, and 5) of the terminal voltages.. 52

Table 3-10 - Fault-location results with different DWT coefficients (levels 2, 3, 4, and 5) of the surge capacitor currents 53

Table 3-11 - Comparison of fault-location errors with different CWT scales of the terminal voltages with 0.001 pu noise 59

Table 4-1 - Calculated values of x_{F1}, x_{F2}, and x_{F3} for different fault locations 71

Table 4-2 - Predicted fault-location and estimation errors with terminal voltage 72

Table 4-3 - Predicted fault-location and estimation errors with surge capacitor current.. 72

Table 4-4 - Predicted fault-location and estimation errors with terminal voltage contaminated with 0.001 pu noise 74

Table 4-5 - Predicted fault-location and estimation errors with terminal voltage contaminated with 0.01 pu noise 74

Table 4-6 - Predicted fault-location and estimation errors with surge capacitor current contaminated with 0.001 kA noise.. 75

Table 4-7 - Predicted fault-location and estimation errors with surge capacitor current contaminated with 0.01 kA noise.. 75

Table 4-8 - Predicted fault-location and estimation errors for high impedance faults using scale-32 CWT coefficients.. 76

Table 5-1 - Calculated values of x_{T1}, x_{T2} , R_T and X_F for different fault locations 96

Table 6-1 - Self and mutual inductance values of different Rogowski coils 112

Table 6-2 - Serial communication pin assignment 117

Table 6-3 - Comparison of fault-location & surge-arrival time difference of event 1 ... 123

Table 6-4 - Comparison of fault-location & surge-arrival time difference of event 10 . 126

Table 6-5 - Comparison of fault locations 136

Table A-1 – Example of calculated Haar wavelet coefficients....................................... 149

List of Figures

Fig. 2-1 - Bewley lattice diagram for a fault at (a) first half of the line (at A) and (b) second half of the line (at B) 14

Fig. 2-2 - Different types of wavelets 20

Fig. 2-3 - Structure of one-level DWT algorithm 21

Fig. 3-1 - HVDC test networks modeled in PSCAD/EMTDC 26

Fig. 3-2 - HVDC dc line parameters (Left: OH line tower structure and Right: UG cable parameters) 27

Fig. 3-3 - Comparisons of original terminal voltages and surge capacitor currents with conditioned signals when permanent dc line fault occurred at 100 km from the rectifier end 28

Fig. 3-4 - Comparisons of original terminal voltages and surge capacitor currents with conditioned signals when permanent dc line fault occurred at 175 km from the rectifier end (300 km UG cable HVDC test network) 29

Fig. 3-5 - Simplified WT based LFL algorithm 31

Fig. 3-6 - Terminal voltages and surge capacitor currents when permanent dc line fault occurred at (a) 625 km (b) 100 km (c) 2100 km from the rectifier end 33

Fig. 3-7 - DWT and CWT coefficient magnitude values of rectifier end voltage and surge capacitor current when a line to ground fault occurred (625 km away from the rectifier end applied at 2.4 s) 35

Fig. 3-8- DWT and CWT coefficient magnitude values of rectifier end voltage and surge capacitor current when a line to ground fault occurred (2100 km away from the rectifier end applied at 2.4 s) 37

Fig. 3-9 - DWT and CWT coefficient magnitude values of rectifier end voltage and surge capacitor current when a line to ground fault occurred (100 km away from the rectifier end applied at 2.4 s) 38

Fig. 3-10 - Comparison coefficient magnitudes of different mother wavelets 39

Fig. 3-11 - Effect of sampling frequency 41

Fig. 3-12 - Fault-location errors with different CWT coefficients (scale 4, 8, 16, and 32) of the terminal voltages 45

Fig. 3-13 - Fault-location errors with different CWT coefficients (scales 4, 8, 16, and 32) of the surge capacitor currents 46

Fig. 3-14 - Fault-location errors with different DWT coefficients (levels 2, 3, 4, and 5) of the terminal voltages 48

Fig. 3-15 - Fault-location errors with different DWT coefficients (levels 2, 3, 4, and 5) of the surge capacitor currents 49

Fig. 3-16 - Fault-location errors with different CWT coefficients (scales 4, 8, 16, and 32) of the terminal voltage 50

Fig. 3-17 - Fault-location errors with different CWT coefficients (scales 4, 8, 16, and 32) of the surge capacitor currents 51

Fig. 3-18 - Fault-location results with different DWT coefficients (levels 2, 3, 4, and 5) of the terminal voltages 53

Fig. 3-19 - Fault-location results with different DWT coefficients (levels 2, 3, 4, and 5) of the surge capacitor currents 54

Fig. 3-20 - Surge capacitor current and terminal voltage with added noise 55

Fig. 3-21 - Prediction errors for different noise levels in the terminal voltages (Using CWT Scale 4) 56

Fig. 3-22 - Prediction errors for different noise levels in the surge capacitor current measurements (Using CWT Scale 4) 56

Fig. 3-23 - Comparison of prediction errors using different CWT scales for terminal voltage with 0.005pu of noise 57

Fig. 3-24 - Prediction errors for different noise levels in the terminal voltages (Using CWT Scale 16) 58

Fig. 3-25 - Prediction errors for different noise levels in the surge capacitor current measurements (Using CWT Scale 16) 58

Fig. 4-1 - HVDC system with two segments of OH lines and one segment of cable 62

Fig. 4-2 - Three-segment test network 68

Fig. 4-3 - Monitored input signals conditioned by A/D for a fault occurred 16 km away from rectifier terminal 70

Fig. 4-4 - Surge capacitor current and terminal voltage with added white noise 73

Fig. 4-5 - HVDC system with "*n*" number of line segments where fault is in i^{th} segment 77

Fig. 5-1 - (a) Star connected three-terminal HVDC system (b) dc line fault F_1 inside line *AD* 84

Fig. 5-2 - (a) dc line fault F_2 inside the *BD* line (b) dc line fault F_3 inside the *CD* line ... 86

Fig. 5-3 - Faulty segment identification and fault calculation method 89

Fig. 5-4 - Surge detection system for VSC HVDC systems (Redrawn from [46]) 92

Fig. 5-5 - (a) Test network topology & line length (b) Measured terminal dc line current 93

Fig. 5-6 - Tower structure for OH line segments 94

Fig. 5-7 - (a) Monitored dc line current signals conditioned by A/D, (b) Zoomed view of the signals, and (c) the corresponding Scale-32 CWT coefficients for a fault occurred in line BD, 10 km away from B terminal 96

Fig. 5-8 - *N*-terminal VSC HVDC system with all dc lines connect to a common point . 98

Fig. 5-9 - Faulty segment identification and fault calculation method for network with '*N*' terminals 101

Fig. 6-1 - Wave-front detection system 105

Fig. 6-2 - Flexible Rogowski coil 106

Fig. 6-3 - Layout of the experimental setup at one converter station 108

Fig. 6-4 - Technical details of the selected Rogowski coil (Redrawn from [56]) 109

Fig. 6-5 - Test network modeled in PSCAD/EMTDC 110

Fig. 6-6 - Surge capacitor current after applying a fault 1 km from rectifier (a) complete view of the two end surge capacitor currents (b) zoomed in view to show the inverter end surge capacitor current 110

Fig. 6-7 - Comparison of Rogowski coil output voltages (a) Complete view (b) Zoomed in view to clearly show the first slope 112

Fig. 6-8 - Installed Rogowski coil at Dorsey converter station 113

Fig. 6-9 – (a) Surge-protection and (b) trigger-pulse generating circuits as appear in the experimental unit 113

Fig. 6-10 - Multifunction Data Acquisition hardware NI USB-6361 from National Instruments.. 115

Fig. 6-11 - Pin layout of NI USB 6361 115

Fig. 6-12 - GPS unit: EVK-6T-0 u-blox 6 Evaluation Kit with Precision Timing......... 116

Fig. 6-13 - Front and real panels of the GPS unit 116

Fig. 6-14 - IPn3G - 3G Cellular Ethernet/Serial/USB Gateway.................................... 117

Fig. 6-15 - ARK-3360F Embedded Box PC from AdvanTech 118

Fig. 6-16 - Simplified flow diagram of the developed software.................................... 119

Fig. 6-17 - Map of the Nelson River HVDC Transmission System with installed locations of the fault locators 121

Fig. 6-18 - Placement of the experimental unit in Nelson River HVDC line (Under normal operation of Nelson River system) 121

Fig. 6-19 - Venn diagram view of recorded events 122

Fig. 6-20 - Histogram view of the fault-location from Dorsey in Kilometers................ 122

Fig. 6-21 - Captured waveform from the experimental unit (First recorded event) 123

Fig. 6-22 - Colour map view of captured Rogowski coil voltages in volts 124

Fig. 6-23 - Captured Rogowski coil pre fault voltages for selected events 125

Fig. 6-24 - Captured voltages for event 10 126

Fig. 6-25 - Fault-location on the map obtained with Manitoba Hydro's lightning strike locator 127

Fig. 6-26 - Nelson River HVDC system dc tower operation under normal condition ... 127

Fig. 6-27 - Event 3 occurred on pole 3 128

Fig. 6-28 - Simulation model 130

Fig. 6-29 - Equivalent circuit of the Rogowski coil 130

Fig. 6-30 - Surge capacitor currents after dc line fault occurred 1 km from the rectifier end. In the second graph y-axis is expanded to show the details of inverter side waveform 132

Fig. 6-31 - CWT coefficient magnitudes and Rogowski coil voltage magnitude obtained from surge capacitor currents at the terminals for ground fault occurred on the dc line 1 km from the rectifier station. 133

Fig. 6-32 - Frequency response of the Rogowski coil 135

Fig. A-1 - Haar wavelet and its shifting process 147

Fig. A-2 - Haar wavelets at different scales 148

Fig. A-3 – Comparison of Haar wavelet and its scale 32 version with an example surge capacitor current signal 148

Fig. A-4 – Input signal used in example calculation 150

Fig. A-5 – Calculated Haar detail coefficients at 3 levels 150

Fig. B-1 - Configure GPS message protocol 151

Fig. B-2 - Configure port protocol settings 152

Fig. B-3 - Enable TIM-TM2 messages 153

Fig. B-4- GPS survey-in 154

List of Symbols

X	Fault location
L	Total dc line length
T_1	Inverter terminal surge-arrival time
T_2	Rectifier terminal surge-arrival time
V or v	Travelling-wave propagation velocity
$td1$	Time difference: Arrival of first and the second surges at the first side
$td2$	Time difference: Arrivals of the initial surges at two sides of the line
$f(t)$	Input signal
$\psi(t)$	Mother wavelet
a	Scaling factor
b	Shifting factor
n	Any integer value
k	Sample number
td	Difference between the initial surge-arrival times at the two terminals
λ	Inverse of propagation velocity
R	Ratio between the smaller and the larger values of the estimated fault locations
V_0	Induced terminal voltage output of Rogowski coil
μ_0	Permeability of free space (4π×10−7 H·m−1)

A	Area of one loop of Rogowski coil
N	Number of helical turns in Rogowski coil
l	Length of the winding of the Rogowski coil
ML	Mutual inductance
SL	Self inductance
Z_l	Load resistance
SR	Coil resistance
C_l	Coil capacitance
f	Frequency
$\boldsymbol{j}$	Unit imaginary number

List of Abbreviations

ac	Alternating Current
A/D	Analog to Digital Conversion
AI	Analog Input
ANN	Antenna
COM	Serial Communication Port
CWT	Continuous Wavelet Transform
DAQ	Data Acquisition Hardware
dc	Direct Current
DI	Digital Input
DSP	Digital Signal Processor
DWT	Discrete Wavelet Transform
EMT	Electromagnetic Transient
EMTP	Electromagnetic Transient Program
FORX	Fibre Optic Receiver
FOTX	Fibre Optic Transmitter
FPGA	Field-programmable Gate Array
GND	Ground
GPS	Global Positioning System

GSM Global System for Mobile

HPF High Pass Filter

HVDC High Voltage Direct Current

IEEE Institute of Electrical and Electronics Engineers

IGBT Insulated Gate Bipolar Transistor

LCC Line Commutated Converter

LFL Line Fault Locator

LPF Low Pass Filter

MTHVDC Multi-terminal High Voltage Direct Current

MTS Manitoba Telecom Services Inc

NI National Instruments Corporation

NMEA National Marine Electronics Association

OH Overhead

PC Personal Computer

PSCAD Power System Computer Aided Design

SIM Subscriber Identity Module

TTL Transistor–Transistor Logic

UART Universal Asynchronous Receiver/Transmitter

UBX U-blox GPS Communication Protocol

UG Underground

UHVDC Ultra High Voltage Direct Current

USB Universal Serial Bus

UTC Coordinated Universal Time

VSC	Voltage Source Converter
WT	Wavelet Transform

Chapter 1

Introduction

1.1 Background

High Voltage Direct Current (HVDC) technology is an economical solution to transmit electrical power over long distances. As the demand for power grows in countries that are rapidly industrializing, many new HVDC transmission schemes are being built, and the operating boundaries of HVDC transmission systems are being pushed to new heights: voltages of ±800 kV and transmission lengths over 2000 km are now a reality. Several 800 kV Ultra High Voltage Direct Current (UHVDC) transmission schemes (Yunnan-Guangdong, Xiangjiaba-Shanghai, etc.) are under construction in China [1]. HVDC transmission systems with extra-long overhead (OH) lines such as the 2500 km long Porto Velho-São Paulo HVDC system [2] and extra-long underground (UG) and submarine cables such as the 580 km long NorNed HVDC system [4] are under construction. The Basslink HVDC system [3] which has a 295 km long cable is already in operation. Often, HVDC lines have to cross various geographical formations such as bodies of water and such schemes use transmission systems that are combinations of overhead (OH) lines and underground (UG) cables. The Basslink HVDC system [3] is an example of such a system.

Another development is the Multi Terminal HVDC (MTHVDC) topology. A conventional HVDC transmission scheme transmits electricity from one point to another, using two converter stations placed at the terminals. A Multi Terminal HVDC (MTHVDC) scheme is an HVDC transmission system with more than two terminals with converters installed at all terminals. Therefore an MTHVDC is more complex than an ordinary point-to-point transmission. In particular, the control system is more elaborate and the telecommunication requirements between the stations become larger.

Consideration of MTHVDC for interconnection of offshore wind farms generated a significant interest on the subject. In addition to the interconnection of offshore wind farms, multi-terminal dc schemes have been proposed for [5],

- Underground urban sub-transmission systems
- As a backbone for distributed and renewable generation systems
- Shipboard power supplies

Furthermore, the technology used in HVDC convertor stations is also changing from traditional thyristor-based Line Commutated Convertor (LCC) technology to new Insulated Gate Bipolar Transistor (IGBT) based Voltage Source Convertor (VSC) technologies. They are commercially available in different brand names such as HVDC Light® by ABB [6], HVDC MaxSine® by Alstom [7] and HVDC PLUS by Siemens [8] . Although classical MTHVDC schemes use line commutated converters, Voltage Source Converter (VSC) technology is considered more suitable for making MTHVDC.

1.2 Motivation

According to reliability statistics of HVDC systems during 2009-2010 found in [9], it is clear that a certain percentage of forced energy outages occur due to transmission line or cable related disturbances. Minimizing the outage time is critical both in terms of reliability and loss of revenues, since HVDC systems are used to transport large amounts of power. Furthermore, unavailability of an HVDC transmission system can impose limitations on the operation of the rest of the system. Therefore, fault-location is of paramount importance once a permanent fault occurs in an HVDC transmission line.

When a temporary fault occurs, the HVDC line protection system detects and extinguishes the fault by means of control actions as mentioned in [10] and [11], so that the system can be restored as fast as possible. However, in case of permanent faults, the system may need to terminate the power transmission until the necessary repairs are performed on the line. Broadly two types of dc lines: overhead lines and cables are used in HVDC systems. The causes for dc line faults can be due to electrical failures and mechanical failures. Mechanical failures are typical in submarine (underwater) cables and are caused by a trawler anchor hooked to the cable or the fishing nets [12]. In overhead line systems, failures are mostly due to flashovers and rarely due to tower collapses. The most common cause for permanent damage to insulators in an overhead line is a lightning surge that is high enough to cause a line flashover. Occasionally, flashover is caused by normal voltage on account of the excessive contamination due to pollution and damaged insulations. As regards to the dc line fault type, line-to-ground faults are the most frequent in an HVDC system due to the tower structure, and pole-to-pole faults are rare since typically the right of way is wider compared to the ac counterpart.

Location of a fault, as accurately as possible, is important to send the repair crews to the right point on the HVDC line. The most fundamental way of fault location is by foot patrols or by patrols equipped with different transportation means and vision aids. Such means of inspections are considered time consuming and not feasible in HVDC systems with long overhead lines or underground/submarine cable systems. Automatic fault locators are used to pinpoint the fault position by processing the voltage and/or current waveform values. The calculations required for the fault location can be performed in off-line mode since the results of the calculations are for the operator's use. This implies that the speed of fault location calculations can be measured in seconds or even minutes [13]. This type of fault location can be classified into the following main categories:

1. Techniques based on resistance calculation performed using voltage and current measurements.
2. Knowledge-based approaches.
3. Techniques based on injection of current signals.
4. Techniques based on travelling-wave phenomenon.

Impedance based methods (e.g. [14] and [15]) typically require line parameters, and the voltage and current measurements during the fault. Reference [14], presents an impedance based method which used post fault voltage and current data together with dc line parameters to locate faults. In this method, the distributed parameter line model is used and hence the voltage distribution over the line is obtained from the voltage and current measurements at the two terminals. Using the voltage distribution, the fault point is identified. These methods typically require a lower signal sampling rate than in the travelling-wave based methods, and therefore can be implemented using data from the existing transient fault recorders at the converter stations. However these methods have a lower accuracy: for example in [14] accuracy is ± 2.5 km. Also, the impedance based fault location methods require accurate line parameters which in case of cables may change over a period of time. Moreover, these methods are difficult to apply in systems with several non-homogeneous line segments.

Knowledge-based fault-location methods are mostly based on artificial neural network, fuzzy-set theory and expert systems [13]. Reference [16] presents how knowledge-based systems can be used in fault identification in HVDC systems. These knowledge-based fault-location methods are mostly suitable in identifying the fault type rather than the exact fault location. The main drawbacks are the requirement of prior training and poor fault location accuracy with minor change in the operating condition. The main advantage of the knowledge based methods is the shorter calculation time; therefore, they can be incorporated in protection relays [13].

Current injection type fault location is based on the travelling-wave principle, and is typically carried out to locate underground cable faults. This type of fault locators requires isolation of the dc line and injecting a certain high frequency signal with a known waveform signature. The current injection type of fault locators are mostly used in ac distribution systems and it is sometimes used in dc cable based HVDC systems.

Travelling-wave based fault-location is the most popular and the most accurate method currently available. Fault-location using the travelling-wave principle is simple and robust. Depending on whether the measurements at the remote terminal of the line are used or not, travelling-wave based line fault-location methods are classified into two categories: (i) two-terminal method and (ii) single-terminal method. The two-terminal method which makes use of only the initial surge generated by the fault is more reliable than the single-terminal method which requires the use of secondary reflections. If the two-terminal measurements are fully synchronized, the difference between the surge-arrival times at the two terminals can be used to determine the fault-location, given that the propagation velocity of the surge is known. With the development of Global Positioning System (GPS) which facilitates accurate time synchronization of the measurements at the two terminals, the two-terminal method has become the most widely used technique. The main disadvantages of the two-terminal methods are the requirements for high sampling frequency transducers capable of capturing travelling waves and the very accurate time synchronization of measurements. More details on this method are discussed in Chapter 2.

HVDC transmission systems with extra-long OH lines (e.g. 2500 km long Porto Velho-São Paulo HVDC system [2]) and HVDC systems with extra-long UG cables (e.g. 295 km long Basslink HVDC system [3]) are under consideration. Accurate fault location in such extra-long dc lines is a challenging task. Fault-location in extra-long HVDC systems is currently achieved with the help of repeater stations. Installation of extra hardware at the repeater stations, which are required to locate line faults using the existing technology, increases the cost of these transmission projects.

Due to high demand in HVDC systems, dc lines have to cross various geographical areas. Therefore, OH lines combined with UG cables become an intricate part of the HVDC system (e.g. [17] and [18]). Existing travelling-wave-based dc line fault-location methods have been developed for the HVDC systems with only overhead transmission lines. Fault-location in HVDC systems with a combination of overhead lines and cables has been generally achieved by considering the overhead sections only. However, this practice is expensive as it requires duplicate installation of additional hardware for each overhead section.

Multi-terminal voltage-source converter (VSC) based HVDC technology is now commercially available and expected to be widely used for the interconnection of off-shore wind farms, as well as in underground urban sub-transmission systems, shipboard power supplies and on shore renewable generation systems [5]. If a line fault occurs in a multi-terminal HVDC scheme, the primary protection must activate and isolate the faulted line segment. Some methods to identify the faulty line in a multi-terminal VSC HVDC network with mesh topology are explained in [5] and [19]. These methods based on current and voltage measurements at the converter terminals have been primarily developed for protection purposes. However, in the case of a permanent dc line fault, as mentioned above, determination of the exact fault-location is essential for carrying out the repairs. This can be achieved by using the existing two-terminal travelling-wave based fault locators with synchronized measurements, if fault locators are placed at all the terminals and at the common point. However, installing a fault locator at every connection point requires additional equipment as well as communication infrastructure, and therefore incurs additional costs.

On the grounds of aforementioned reasons, this thesis focuses on elaborating on the problems associated with fault-location in HVDC systems with extra-long dc lines, with several non-homogeneous segments of dc lines and star-connected networks, and provides new exclusive algorithms and field validation data.

1.3 Objectives

The overall goal of this research is to improve the accuracy of travelling-wave based fault-location technology for HVDC transmission systems, extend the applicability of technology for emerging new HVDC topologies, and field validate a transducer to capture the travelling waves. The following specific objectives were fulfilled to achieve the overall goal:

1. Development of improved methods to detect travelling waves and measure the travelling-wave arrival times
2. Identification of suitable input signals which can be used to determine the travelling-wave arrival times and the required signal conditioning needs
3. Development of fault-location algorithms that are suitable for the following HVDC transmission system configurations:
   I. Classical two-terminal HVDC schemes with very long (> 2000 km) OH lines
   II. Classical two-terminal HVDC schemes with very long (> 300 km) UG cables
   III. Classical two-terminal HVDC schemes with segments of OH lines and UG cables
   IV. VSC based star connected multi-terminal HVDC schemes
4. Identification of the hardware specifications for implementation of the fault locator in a classical HVDC system.

1.4 Thesis Overview

The thesis covers five areas: (1) review of the existing travelling-wave based fault-location technology used in HVDC systems, (2) the author's contributions on dc line fault-location in extra-long HVDC lines and cables, (3) HVDC systems with several dc line segments, and (4) multi-terminal HVDC systems, and (5) hardware implementation details. This chapter provides an introduction giving the background information with the problem statement and the research objectives.

A background to the travelling-wave based fault-location concept is provided in Chapter 2. A brief introduction to the wavelet transform is given and some example applications of the wavelet transform in the power system field is presented. Then a wavelet transform based surge detection method is explained. The effects of the sampling frequency and mother wavelet type are discussed.

In Chapter 3, fault-location in a 2400 km long overhead HVDC line and a 300 km long underground HVDC cable using the two-terminal travelling-wave method are investigated. The relative merits of using the terminal voltage and the terminal surge capacitor current for the detection of travelling waves are examined. Practical considerations such as the influences of noise, A/D conversion precision and the fault impedance on the fault-location accuracy were also investigated.

In Chapter 4, a novel method is proposed for locating faults in an HVDC system with a combination of overhead lines and cables by using only the terminal measurements. The method can determine the faulted line segment and the exact fault-location.

Chapter 5 presents a new fault-location method for locating faults in star-connected Multi terminal HVDC systems. The method can find the faulty line segment and calculate the distance to the fault from a terminal using only the surge-arrival times measured at the terminal.

Details about the implementation of an experimental line fault locator are presented in Chapter 6. The proposed hardware specifications and measurement transducer usage are validated by installing experimental data acquisition units at the Nelson River HVDC system. Disturbances that occurred during July to September 2012 were monitored and analysed in detail.

Finally in Chapter 7, conclusions and a summary of the contributions are presented.

Chapter 2

Travelling-wave based fault-location in HVDC systems using wavelet transform

2.1 Introduction

The travelling-wave based fault-location principle, which utilizes the propagation times of the voltage and current travelling waves generated on a transmission line when a fault occurs, is well known. Although direct application of this principle is challenging in the highly branched and meshed ac networks, it has been successfully applied to transmission line fault-location in the conventional HVDC systems [20] - [28], which have only two terminals. The key requirement to improve the accuracy of fault-location in long lines is precise detection of the wave-front arrival times.

In many of the recently published research [26]-[28], surge-arrival times have been detected using the Discrete Wavelet Transform (DWT) coefficients of the measured signals. Wavelet transform works well for analyzing transients in signals because of its simultaneous time and frequency localization capabilities. Availability of software tools and a lower computational burden have made the discrete version of the wavelet transform, DWT, the common choice for implementation of these fault-location algorithms.

Compared to DWT, continuous-wavelet transform (CWT) provides more a detailed and continuous analysis of a fault transient [29]. In CWT, the analyzing wavelet is shifted smoothly along the time axis of the input signal. Therefore, CWT coefficients have better time resolution, which is very important to have high accuracy in travelling-wave based dc line fault-location.

This chapter introduces the Travelling-wave based fault-location concept, and Wavelet transform and its applications. It also explains mathematical details of the Discrete Wavelet Transform (DWT) and Continuous Wavelet Transform (CWT).

2.2 Travelling-wave based fault-location

Travelling-wave based fault-location can be applied to both ac and dc transmission lines. The flashover at the fault point launches two waves that travel in opposite directions away from the fault. If the transients appearing at either end of the line are captured, they can be analysed to determine the fault position. HVDC transmission lines are ideal for the application of travelling-wave theory as they are mainly used for point to point transmission.

There are two types of fault-location algorithms differentiated according to the number of measurement locations used: (i) two-ended method and (ii) one-ended method. Travelling-wave based fault-location in ac transmission lines is clearly described in IEEE standard C37.114-2004 [30]. However, there is no such standard for fault-location in dc transmission lines.

Referring to the lattice diagram shown in Fig. 2-1, the distance to the fault-location from the left hand side end, X, is calculated by using the two ended method as

$$X = \frac{[L + (T_1 - T_2) \times V]}{2} \quad \text{Eq. 2-1}$$

Where L is the total length of the transmission line, T_1 is the inverter terminal surge-arrival time, T_2 is the rectifier terminal surge-arrival time, and V is the propagation velocity of the travelling surge. Eq. 2-1 is valid for both scenarios shown in Fig. 2-1, i.e., when the fault is on the first half or second half of the transmission line.

The two-ended method requires the determination of the difference between the times of arrival of fault-generated waves at two line terminals, $(T_1 - T_2)$. In order to accurately determine the wave arrival time difference, measurements at the two ends need to be time synchronized. Data measured at the two ends must be brought to a common point so that the fault position can be determined. Global Positioning System (GPS) provides a way of time synchronization of measurements at different geographical locations with accuracies better than 1 μs over the entire surface of the Earth, 24 hours a day [13], [30].

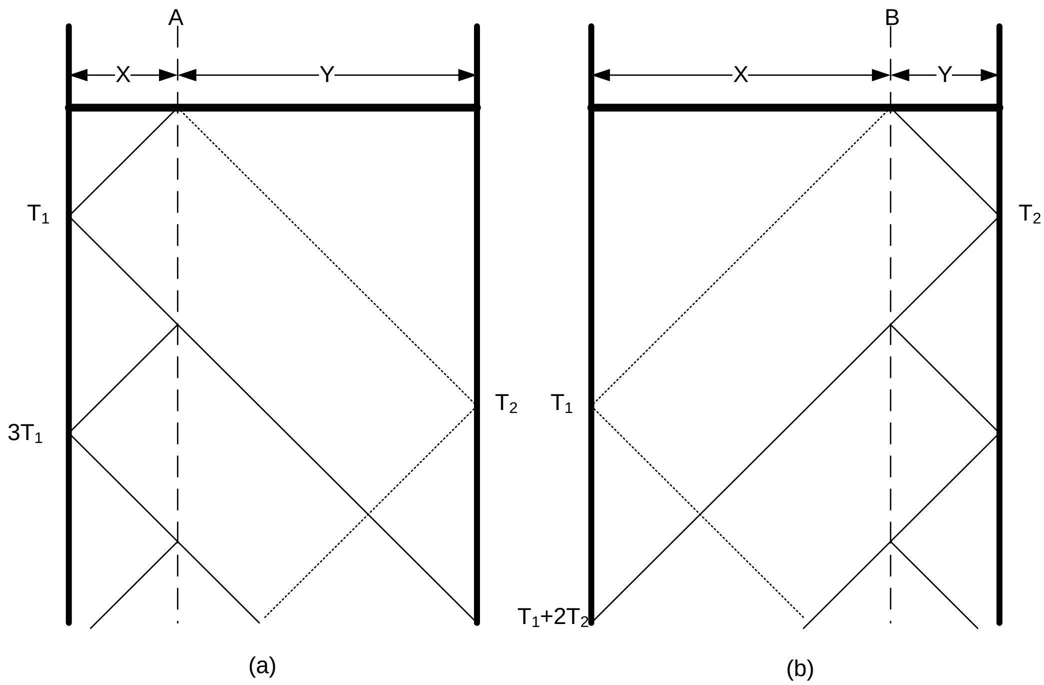

Fig. 2-1 - Bewley lattice diagram for a fault at (a) first half of the line (at A) and (b) second half of the line (at B)

The travelling-wave propagation velocity *V* is a parameter in Eq. 2-1 and the value of *V* can change from scheme to scheme and with aging, especially in cables. If secondary reflections are used, the travelling velocity of the signal can be excluded from the evaluation process given that the fault is permanent and an accurate surge-arrival time detection method is available. In order to eliminate the travelling-wave velocity from the calculations, the time between the arrival of the first and the second surges must be measured. The first surge starts at the inception of the fault whereas the second surge corresponds to the reflection at the remote end or fault point. If the fault occurs between the fault locator and the midpoint of the protected line, the first reflection from the fault point arrives at the fault locator before any other reflection from the remote end as shown in Fig. 2-1 (a). On the other hand, if the fault occurs between the midpoint and remote end bus, reflections from the remote end may arrive at the fault locator before the first reflection from the fault point, as shown in Fig. 2-1(b).

For a fault in the first half of the line (*X*<*Y*) as shown in Fig. 2-1(a), the following relationship can be derived;

$$td_1 = 3T_1 - T_1 = 2T_1 = 2\left(\frac{X}{V}\right) \quad \text{Eq. 2-2}$$

$$td_2 = T_2 - T_1 = \left(\frac{Y}{V}\right) - \left(\frac{X}{V}\right) \quad \text{Eq. 2-3}$$

$$L = X + Y$$

Where, td_1 is the time difference between the arrival of the first and second surges at the first side; td_2 is the time difference between the arrivals of the initial surges at two sides of the line; V is the travelling-wave velocity; L is the total length of the line.

By eliminating V, the distance to the fault from the left hand side can be evaluated using Eq. 2-2 and Eq. 2-3 as;

$$X = L \times \frac{\left(\frac{1}{2}\right)}{\left(1 + \left[\frac{td_2}{td_1}\right]\right)} \quad \text{Eq. 2-4}$$

This method could be applied to all fault types provided that the two-terminal recordings are synchronized in time. The arrival time of the transient peaks at each end of the line only depends on the fault distance and propagation velocity. Furthermore, for a fault in the second half of the line at B (X>Y) as shown in Fig. 2-1(b), the relationship in

Eq. 2-7 can be derived. Eq. 2-4 and Eq. 2-7, which are independent of the velocity of propagation, can be used to calculate the fault distance X

$$td_1 = (T_1 + 2T_2) - T_1 = 2T_1 = 2\left(\frac{Y}{V}\right) \qquad \text{Eq. 2-5}$$

$$td_2 = T_1 - T_2 = \left(\frac{X}{V}\right) - \left(\frac{Y}{V}\right) \qquad \text{Eq. 2-6}$$

$$X = L \times \frac{\left(1/2 + \left[td_2/td_1\right]\right)}{\left(1 + \left[td_2/td_1\right]\right)} \qquad \text{Eq. 2-7}$$

On the other hand, the single-ended method does not require remote end synchronization. It makes use of fault induced spikes and one reflected surge to determine the fault-location. However, in this case, due to the lack of any other time reference, all time measurements will be with respect to the instant when the fault generated transient is first detected. For a fault in the first half of the line (X<Y) as shown in Fig. 2-1(a);

$$td_1 = 3T_1 - T_1 = 2T_1 = 2\left(\frac{X}{V}\right)$$

$$X = \frac{V}{2} \times td_1 \qquad \text{Eq. 2-8}$$

For a fault in the second half of the line (X>Y) as shown in Fig. 2-1(b);

$$td_1 = (T_1 + 2T_2) - T_1 = 2T_1 = 2\left(\frac{Y}{V}\right)$$

$$Y = L - X$$

$$X = L - \frac{V}{2} \times td_1 \qquad \text{Eq. 2-9}$$

Eq. 2-8 and Eq. 2-9 can be used to calculate the fault distance *X*. In this case both equations are dependent of the velocity of propagation. The one-ended principle is more cost effective to be realized, but its reliability is not satisfactory due to the complexity of fault reflected surge discrimination. The two-ended principle is more reliable than the one-ended method as it only makes use of the initial fault generated surges.

The following equipment is necessary to locate faults using the two-terminal travelling-wave method [30]:

1. Accurate time stamping device (GPS) on both ends of the line.
2. An appropriate sensor to detect the voltage travelling-waves or current travelling-waves, depending on the parameter used.
3. A communications circuit is required to transmit the time stamped data back to a central location.
4. A computer capable of retrieving the remote time stamp data or extracting wave front arrival times from the appropriate waveforms, and performing the required calculations to determine the fault-location using Eq. 2-1.

The accuracy of travelling-wave based fault-location directly depends on the accuracy of measuring the relevant surge-arrival time differences. Since the velocity of propagation of travelling waves in transmission lines is close to the speed of light, an error of one micro-second in the time difference measurement translates into approximately 300 m error in the fault-location. Detection of the precise arrival times of the wave fronts is very important. Transducer bandwidths and signal sampling rates are thus a concern in practical implementation. If using the one ended measurements, distinguishing between travelling waves reflected from the fault and from the remote end of the line is a problem [30].

However, the developments in transducer technology and broad bandwidth sampling capability have eased some of the practical difficulties of travelling-wave based methods for fault-location. Furthermore, modern signal processing techniques such as wavelet transform have shown to be useful in locating the transients such as travelling-wave fronts superimposed on signals.

2.3 Wavelet transform

The wavelet transform is a linear transformation similar to the Fourier transform. However, it is different from the Fourier transform because it allows the time localization of different frequency components of a given signal [31].

The continuous wavelet transform (CWT) of a signal *f(t)* is the integral of the product between *f(t)* and the daughter-wavelets, which are time translated and scale expanded or compressed versions of a function $\psi(t)$, which is called the mother-wavelet. Therefore, CWT of a signal *f(t)* with respect to the mother wavelet $\psi(t)$ is written as

$$CWT(f(t);a,b) = \int_{-\infty}^{\infty} f(t)\psi^{*}{}_{a,b}(t)dt \qquad \text{Eq. 2-10}$$

$$\psi^{*}{}_{a,b}(t) = \frac{1}{\sqrt{a}}\psi\left(\frac{t-b}{a}\right) \qquad \text{Eq. 2-11}$$

Where $\Psi_{a,\ b}\,(t)$ is a continuous function in both the time domain and the frequency domain called the mother-wavelet which is defined by Eq. 2-11 and * represents operation of complex conjugate. "*a*" is a scaling factor and "*b*" is the shifting factor.

If the factors “*a*” and “*b*” are changed in a discrete manner, the wavelet transform is called discrete wavelet transform (DWT). Often “*a*” and “*b*” are changed in a didactic fashion. The scale “*a*” is changed as powers of *2*, i.e. $a_0=2^0=1$, $a_1=2^1=2$, etc. and in general, $a_j=2^j$ [13] where *j* is referred to as the level of details. The value of *b* is also changed in a discrete manner as powers of 2: at j^{th} detail level, the time shifts are changed as $b_0=2^j\times 0=0$, $b_1=2^j\times 1=2^j$, etc. and generally: $b_n=2^j\times n$ [13]. DWT of the sampled waveform *f(k)* can be expressed as:

$$DWT_{x_{jn}} = \sum_{k=0}^{M-1} f(k)\psi_{jn}^{*}(k) \qquad \text{Eq. 2-12}$$

$$\psi_{jn}(k) = 2^{-\frac{j}{2}}\psi\left(2^{-j}k - n\right) \qquad \text{Eq. 2-13}$$

Where *k* is the sample number of *f(t)*, *M* is the total number of signal samples of non-zero values of $\psi_{jn}(k)$ for the time period. The wavelet function after substituting the generalized values of ‘*b*’ and ‘*a*’ (in terms of *j* and *n*) is shown in Eq. 2-13.

A mother-wavelet is an oscillatory function with amplitude that begins at zero, increases, and then decreases back to zero. The shapes of several mother-wavelet types are shown in Fig. 2-2. The wavelets in *Daubechies (db)* family are commonly used in power system applications. The *Haar* mother-wavelet, which is also called *db2* mother-wavelet, is considered the simplest mother-wavelet type available. Therefore, it is expected to be computationally less demanding.

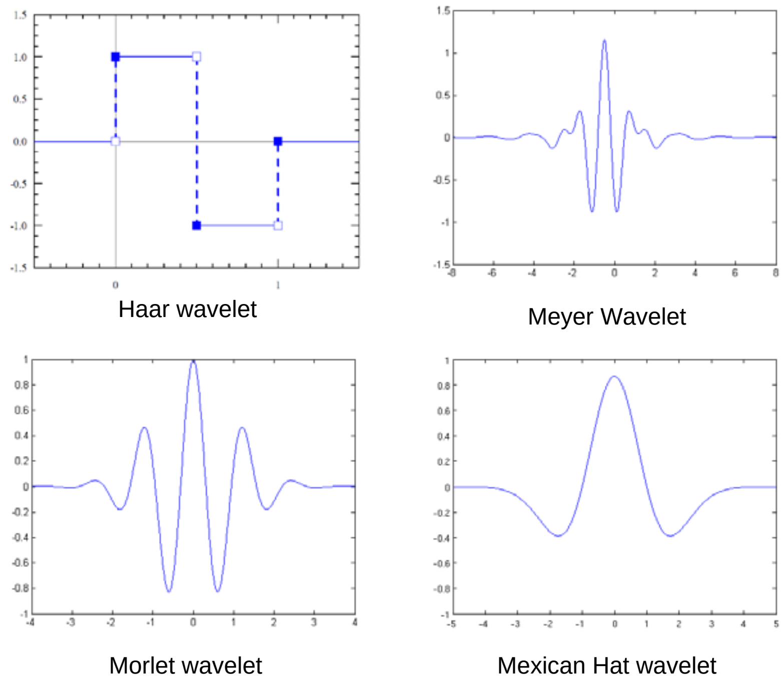

Fig. 2-2 - Different types of wavelets

2.3.1 Discrete wavelet transform

Discrete wavelet transform (DWT) has been used to detect incoming travelling waves in many fault-location algorithms [26], [27], [28]. This has probably been motivated by the computational efficiency of DWT over its continuous version. The DWT, which is also considered as multi-resolution analysis, differs from *continuous wavelet transform* (CWT) with clear steps in the time-frequency plane [22]. The DWT can be used to decompose the input signal into multiple frequency bands and this can be implemented efficiently as a filter bank as shown in Fig. 2-3 under DWT decomposition [22]. Only a single level is shown in Fig. 2-3 but this can be extended for a series of levels by substituting the approximation value with the input signal of the next level.

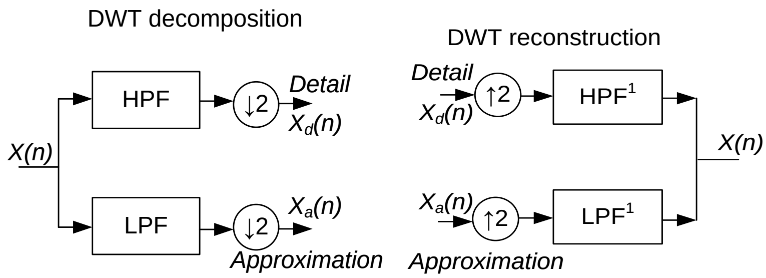

Fig. 2-3 - Structure of one-level DWT algorithm

This implementation is commonly known as *Mallat tree* algorithm and consists of a series of low-pass filters *(LPF)* and their dual high pass filters *(HPF)*. The circle with a downward arrow behind 2 denotes down sampling by a factor of 2. The output $x_d(n)$ is called the detail wavelet coefficients while the output from the last low pass filter is referred to as the approximation wavelet coefficient.

It is possible to obtain the original signal $x(t)$ through wavelet series reconstruction. The reconstruction can also be carried out efficiently using a tree algorithm as shown in Fig. 2-3 under DWT reconstruction. The filters HPF^1 and LPF^1 are the inverse filters of *HPF* and *LPF* respectively. In Fig. 2-3, the circles with an upward arrow behind 2 denotes up sampling by a factor of 2.

2.4 Wavelet transform applications in power systems

Wavelet analysis is widely used in image processing, medical imaging, communication and acoustics [24]. Wavelet transform is suited for the analysis of signals containing short-lived high frequency disturbances superposed on lower frequency continuous waveforms [31]. Thus, in power systems, wavelet analysis is used for the detection of signal features such as transients in the identification of power quality disturbances. The multi-resolution properties of wavelet transform are useful for analyzing fault transients that contain localized high frequency components superposed on power frequency signals [31].

The wavelet transform can be used for detecting travelling waves in the line fault-location. As mentioned earlier, in travelling-wave based fault-location systems, accurate detection of the travelling-wave arrival time is very important. Wavelet coefficients of the recorded voltage and current signals can be used to recognize the arrival of wave fronts at the measuring point. Usually the discrete wavelet transform is applied to the detection signal yielding the wavelet coefficients in selected levels. The correct fault position will be determined by analyzing the relationship between the characteristics of the transient sequences. Each transient signal is identified with a synchronizing time at its local maximum value. The first local maximum represents the arrival of the initial wave generated by the fault; the second local maximum represents the arrival of the first reflected wave and so on.

Chapter 3

DC line fault-location in HVDC systems with an extra-long dc line

3.1 Introduction

With the rapid development of HVDC technology, HVDC transmission systems with extra-long overhead (OH) lines or underground (UG) cables are coming into existence. The 2500 km long Porto Velho-São Paulo HVDC system [2] and the 295 km long Basslink HVDC system [3] are good examples. Accurate fault-location in such extra-long HVDC transmission lines or cables is a challenging task because the travelling waves get attenuated along the line.

Fault-location in such extra-long HVDC systems is currently achieved by sectioning the line into two or more segments and installing repeater stations [21] at segment boundaries. Installation of extra fault-location hardware at the repeater stations increases the cost of these transmission projects.

This chapter investigates the possibility of accurately locating the faults on such extra-long OH lines and UG cables only using terminal measurements. It explores how the wavelet coefficients of the measured signals, obtained using the DWT and CWT discussed in the previous chapter, can be used to more accurately detect the travelling wave arriving times at the terminals. All studies were carried out with detailed models of HVDC converters, transmission lines and cables simulated in PSCAD/EMTDC. The fault-location algorithm was implemented in MATLAB. The importance of calibrating the travelling-wave speed is highlighted as the travelling waves have different velocities at different frequencies. Therefore propagation velocities are calibrated to each of the scale of the wavelet coefficients used. Furthermore, the accuracy of the fault-location of the proposed method was studied under noisy input signals.

3.2 Test networks used for simulation studies

Simulations were done using two HVDC transmission networks, one with an OH transmission line and the other with a UG cable. Travelling wave propagation velocities are different in OH lines and UG cables. OH lines are built with bare conductors (typically aluminum) mounted on towers which can be made from wood, steel, or concrete. Electricity can be also be transmitted through cables running underground or undersea (submarine). UG cables typically have the conductor covered with insulating materials (e.g. oil, paper, XLPE), armour and a sheath cover. Travelling-wave travels at a higher speed in OH lines (close to the speed of light) than in UG cables (approximately half of the speed of light). The propagation velocity is a function of line parameters. In a loss less line, it is equal to $1/\sqrt{L \cdot C}$ where L is the line inductance per unit length and C is the line capacitance per unit length [13]. Because of the construction of UG cables, they typically have higher per unit capacitances compared to OH lines. Therefore they have lower propagation velocity. Attenuation is another issue that is important in travelling-wave based fault-location. Attenuation coefficient of a transmission line is proportional to the square root of line impedance and admittance per unit length [13]. Attenuation of travelling waves is faster in UG cables compared to OH line due to dielectric losses in the cable insulation. These dielectric losses substantially increase with the frequency. Therefore it is important to analyse the proposed fault location method in those two types of dc lines.

Both test networks are modified versions of the first Cigré benchmark HVDC scheme [32]. This test network has 500 kV as the nominal dc voltage and it is designed to deliver 1000 MW of active power. Furthermore, a bipolar HVDC configuration is used since most of the present day HVDC systems are built in a bipolar configuration, instead of the mono-polar arrangement in the original reference.

The simplified lumped parameter "π" - model that represents a cable HVDC line scheme in the original Cigré model [32] was replaced with a frequency-dependent distributed-parameter model of a 2400 km long overhead transmission line in the OH line based test network. In the other test network based on UG cable, the simplified π - model was replaced with a frequency dependent distributed parameter model of a 300 km long underground cable. The schematic diagram of the test networks is shown in Fig. 3-1.

The tower structure for the OH dc line and cable parameters for the UG dc line are shown in Fig. 3-2. All the distance measurements are shown in metres. The original test network does not contain a surge capacitor. A surge capacitor is used to protect the converter station equipment from surges travelling along the dc line. The steep wave-front of a surge travelling along the dc transmission line is first attenuated by the line surge impedance and then by the surge capacitor. The existing fault locator installed at the Nelson River HVDC scheme uses surge capacitor current to detect surge-arrival [20]. In the simulation model a *20* nF surge capacitor (minimum in modern HVDC systems) is added to the test networks.

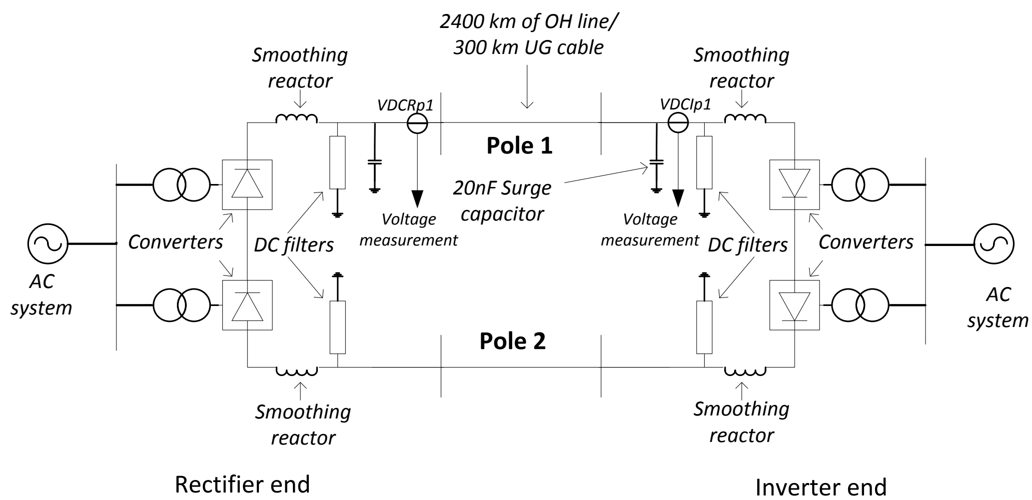

Fig. 3-1 - HVDC test networks modeled in PSCAD/EMTDC

A series smoothing reactor is important in a line commutated type HVDC system [33]. However, the original test network does not contain a separate smoothing reactor because it is included in the simplified cable model. The typical value of the smoothing reactor is in the range of 0.5-1 H [33]. Therefore, a 0.5 H smoothing reactor is placed in series with the transmission line at both ends.

The terminal voltage and surge capacitor current measurements were recorded for a number of simulation cases with different fault locations. The input signals were conditioned assuming a 2 MHz sampling rate, 16-bit Analog to Digital (A/D) conversion resolution, and a 0-20 V range before use in the HVDC line fault-location algorithm. This allows understanding the fault-location performance under the presence of signal conditioning required for digital processing. These A/D parameters were selected after careful testing and considering the capabilities of the commercially available A/D converters.

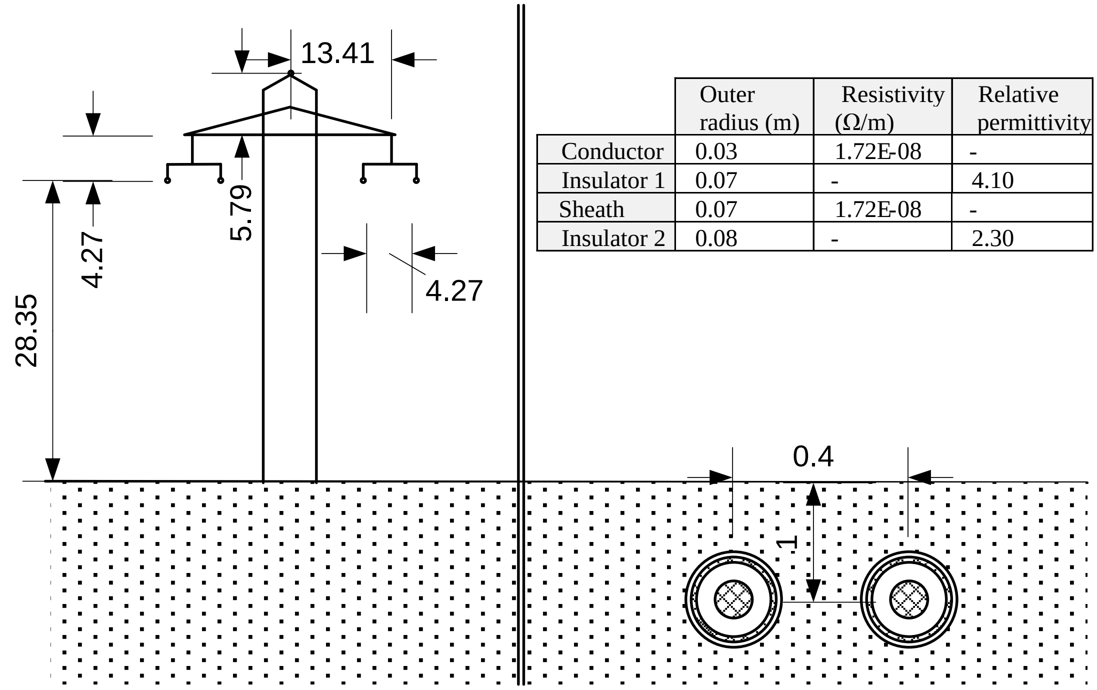

	Outer radius (m)	Resistivity (Ω/m)	Relative permittivity
Conductor	0.03	1.72E-08	-
Insulator 1	0.07	-	4.10
Sheath	0.07	1.72E-08	-
Insulator 2	0.08	-	2.30

Fig. 3-2 - HVDC dc line parameters (Left: OH line tower structure and Right: UG cable parameters)

3.2.1 HVDC test network with 2400 km long OH dc line

Fig. 3-3 shows monitored signals when a permanent dc line fault occurred 100 km away from the rectifier terminal. Fig. 3-3 (a) and (b) show the original terminal voltage and surge capacitor current measurements. The fault initiated surge is first observed at the rectifier end, since the fault is much closer to the rectifier terminal.

The waveforms shown in Fig. 3-3 (c) and (d) are the measured terminal voltages and surge capacitor currents respectively after normalization between 0-20 V and quantization with a 16-bit resolution at a 2 MHz sampling rate. The input vector limits are taken as 0-2 pu for voltage and -1 kA to 1 kA for surge capacitor currents. Therefore values below zero are set to ‘zero’ due to the normalization effect as seen in voltage waveforms in

Fig. 3-3 (c). This does not have any impact in operation of the line fault locator since it only uses the initial sharp change in voltage.

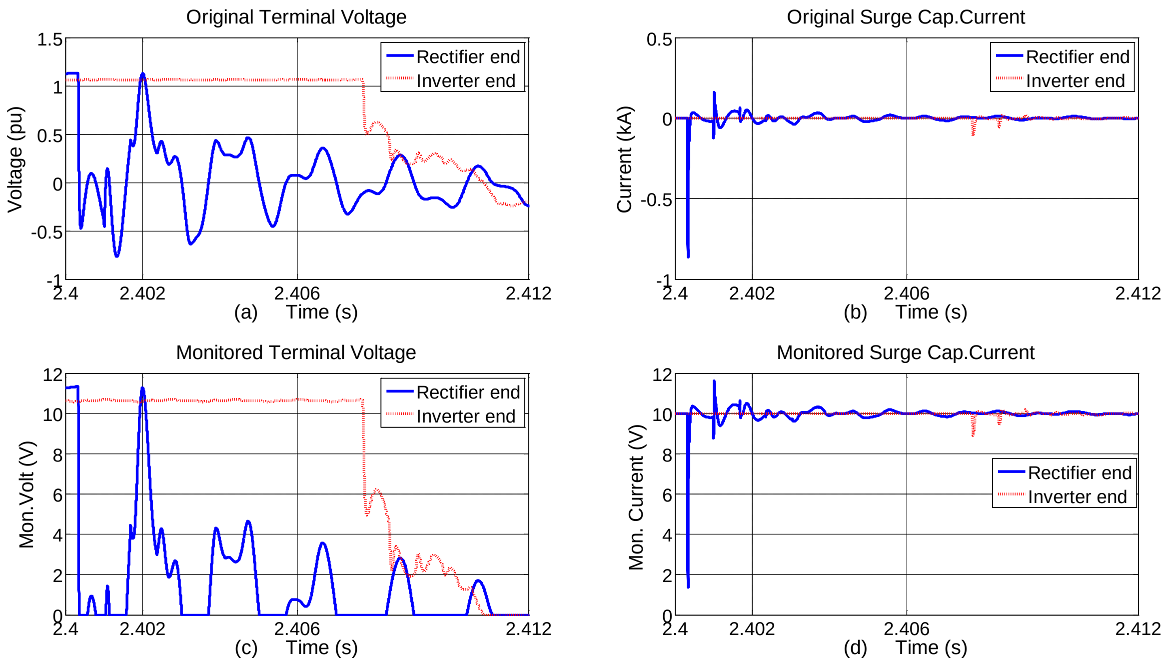

Fig. 3-3 - Comparisons of original terminal voltages and surge capacitor currents with conditioned signals when permanent dc line fault occurred at 100 km from the rectifier end

3.2.2 HVDC test network with 300 km long UG cable dc line

Fig. 3-4 shows monitored signals when a permanent dc line fault occurred at 175 km from the rectifier terminal. Fig. 3-4 (a) and (b) show the original terminal voltage and surge capacitor current measurements. In this case, the fault initiated surge is first observed in the signals measured at the inverter end since the fault is closer to the inverter side.

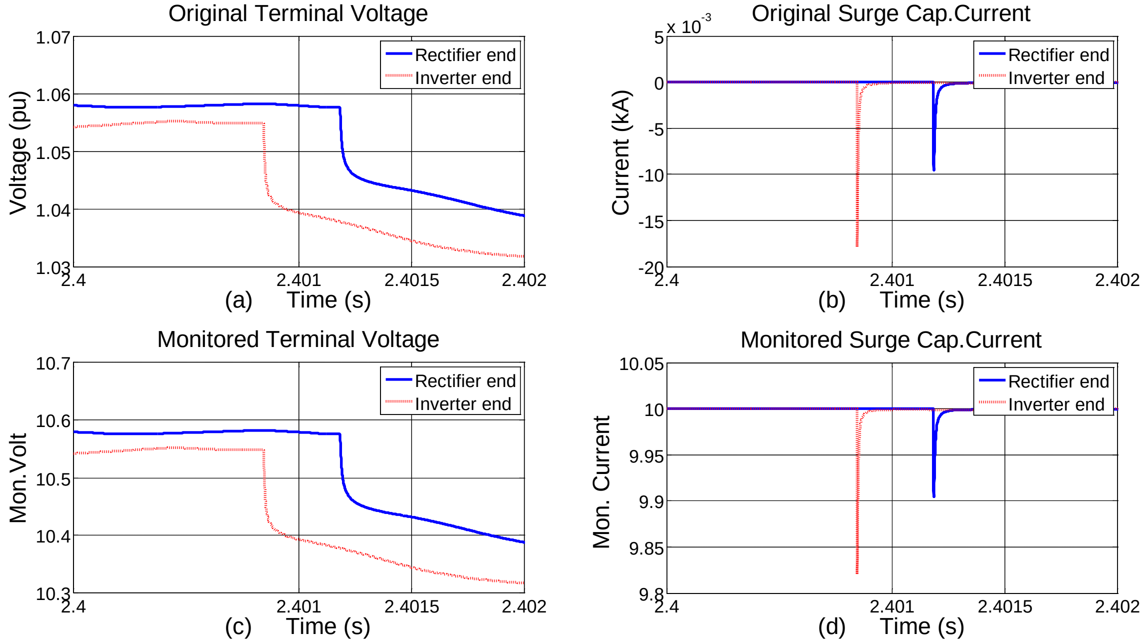

Fig. 3-4 - Comparisons of original terminal voltages and surge capacitor currents with conditioned signals when permanent dc line fault occurred at 175 km from the rectifier end (300 km UG cable HVDC test network)

The waveforms shown in Fig. 3-4 (c) and (d) are the measured terminal voltages and surge capacitor currents respectively after normalization between 0-20 V and quantization with a 16-bit resolution at a 2 MHz sampling rate. Similar to the OH line case, the input vector limits are taken as 0-2 pu for voltage and -1 kA to 1 kA for surge capacitor currents. However in this case there is no value below zero since the lower voltage drop is seen compared to the OH line simulation results.

3.3 Wavelet based surge-arrival time detection

This section analyses the use of wavelet coefficients of the measured signals to detect surge-arrival times.

3.3.1 Proposed fault-location algorithm

A simplified depiction of the two-ended travelling-wave based fault-location algorithm is shown in Fig. 3-5. Initially the potential input signal, either the terminal voltage or the surge capacitor current, is stored to a buffer. Then either DWT or CWT is applied to the input signal and the magnitude values of the wavelet coefficients are extracted.

A threshold to identify the surge-arrival point is set about 50% above the maximum value of the wavelet coefficient of the corresponding input signal under the normal conditions. The safety margin is arbitrarily selected and is required to allow for the noise. Different threshold values are found for each coefficient scale considered in the algorithm. This process is explained in detail later in this chapter.

The time when the magnitude of the considered coefficient rises above the threshold is recognized as the time of arrival of a surge at the terminal. From the measurements at the other end of the transmission line, the time of arrival of the surge in that terminal is received via a telecommunication channel.

As different coefficient scales or levels represent different frequency bands in the signal, the velocity of propagation at each of these frequency bands could differ slightly. These velocities can be found and the algorithm can be calibrated by using test data for a known fault. The calibration process will also be explained in detail later in this chapter.

The algorithm attempts to find an arrival of a surge in the current data buffer, and if it does not find an edge, then the buffer window is shifted and the procedure is repeated. Note that if the signal processing can be done in real time, the occurrence of a fault can be detected by continuously observing the wavelet coefficients, without depending on an external initiation signal. With fast digital signal processors (DSPs), this is also a practically viable approach.

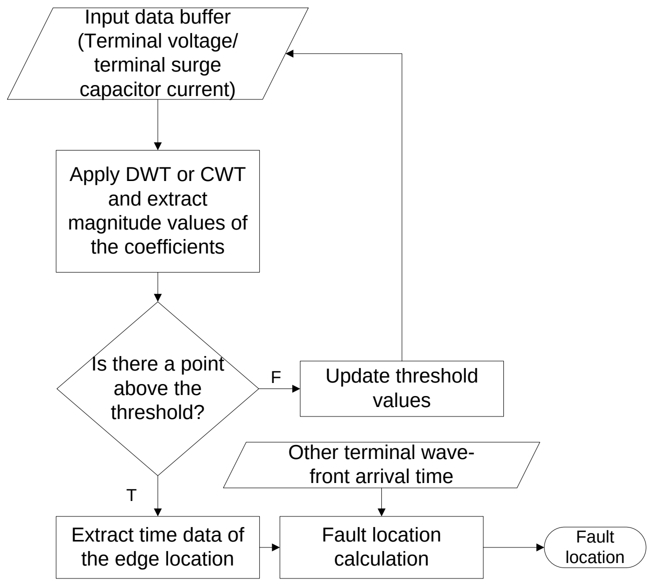

Fig. 3-5 - Simplified WT based LFL algorithm

3.3.2 Discrete Wavelet Transform (DWT) and Continuous Wavelet Transform (CWT)

As explained in Section 2.3.1 in the DWT, the signal is broken into dyadic blocks or the shifting and the scaling is based on a power of 2. The CWT still uses discretely sampled data, however the scaling can be defined from the minimum (original signal scale) to a maximum chosen value, and the shifting process can be made a smooth operation (shifting by one sampling step each time) across the length of the sampled data.

$$CWT(f(k);a,b)^n = \sum_{k=0}^{n} \mathrm{f(k)}\, \psi^*_{\mathrm{a,b}}(\mathrm{k}) \qquad \text{Eq. 3-1}$$

$$\psi^*{}_{a,b}(k) = \frac{1}{\sqrt{a}}\psi\left(\frac{k-b}{a}\right) \qquad \text{Eq. 3-2}$$

In Eq. 3-2 a and b are integers. The effect of discretizing the wavelet is that the time-scale space is now sampled at discrete intervals. The sample number is represented by k in both Eq. 3-1 and Eq. 3-2. In Eq. 3-1 the CWT coefficient is found for a sample window of interest which is denoted by n.

CWT provides a finer time and frequency resolution, and expects to perform better in fault-location applications. The trade-off for this improved resolution is increased computational time and memory required to calculate the wavelet coefficients. However, HVDC line fault-location is not a real time process and therefore, computational time is not a critical issue. A description of the calculation of wavelet transform coefficients is given in Appendix-A.

3.3.3 Application to a sample waveform

Examples of the terminal voltage and the surge capacitor current waveforms observed during an HVDC line fault are shown in Fig. 3-6. All waveforms are sampled at a rate of 2 MHz and the OH transmission line is 2400 km long. Plot in Fig. 3-6 (a) shows the terminal waveforms when a permanent line-to-ground fault occurred 625 km away from the rectifier end. In this case, sharp drops in the voltages and the spikes in the surge capacitors are clearly visible on both sides. Plot in Fig. 3-6 (b) shows the case when the fault occurred 100 km from the rectifier terminal. First, the rectifier end sees a sharp drop in the voltage when the initial surge arrived. The subsequent ripples seen on the rectifier voltage are due to the reflected travelling waves. The magnitudes of the initial sharp voltage drop and the reflected surges are small on the inverter-side voltage for this case.

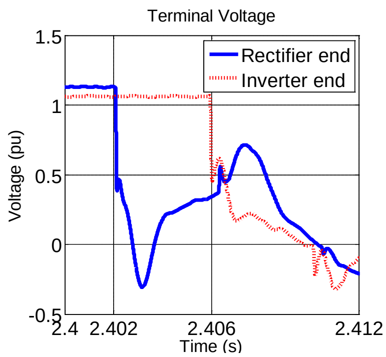

(a)

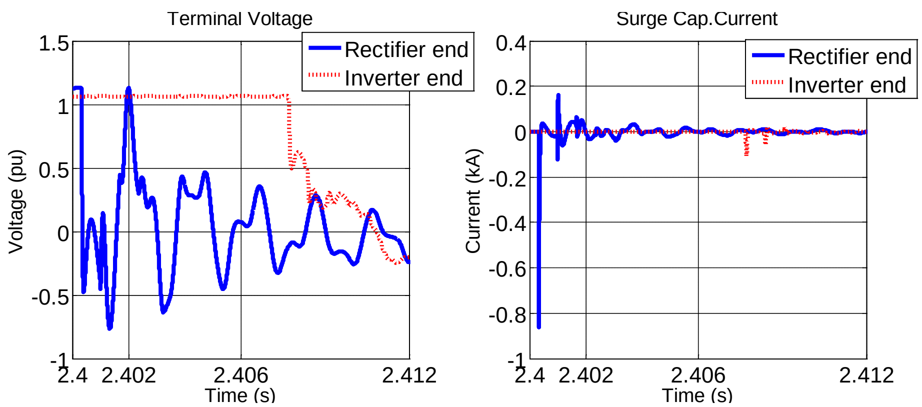

(b)

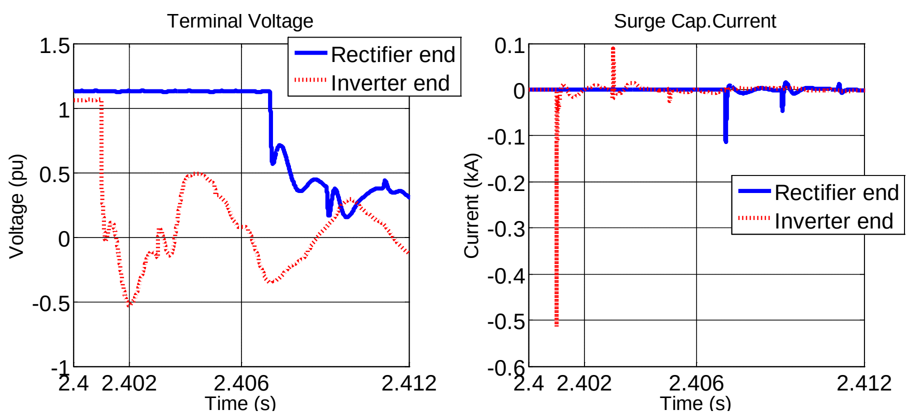

(c)

Fig. 3-6 - Terminal voltages and surge capacitor currents when permanent dc line fault occurred at (a) 625 km (b) 100 km (c) 2100 km from the rectifier end

Also, the magnitude of the surge observed at the inverter-side surge capacitor current is much smaller compared to the rectifier side. This is due to the attenuation of travelling waves when it travels along the transmission line. Plot in Fig. 3-6 (c) shows the waveforms when the fault is closer to the other end (2100 km from the rectifier terminal). In this case the first sharp drop and the ripples due to reflections in the voltage are clearly visible at the inverter side. The spike in the surge capacitor current at the rectifier side is smaller than that of the inverter side. Thus it becomes more difficult to accurately detect a surge when the fault is far from the measuring point.

Comparison of the DWT and CWT coefficient magnitude values for the waveforms shown in Fig. 3-6 (a) is shown in Fig. 3-7. Here it is interesting to observe the surge detection performance. Therefore, only the rectifier end terminal voltage and surge capacitor measurements are analysed.

Plots in Fig. 3-7 (a) and Fig. 3-7 (f) show the rectifier end terminal voltage and surge capacitor current respectively monitored from the simulations. Although the surge appears as a step change in voltage/surge capacitor current in the time scale used in Fig. 3-6 (a), when the time scale is expanded it appears as a smooth change. This explains the difficulty in locating the precise surge-arrival time. CWT of the terminal voltage is calculated with the *Haar* mother-wavelet at scales 4, 8, 16 and 32 and the magnitudes of these coefficients are shown in Fig. 3-7 (b), (c), (d) and (e) respectively. DWT of the same signal is calculated with the *Haar* mother-wavelet for levels 2, 3, 4 and 5 (which are equivalent to selected CWT scale values in frequency bands). Magnitudes of the detail coefficients of DWT are also shown in Fig. 3-7 (b), (c), (d) and (e) respectively. Similarly using the terminal surge capacitor current, CWT and DWT coefficient values are compared in Fig. 3-7 (g), (h), (i) and (j).

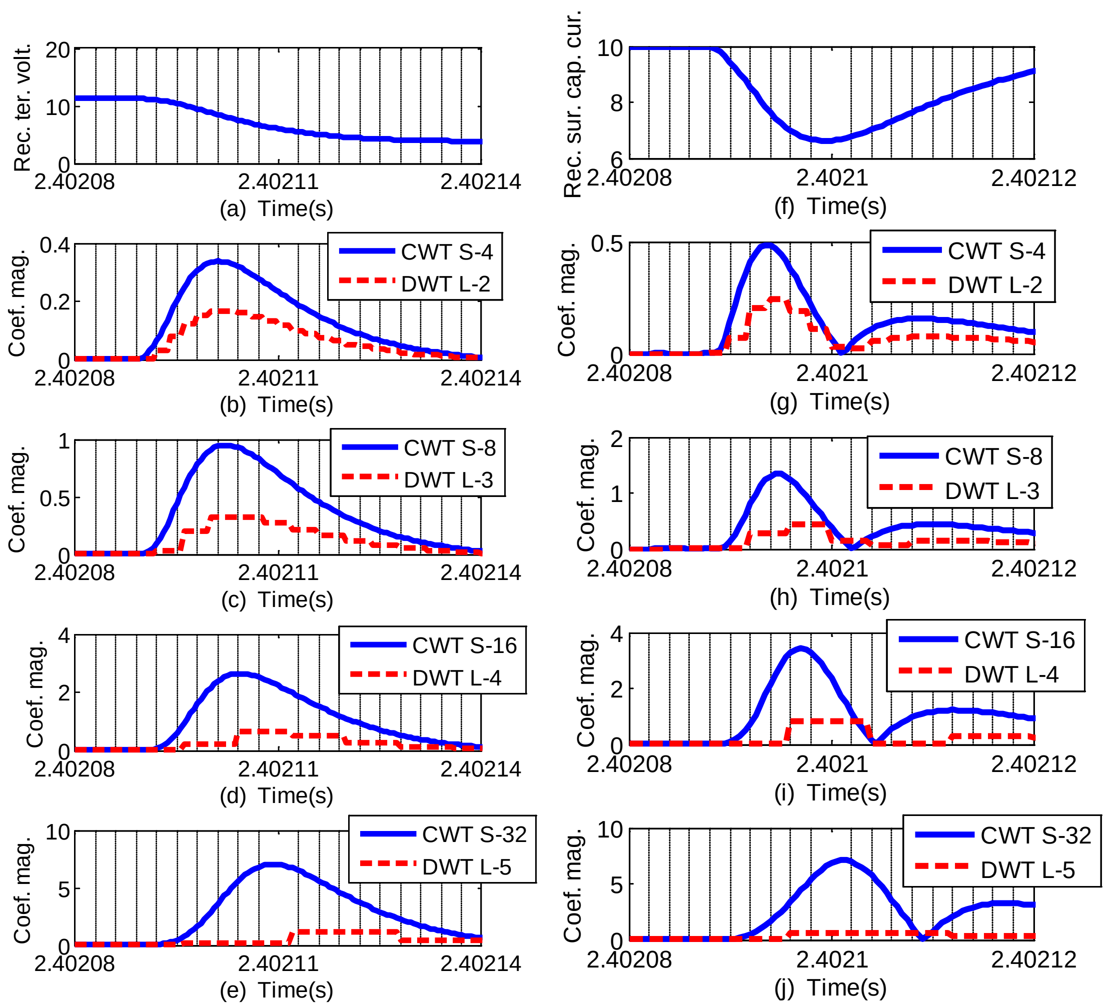

Fig. 3-7 - DWT and CWT coefficient magnitude values of rectifier end voltage and surge capacitor current when a line to ground fault occurred (625 km away from the rectifier end applied at 2.4 s)

As can be seen from Fig. 3-7, the arrival of the surge is observed better in the wavelet coefficients when compared to the original voltage signal. If a proper threshold value is set, then the initial surge-arrival point can be detected by using the wavelet coefficients. This process will be explained with more details in Section 3.3.5. Further, it is clearly visible that the corresponding DWT values are poor in time resolution and also are smaller in magnitude compared with CWT coefficients. Because of this reason, the CWT based fault-location method can be expected to give better accuracy than the DWT based fault-location method. Also, there is a time delay, which increases with the level/scale of the coefficient, associated with the process of calculation of wavelet coefficients. However, this delay should not adversely affect the fault-location if the coefficients of the same level/scale are used at the both ends because only the time differences are used in the equations calculating the fault-location. However, larger errors can be expected at higher levels/scales because the sharpness of the transients seen on the wavelet coefficients becomes lower at higher levels/scales.

Similar comparison is done when the fault happened 2100 km away from the rectifier end and the results are shown in Fig. 3-8. Conditioned terminal voltage and surge-capacitor current signals are shown in Fig. 3-8 (a) and Fig. 3-8 (f). As can be seen in the figure, when the fault is far from the terminal, the changes in the monitored signals are smaller. However, arrival of the surge is observed better in the wavelet coefficients when compared to the original voltage signal.

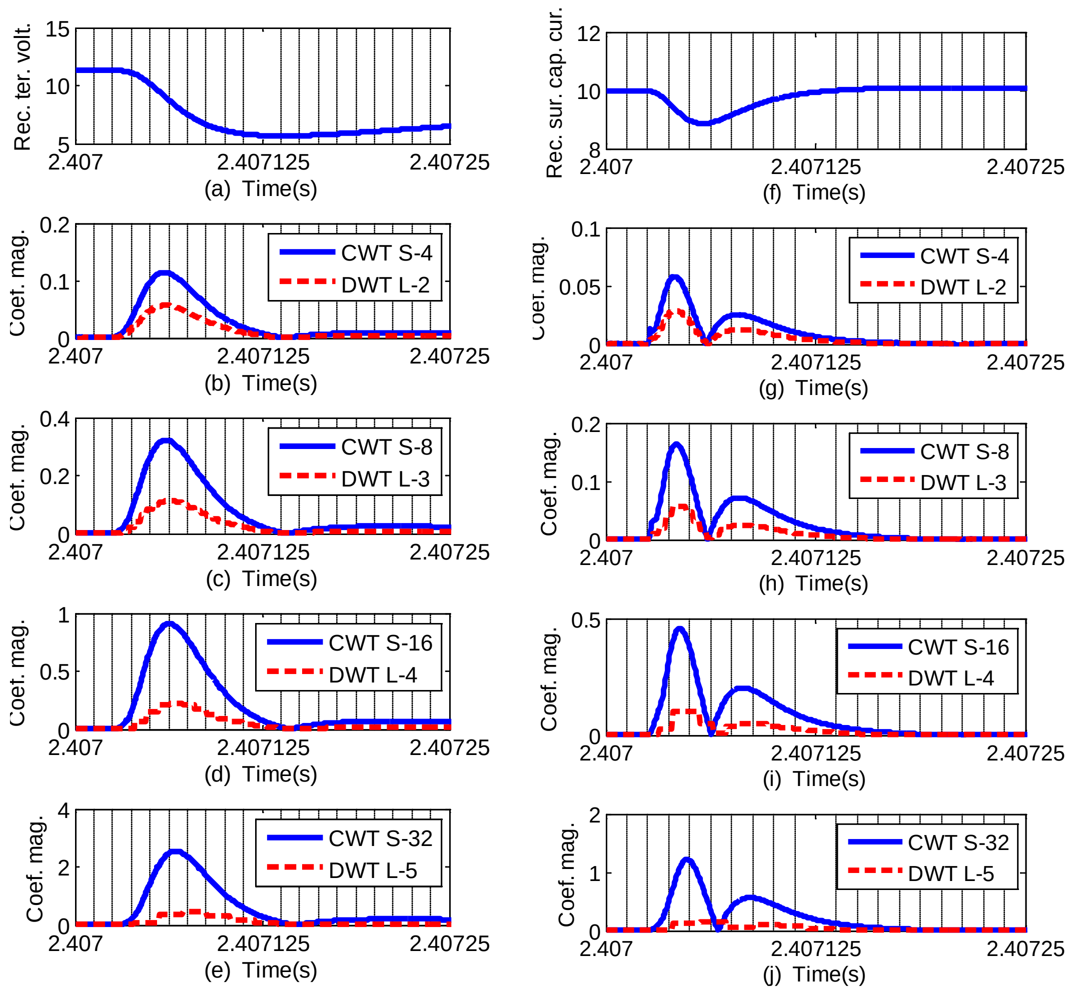

Fig. 3-8- DWT and CWT coefficient magnitude values of rectifier end voltage and surge capacitor current when a line to ground fault occurred (2100 km away from the rectifier end applied at 2.4 s)

Further results are shown in Fig. 3-9 when the fault happened 100 km away from the rectifier end. Conditioned terminal voltage and surge-capacitor current signals are shown in Fig. 3-9 (a) and (f). As can be seen in the figure, when the fault is closer to the terminal, the changes in the monitored signals are sharper. It can be clearly seen that the corresponding DWT values are poor in time resolution and also are smaller in magnitude compared with CWT coefficients.

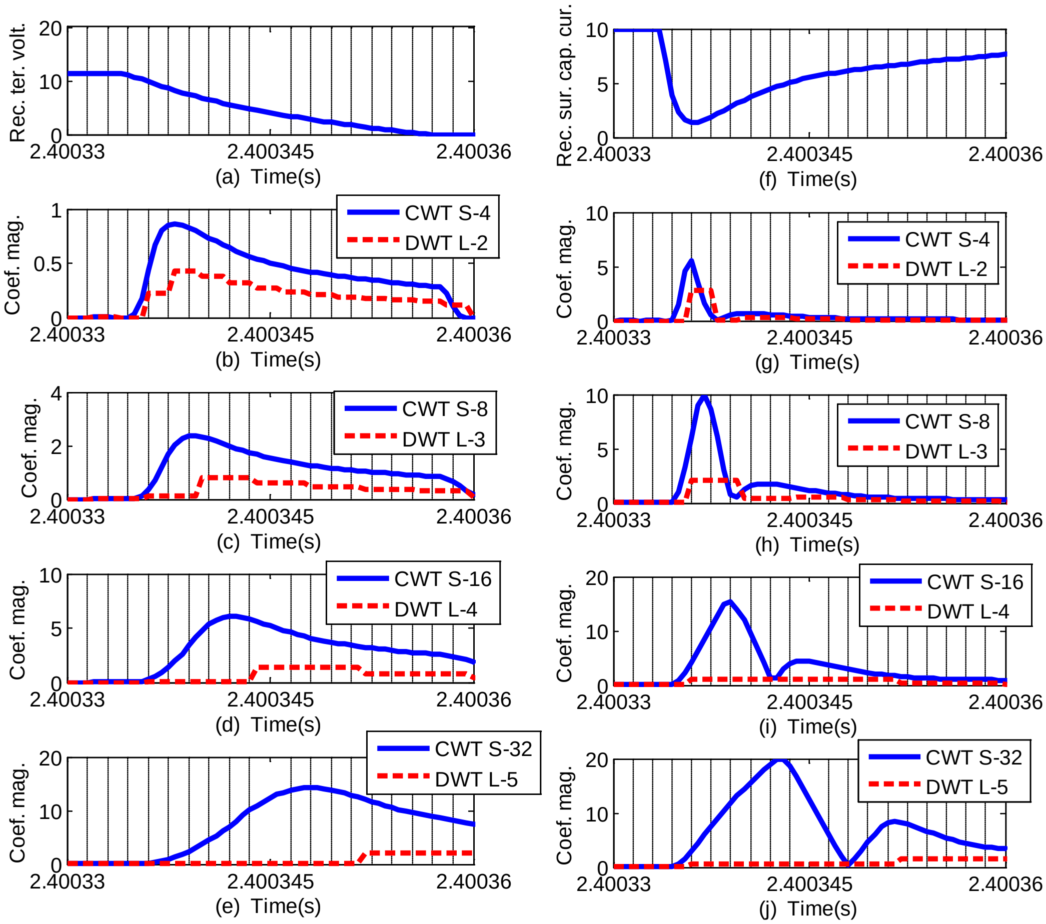

Fig. 3-9 - DWT and CWT coefficient magnitude values of rectifier end voltage and surge capacitor current when a line to ground fault occurred (100 km away from the rectifier end applied at 2.4 s)

3.3.4 Effect of mother-wavelet type

As mentioned before, the accuracy of the travelling-wave based line fault-location is largely dependent on the precise identification of the surge-arrival time. The mother wavelet plays an important role when wavelet transform is used to detect the surge-arrival time. Selection of the proper mother wavelet type is a trial and error study. Monitored rectifier end voltage, when a permanent dc line-to-ground fault applied at 625 km away from the rectifier end, is used to analyze the effect of the mother wavelet. This waveform is shown in Fig. 3-10 (a) and the CWT coefficient magnitude values of that waveform extracted using *Daubechie* family mother-wavelets are shown in Fig. 3-10 (b).

The *Haar* mother-wavelet (*db 1*) provides faster response and the sharpest edge compared with other mother wavelets. Furthermore, it is the simplest mother wavelet and therefore it requires less computational burden in the hardware implementation. Therefore, the *Haar* mother-wavelet is selected in future studies in the wavelet-based line fault locator.

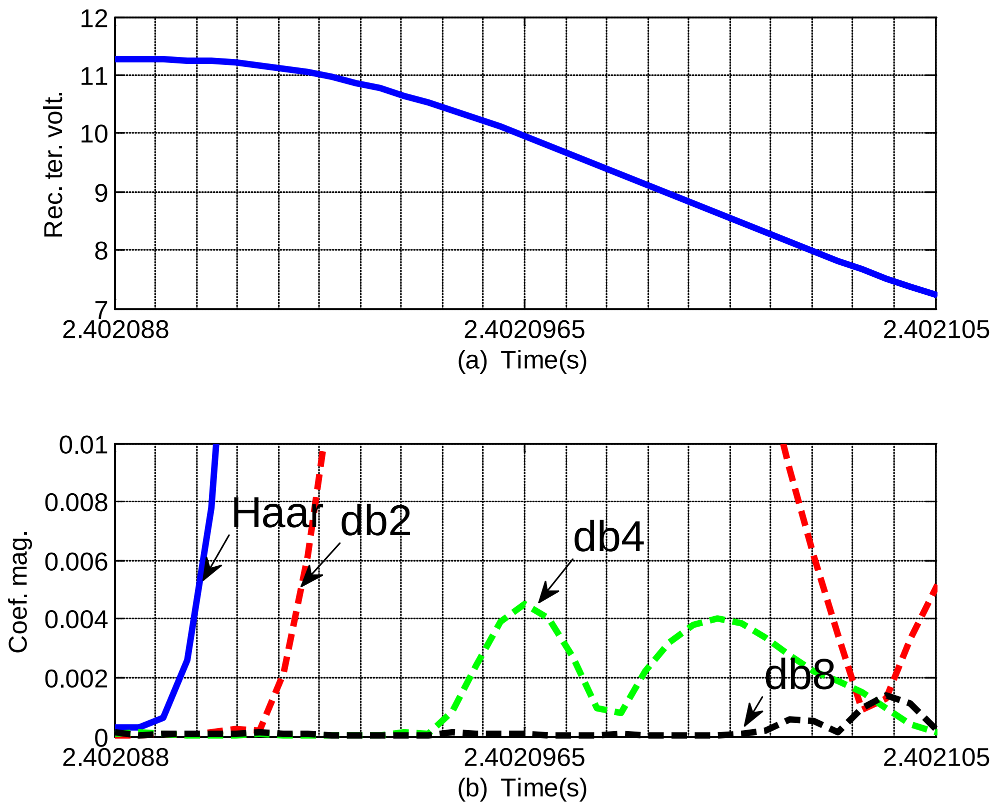

Fig. 3-10 - Comparison coefficient magnitudes of different mother wavelets

(a) Rectifier end terminal voltage (b) Wavelet coefficient magnitudes when a line to ground fault occurred (625 km away from the rectifier end applied at 2.4 s)

3.3.5 Effect of sampling frequency

Travelling-wave based line fault-location requires a high sampling frequency. This is one of the major drawbacks in this method. However, the selection of a suitable sampling frequency is a trade-off between the required accuracy and the availability of signal processing and transducer hardware.

Fig. 3-11can be used to demonstrate the effect of sampling frequency in the accuracy of the fault-location method. Fig. 3-11(a) shows the discretized simulated waveform of the rectifier end voltage. Each sample is available when the waveform is sampled at a 2 MHz frequency. Red dots show the samples available when the waveform is sampled at a 1 MHz frequency. The green and black dots represent the samples when the waveform is sampled at either 500 kHz or 400 kHz frequencies respectively. It is clear when the sampling frequency is reduced the information available in a certain time period is reduced.

Travelling waves propagate along OH lines with a velocity equal to 300000 km/s and along UG cables with a velocity approximately half of that. Therefore the wave travels in the OH line about 300 m and in the UG cable about 150 m within a 1μs time period. If the distance between samples is 1 μs or in other words the sampling frequency is 1 MHz, then there is a possibility of error of about 300 m or 150 m in the OH line or in UG cable respectively. Therefore it is clear how the accuracy of the fault-location is reduced when the sampling frequency is reduced.

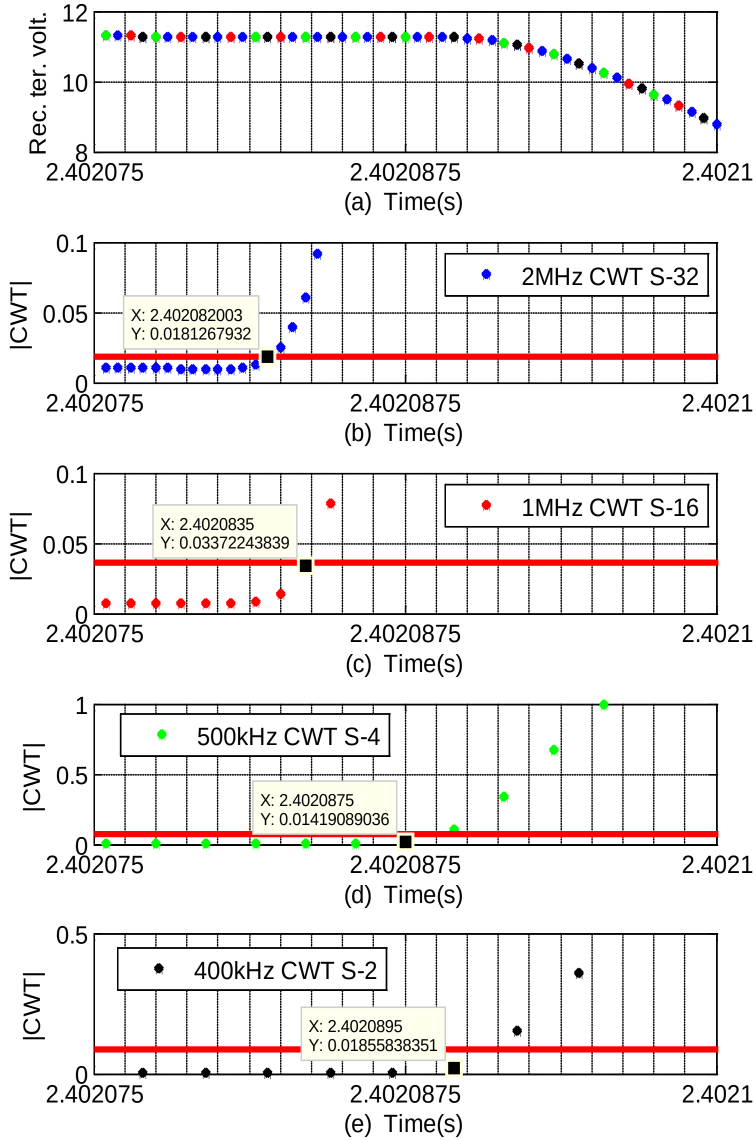

Fig. 3-11 - Effect of sampling frequency

Furthermore, Fig. 3-11(b)-(e) shows the CWT coefficient magnitude values taken with the input signal shown Fig. 3-11 (a) at different sampling frequencies. Similar frequency bands are used in the plots in order to match the CWT scale frequencies at different sampling rate. For example scale 32 at a 2 MHz sampling frequency is representing the 31.25 kHz to 62.5 kHz frequency band and scale 16 at a 1 MHz frequency is representing the same frequency band.

The threshold is selected for each CWT magnitude scale, considering a safety margin of 50% to the steady state maximum value. It is shown by the red line in each plot of the CWT coefficient magnitude. The identified surge-arrival time is marked on each plot. The fastest surge-arrival time is seen at the highest sampling frequency as 2.402082 s.

3.3.6 Determination of propagation velocity

In order to achieve good accuracy from the fault-location algorithm, it is important to use accurate propagation velocity values, which are dependent on the configuration of the OH line or UG cable in the HVDC system. Although it is possible to estimate the propagation velocities from the conductor or cable geometry, the best approach is to estimate these values using the measurements obtained for a known fault-location. Such data is normally obtained during the commissioning of a line-fault location system.

During the test, a permanent dc line fault is applied at a known location. Then the Wavelet coefficient magnitudes are extracted from the monitored terminal measurements. Only the CWT coefficient values are shown for this test result. Surge-arrival times at the two terminals are found using the pre-defined threshold values. Propagation velocity can be calculated for each CWT scale using the Eq. 3-3.

$$V = \frac{L - 2X}{td} \qquad \text{Eq. 3-3}$$

Where L is the total line length, X is the test fault-location and td is the difference between the surge-arrival times at the two terminals found using the CWT coefficients.

As an example, a test fault is simulated at 400 km from the rectifier terminal of the test network with 2400 km of the OH line. Table 3-1 shows the calculated propagation velocities using the wavelet coefficients at different scales. As can be seen, lower scales (corresponding to higher frequency) have higher propagation velocities. Also the calculated value of the propagation velocity slightly depends on the input signal considered.

Table 3-1 - Calibrated propagation constant values for OH line HVDC test network

		CWT Scales			
		4	**8**	**16**	**32**
P.constant (km/s)	**Using Terminal Voltage**	298790.00	298760.00	298700.00	298620.00
	Using Surge Cap. Current	298810.00	298790.00	298760.00	298730.00

As another example, a test fault is applied at 100 km away from the rectifier terminal of the test network with 300 km of UG cable. Table 3-2 shows the calculated propagation velocities. As can be seen, propagation velocities in the cable are approximately half of the propagation velocities seen in the OH lines. In this case also, the propagation velocity changes with the scale of the wavelet coefficient considered and the type of the input signal, but not systematically as in the case of the OH line.

Table 3-2 - Calibrated propagation constant values for UG cable HVDC test network

		CWT Scales			
		4	**8**	**16**	**32**
P.constant (km/s)	**Using Terminal Voltage**	147820.00	147710.00	147710.00	147820.00
	Using Surge Cap. Current	147710.00	147710.00	147820.00	147820.00

3.4 Simulation results for HVDC systems with extra-long dc line

The results of the dc line fault-location with wavelet coefficients are presented for the two test networks, the HVDC system with a 2400 km long OH line and the HVDC system with a 300 km long UG cable. The simulation tests were designed to

- compare the fault-location performance with two potential input signals considered, (i) the converter terminal voltages and (ii) the surge capacitor currents.
- compare the fault-location performance with DWT and CWT coefficients of the input signals
- identify the most suitable scales/levels of the wavelet coefficients
- investigate the effect of noise and identify the best parameters under the presence of noise.

The fault-location performance was evaluated using the absolute prediction error. This value shows the magnitude difference between the predicted fault-location and the actual fault-location in kilometers.

3.4.1 Simulation results: HVDC test network - 2400 km OH line

Table 3-3 and Fig. 3-12 show the fault-location results for different fault locations, when the CWT coefficients of the terminal voltage measurements are used to identify the travelling-wave arrival time. The prediction errors are within ±350 m for CWT scales up to 32. In general the lower scales give better accuracy.

Table 3-3 - Fault-location results with different CWT coefficients (scales 4, 8, 16, and 32) of the terminal voltages

Actual fault-location (km)	Predicted fault-location (in km) using CWT Scales			
	4	8	16	32
1	1.120	1.158	1.157	1.120
10	10.159	10.120	10.193	10.228
100	100.093	100.047	100.028	100.037
157	157.012	157.035	157.006	156.999
251	250.980	250.994	251.022	250.915
333	333.072	333.003	333.091	333.035
850	850.121	850.079	850.145	850.093
1111	1110.887	1110.821	1110.837	1110.713
1200	1200.000	1200.075	1200.075	1200.075
1323	1322.951	1323.014	1322.916	1323.031
1400	1400.037	1399.944	1399.907	1400.000
2040	2040.037	2040.034	2040.026	2040.090
2100	2099.869	2099.860	2099.767	2099.664
2240	2239.925	2239.903	2239.933	2239.866

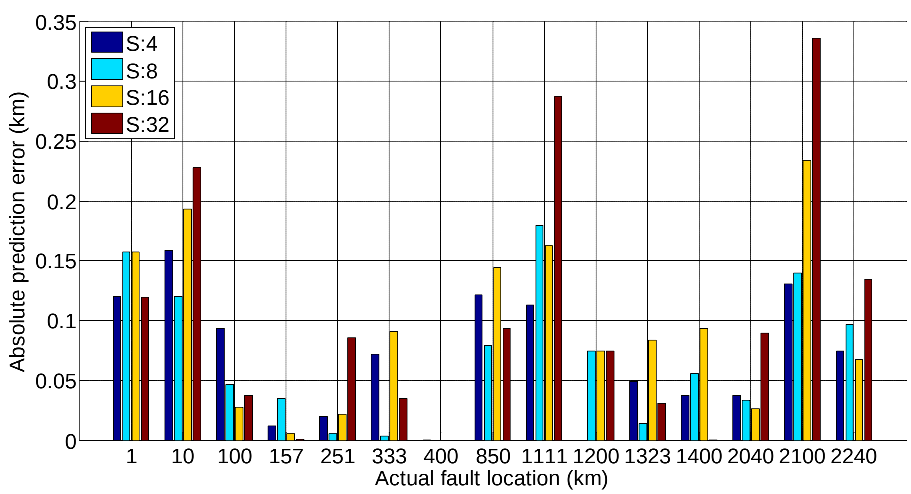

Fig. 3-12 - Fault-location errors with different CWT coefficients (scale 4, 8, 16, and 32) of the terminal voltages

Table 3-4 and Fig. 3-13 show the fault-location results when the surge capacitor currents are used as the input signals. Overall accuracy is similar to the accuracy obtained with the terminal voltages as inputs. The prediction errors are within ±400 m for the

CWT scales up to 32. Again, the lower scales give better accuracy. These results indicate that both input signals, the surge capacitor current and the terminal voltage, work equally well for fault locating in HVDC.

Table 3-4 - Fault-location results with different CWT coefficients (scale 4, 8, 16, and 32) of the surge capacitor currents

Actual fault-location (km)	Predicted fault-location (in km) using CWT Scales			
	4	8	16	32
1	1.158	1.270	1.232	1.195
10	10.197	10.233	10.270	10.232
100	100.140	100.168	100.196	100.149
157	157.064	157.087	157.110	157.058
251	250.966	250.980	250.994	251.008
333	332.991	333.072	333.078	333.010
850	850.014	849.972	849.930	849.888
1111	1110.953	1110.962	1110.895	1110.829
1200	1200.000	1199.925	1199.851	1199.851
1323	1322.962	1322.951	1322.939	1322.853
1400	1399.981	1399.888	1399.869	1399.776
2040	2039.892	2039.888	2039.735	2039.731
2100	2099.879	2099.720	2099.711	2099.627
2240	2239.873	2239.776	2239.754	2239.656

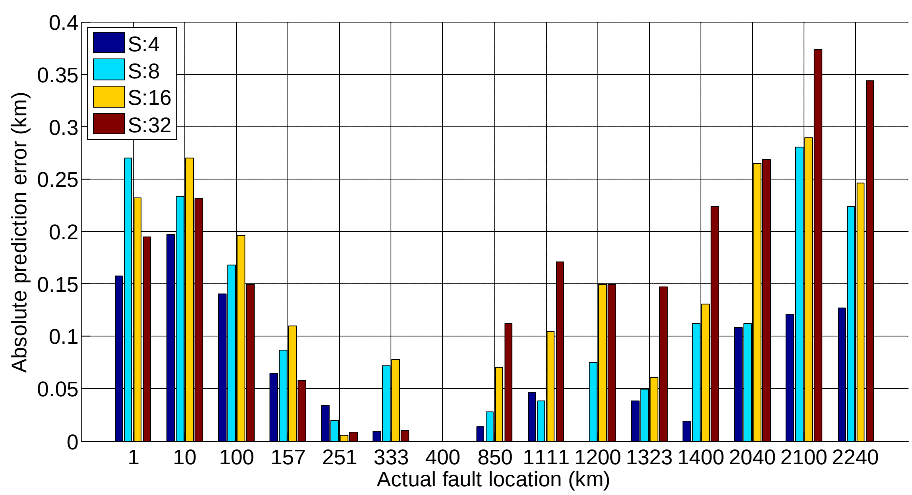

Fig. 3-13 - Fault-location errors with different CWT coefficients (scales 4, 8, 16, and 32) of the surge capacitor currents

Table 3-5, Table 3-6, Fig. 3-14, and Fig. 3-15 summarize the fault-location performance obtained when DWT coefficients of the input signals are used to detect the surge-arrival times. In Fig. 3-14 the terminal voltages are used as the inputs for the fault-location algorithm. According to the tested cases the prediction error is within ±2.5 km when detail coefficients up to level 5 are used. Although smaller prediction errors are visible at lower DWT levels, these coefficients can be affected by noise.

Table 3-5 - Fault-location results with different DWT coefficients (levels 2, 3, 4, and 5) of the terminal voltages

Actual fault-location (km)	Predicted fault-location (in km) using DWT levels			
	2	**3**	**4**	**5**
1	1.046	1.046	1.941	2.236
10	10.011	9.712	10.601	12.374
100	99.963	99.365	100.187	101.826
157	156.743	157.041	157.223	158.777
251	250.878	250.579	251.885	250.913
333	332.761	332.761	334.005	335.296
850	850.056	850.056	850.317	852.031
1111	1110.945	1110.945	1110.414	1110.548
1200	1200.000	1200.000	1200.000	1200.000
1323	1323.123	1323.422	1323.031	1324.338
1400	1400.224	1399.925	1399.179	1398.882
2040	2040.344	2040.344	2040.911	2039.955
2100	2100.112	2100.112	2099.440	2099.590
2240	2240.269	2240.269	2240.090	2238.539

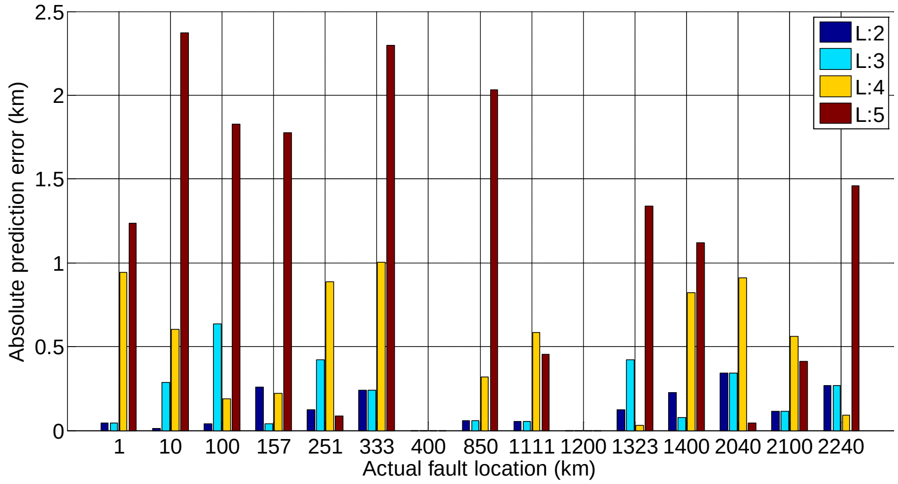

Fig. 3-14 - Fault-location errors with different DWT coefficients (levels 2, 3, 4, and 5) of the terminal voltages

In Table 3-6 and Fig. 3-15, detail DWT coefficients of the surge capacitor currents are used as inputs. The results indicate that the prediction errors less than ±2.2 km are achievable for the tested cases using DWT levels up to 5. Again a better accuracy can be achieved with lower detail levels.

Table 3-6 - Fault-location results with different DWT coefficients (levels 2, 3, 4, and 5) of the surge capacitor currents

Actual fault-location (km)	**Predicted fault-location (in km) using DWT levels**			
	2	**3**	**4**	**5**
1	2.540	2.241	1.608	-1.083
10	11.505	9.712	9.083	9.083
100	99.963	99.963	98.783	98.783
157	157.041	157.041	155.892	156.191
251	250.878	250.579	250.675	250.675
333	333.059	333.358	332.900	332.900
850	850.056	850.056	849.871	848.675
1111	1110.945	1110.945	1111.496	1112.692
1200	1200.000	1199.402	1198.804	1200.000
1323	1322.824	1322.824	1323.487	1322.291
1400	1399.925	1399.925	1400.629	1399.433
2040	2040.045	2040.344	2040.788	2039.891
2100	2099.813	2100.112	2100.588	2099.691
2240	2239.970	2240.269	2241.417	2241.417

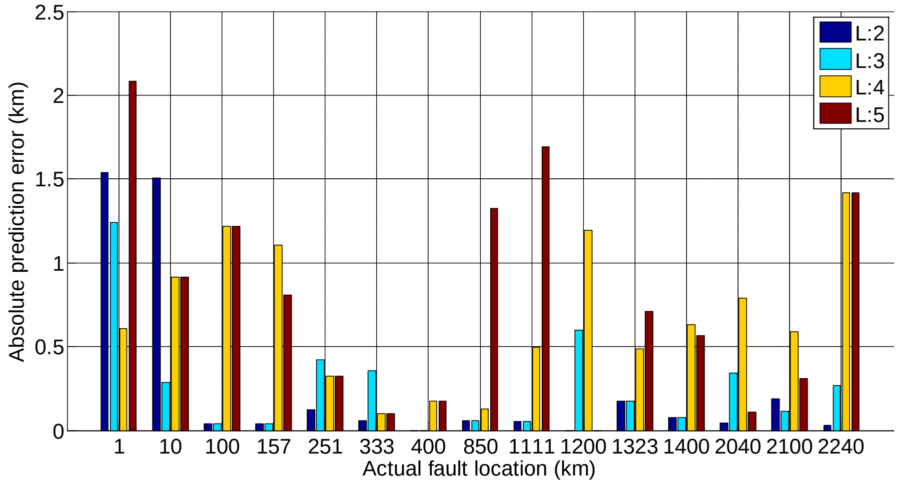

Fig. 3-15 - Fault-location errors with different DWT coefficients (levels 2, 3, 4, and 5) of the surge capacitor currents

When DWT and CWT based fault-location methods are compared for the test network with 2400 km of OH line, it can be clearly seen that the CWT based method provides consistently better fault-location accuracy than the DWT based method.

3.4.2 Simulation results: HVDC test network - 300 km UG cable

Table 3-7, Fig. 3-16, and Table 3-8, Fig. 3-17 show the fault-location results and prediction errors obtained with CWT coefficients. In Fig. 3-16 terminal voltages are used as inputs. The prediction errors are in the range of ±200 m for the test cases using CWT scales up to 32.

Table 3-7 - Fault-location results with different CWT coefficients (scales 4, 8, 16, and 32) of the terminal voltages

Actual fault-location (km)	Predicted fault-location (in km) using CWT scales			
	4	8	16	32
1	0.961	1.034	0.997	0.813
5	4.952	5.022	4.985	4.804
10	9.941	10.007	9.970	9.830
150	150.000	150.000	149.963	150.000
175	174.982	175.000	175.037	175.018
200	200.037	200.000	200.000	200.074
201	201.035	200.997	201.034	201.072
247	247.007	246.972	247.009	247.118
250	250.037	250.000	250.000	250.074
290	290.059	289.993	289.993	290.133
299	299.039	298.966	299.003	299.150

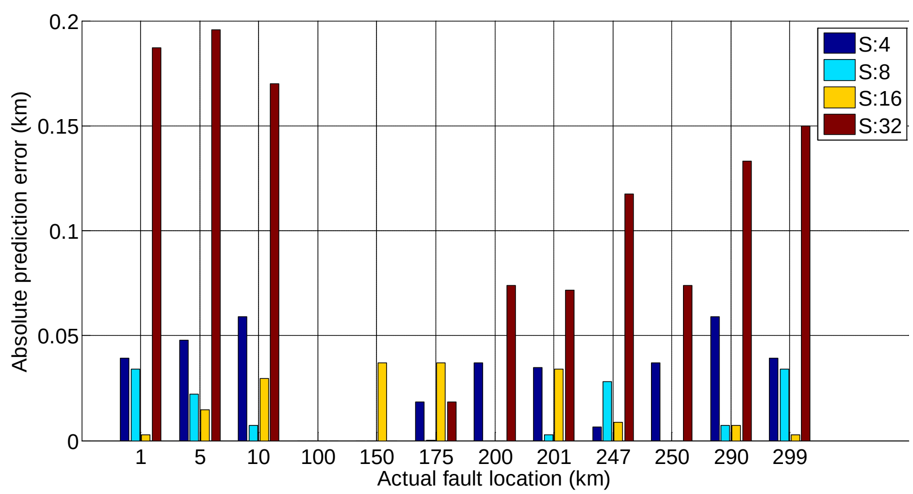

Fig. 3-16 - Fault-location errors with different CWT coefficients (scales 4, 8, 16, and 32) of the terminal voltage

Table 3-8 - Fault-location results with different CWT coefficients (scales 4, 8, 16, and 32) of the surge capacitor currents

Actual fault-location (km)	**Predicted fault-location (in km) using CWT scales**			
	4	**8**	**16**	**32**
1	1.182	1.145	1.035	0.998
5	5.170	5.133	5.026	4.989
10	10.155	10.118	10.015	9.978
150	150.000	150.000	150.000	150.000
175	174.963	174.963	174.982	174.982
200	200.000	199.963	200.000	200.000
201	200.960	200.960	200.998	201.035
247	246.861	246.935	247.007	247.007
250	249.889	249.889	249.963	250.000
290	289.845	289.882	289.985	290.022
299	298.818	298.818	298.965	299.002

Fault-location errors when surge capacitor currents were used as inputs are shown in Fig. 3-17. Maximum prediction error values are within ±200 m for the CWT scale 4. The overall prediction errors lie within the same range obtained with the terminal voltages. Therefore, even for the UG cable based HVDC systems, the surge capacitor current can be used as a potential input to this fault-location algorithm.

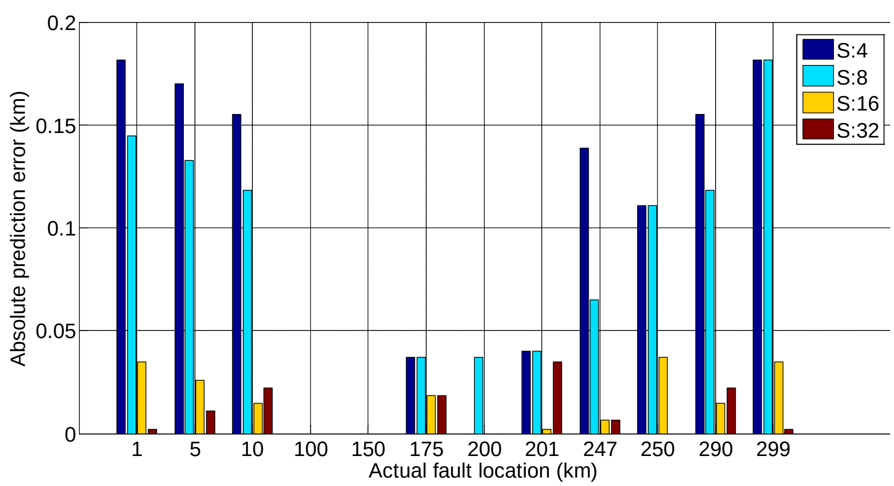

Fig. 3-17 - Fault-location errors with different CWT coefficients (scales 4, 8, 16, and 32) of the surge capacitor currents

Table 3-10 and Fig. 3-19 show the fault-location results obtained using DWT coefficients of the terminal voltages and the surge capacitor currents respectively. The prediction errors are within the range of ±1.8 km in the case of terminal voltages and ±3.5 km in the case of surge capacitor currents. Therefore, again it is clear that the CWT coefficient based method provides better overall accuracy than the DWT coefficient based method. Furthermore, the results also indicate that the same algorithm can be used in HVDC systems with UG cables.

Table 3-9 - Fault-location results with different DWT coefficients (levels 2, 3, 4, and 5) of the terminal voltages

Actual fault-location (km)	**Predicted fault-location (in km) using DWT levels**			
	2	**3**	**4**	**5**
1	0.740	1.471	2.632	2.485
5	4.882	5.588	6.140	6.287
10	9.911	10.588	11.111	11.111
150	150.000	150.000	150.000	150.000
175	175.000	174.853	174.415	174.415
200	200.000	200.000	200.000	199.854
201	201.036	200.588	200.000	200.000
247	247.041	246.471	246.199	246.345
250	250.148	249.559	248.684	248.684
290	290.089	289.412	288.889	288.889
299	299.260	298.529	297.368	297.515

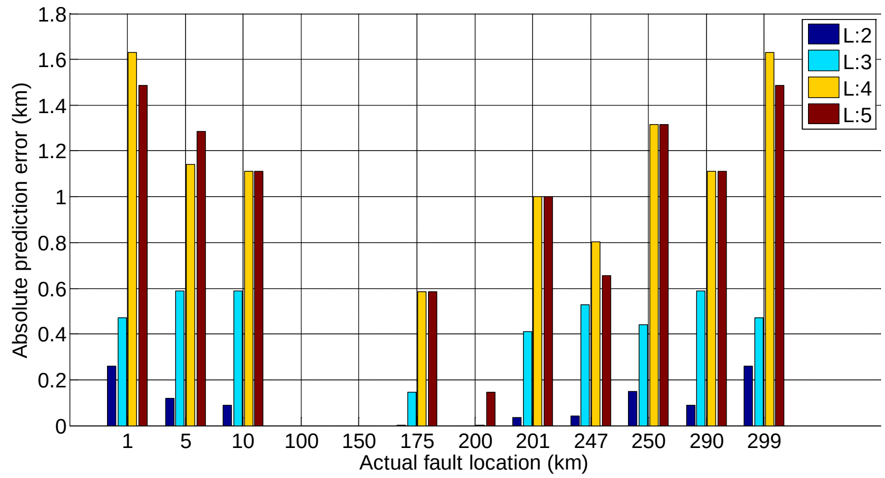

Fig. 3-18 - Fault-location results with different DWT coefficients (levels 2, 3, 4, and 5) of the terminal voltages

Table 3-10 - Fault-location results with different DWT coefficients (levels 2, 3, 4, and 5) of the surge capacitor currents

Actual fault-location (km)	**Predicted fault-location (in km) using DWT levels**			
	2	**3**	**4**	**5**
1	0.888	0.888	0.888	-1.048
5	5.030	4.734	4.438	2.844
10	10.059	9.763	9.467	6.587
150	150.000	150.000	150.000	150.000
175	175.000	175.000	174.704	175.000
200	200.000	200.000	200.000	201.048
201	201.036	201.183	201.183	201.198
247	247.041	247.041	247.337	248.653
250	250.000	250.148	249.852	251.048
290	289.941	290.237	290.533	293.413
299	299.112	299.112	299.112	301.048

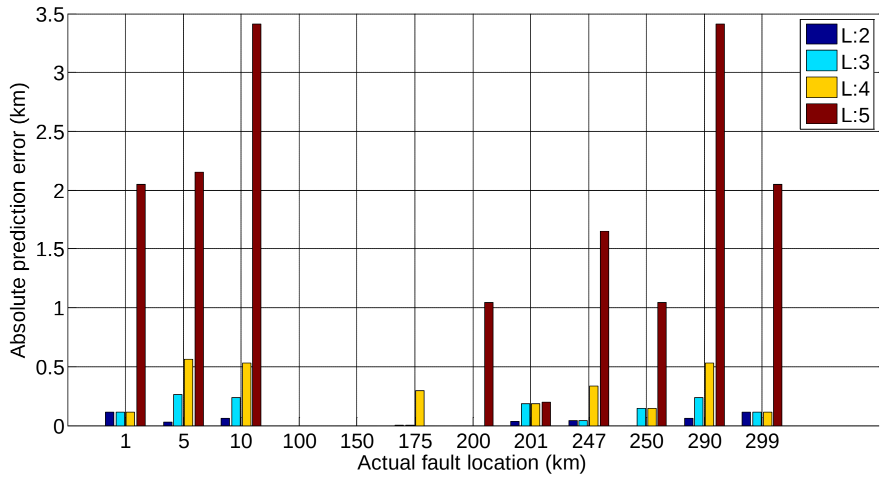

Fig. 3-19 - Fault-location results with different DWT coefficients (levels 2, 3, 4, and 5) of the surge capacitor currents

3.5 Effect of the noise in the input signal

Performance of the fault-location algorithm was tested with input signals contaminated with uniformly distributed random noise. This study was done for both test networks. As an example, Fig. 3-20 shows rectifier terminal voltage and surge capacitor current contaminated with noise in the HVDC system with an OH dc line. In Fig. 3-20 (a), rectifier end voltage with added 0.001 pu white noise is compared with the clean signal. In Fig. 3-20 (b), the same signal with 0.01 pu white noise is shown.

Fig. 3-20 (c) and (d) compare the rectifier end surge capacitor current with 0.001 kA and 0.01 kA noise respectively with the clean signal. In the following sections, results obtained with the CWT based method are presented for the two test networks.

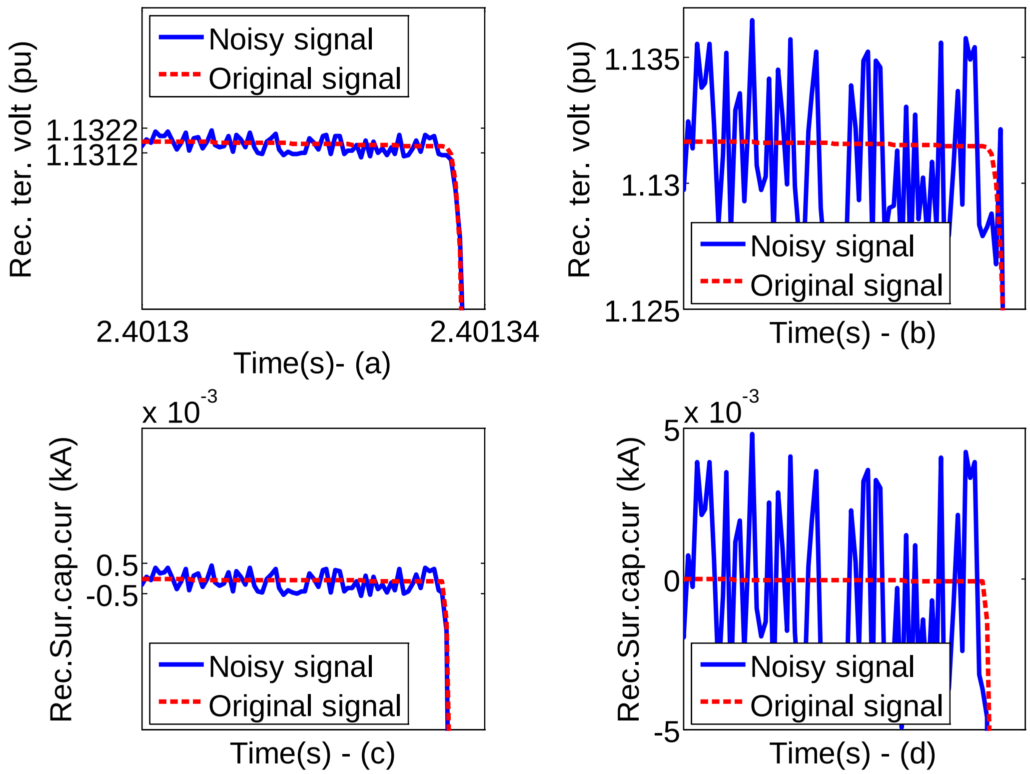

Fig. 3-20 - Surge capacitor current and terminal voltage with added noise

3.5.1 Performance with noisy inputs: HVDC test network with 2400 km long OH dc line

The fault-location performance obtained with terminal voltage measurements contaminated with 0.005 pu noise and 0.001 pu noise is compared with the normal no noise condition in Fig. 3-21. Similarly, Fig. 3-22 compares the prediction fault-location performance obtained with surge capacitor current measurements contaminated with 0.005 kA noise and 0.001 kA noise with the normal no noise condition.

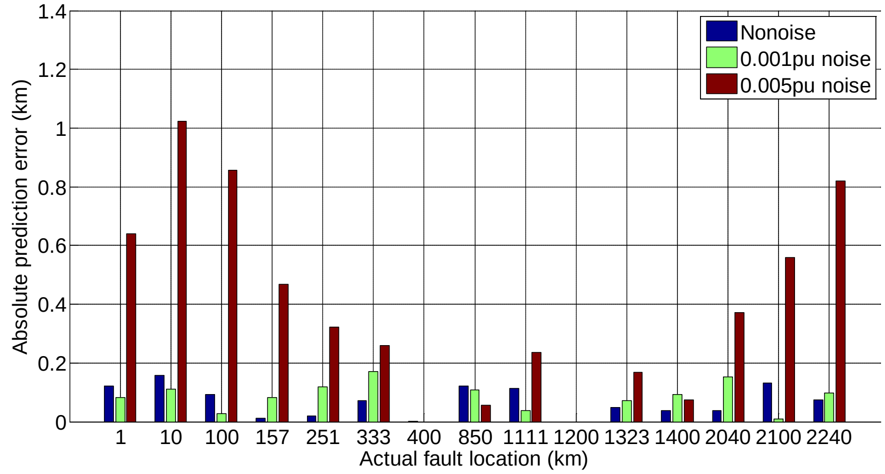

Fig. 3-21 - Prediction errors for different noise levels in the terminal voltages (Using CWT Scale 4)

In both of these cases only the CWT scale 4 coefficients, which gave the lowest errors in general, was used. According to the results, with increasing noise level, the accuracy of the fault-location is reduced, although occasionally the errors are reduced due to compensation of other errors by the random noise.

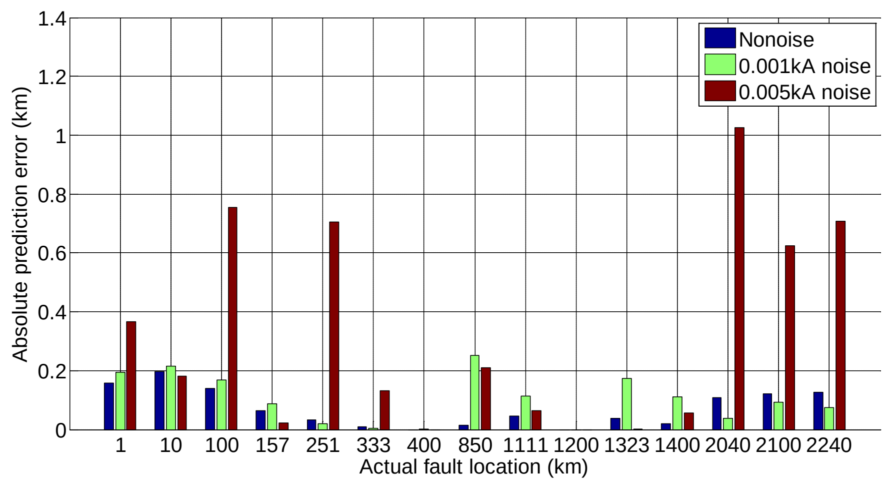

Fig. 3-22 - Prediction errors for different noise levels in the surge capacitor current measurements (Using CWT Scale 4)

Fig. 3-23 compares the prediction errors with different CWT scales when the terminal voltages containing 0.005 pu noise are used as inputs. As can be seen in Fig. 3-23, the lower scales are more sensitive to noise than the higher scales. Therefore when the input signals are corrupted with noise, which is usually the case in practical situations, use of higher CWT scales (Scales 16 and 32) is desirable to achieve robust results.

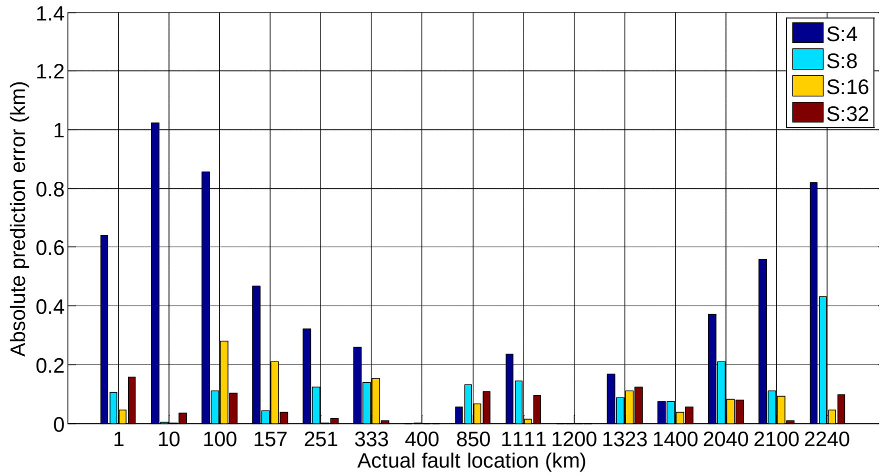

Fig. 3-23 - Comparison of prediction errors using different CWT scales for terminal voltage with 0.005pu of noise

3.5.2 Performance with noisy inputs: HVDC test network with 300 km long UG cable dc line

The results obtained for the UG cable test network are presented in Fig. 3-24 and Fig. 3-25. It was found that cable based test network is more sensitive to noise and therefore higher scales (Scale 16) are used to compare fault location performance with changing noise levels. Fig. 3-24 compares the prediction errors using terminal voltage measurements contaminated with 0.001 pu noise and no noise. Fig. 3-25 compares the prediction errors using surge capacitor measurements contaminated with 0.001 kA noise and no noise.

It is clearly visible that the performance of the fault-location algorithm is sensitive to noise in the input signal. In the case shown in Table 3-11, where the input signal is the voltage contaminated with 0.001 pu noise, it was impossible to find the fault-location with a reasonable accuracy with the scale 4 and 8 wavelet coefficients. Therefore, when the noise is present in the input signals, use of higher CWT scales (Scales 16 and 32) is required in the case of UG cable based systems.

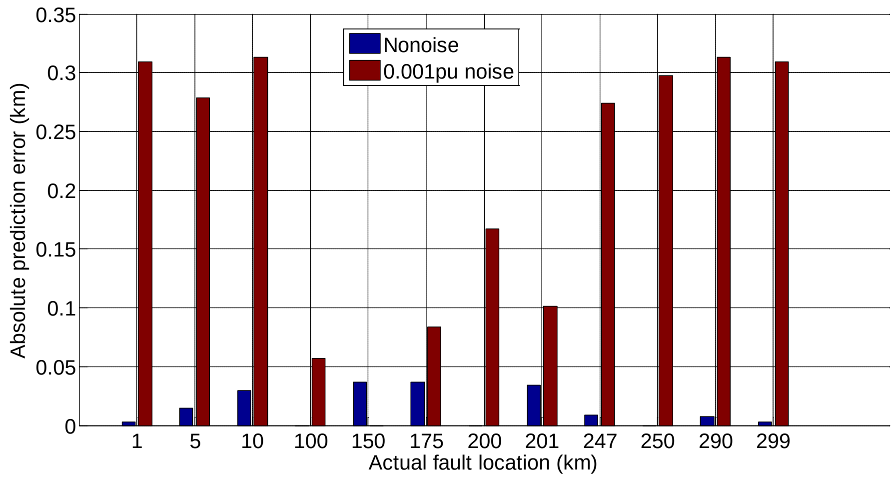

Fig. 3-24 - Prediction errors for different noise levels in the terminal voltages (Using CWT Scale 16)

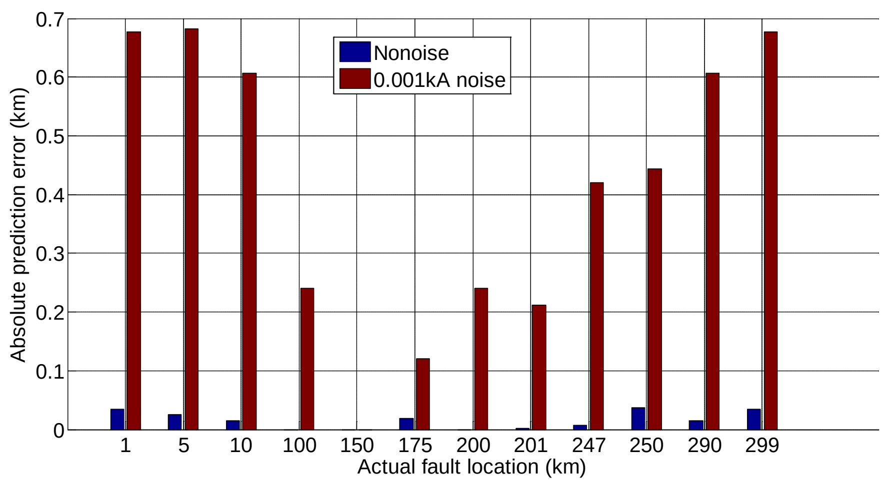

Fig. 3-25 - Prediction errors for different noise levels in the surge capacitor current measurements (Using CWT Scale 16)

Table 3-11 - Comparison of fault-location errors with different CWT scales of the terminal voltages with 0.001 pu noise

Actual fault location (km)	Predicted fault location (km) using CWT scales			
	4	8	16	32
1	NA	0.958	1.141	1.214
5	NA	-0.332	5.081	5.224
10	NA	10.059	10.125	10.228
150	150.000	149.963	150.000	150.000
175	175.110	174.908	174.963	174.945
200	199.890	199.963	199.853	199.890
201	201.066	200.995	200.957	200.993
247	NA	246.905	246.907	246.909
250	NA	249.926	249.890	249.816
290	NA	289.904	289.875	289.772
299	NA	299.042	298.859	298.786

3.6 Concluding remarks

Travelling-wave based fault-location on an extra-long HVDC line using the terminal measurements was investigated. The proposed algorithm that uses the two-terminal travelling-wave fault-location principle has the ability to correctly identify the fault-location in HVDC systems with both OH lines and UG cables. The analysis considered the scaling and quantization effects of the A/D conversion. The simulation results indicated that either the terminal voltage or the surge capacitor current could be used as the input signal. The signal conditioning applied includes scaling to 0-20 V range, 2 MHz sampling, and 16-bit A/D conversion resolution.

Wavelet transform is used to accurately detect the arrival time of travelling waves at the converter terminals. It was shown that the scheme, which uses continuous wavelet transform coefficients yields more robust and accurate wave front detection compared to the scheme that uses discrete wavelet transform coefficients.

Application of the proposed fault-location method to two HVDC systems consisting of a 2400 km long overhead line and a 300 km long underground cable were demonstrated through simulations. The simulation results verified the correct operation of the fault-location algorithm. According to the simulation results, it was possible to achieve a fault-location prediction error of ±400 m for the test system with a 2400 km OH line using either terminal voltage or surge capacitor current measurements as inputs. The simulation results also show this algorithm works with a 300 km UG cable line and both inputs signals would produce similar accuracy levels: in the prediction error range of ±200 m under normal conditions for permanent line to ground faults.

Simulations showed that the proposed method's accuracy degrades with the presence of measurement noise. It was found that the UG cable test network is more sensitive to noise than the OH line test network. However, when the noise is present in the input signals, use of higher CWT scales (Scales 16 and 32) is desirable to achieve robust results in both test networks.

Chapter 4

Fault-location in conventional HVDC schemes with multiple segments

4.1 Introduction

HVDC transmission systems are often used to transport electricity across water bodies such as rivers, lakes, and seas where underground, underwater or submarine cables are used. Since converter stations are not always located close to the shore of the water body, these HVDC systems use a combination of OH transmission and UG cables as the transmission medium. Such intricate configurations are becoming an integral part of HVDC systems [18], [34]. Existing travelling-wave-based dc line fault-location methods have been developed for the HVDC systems with only OH transmission lines or only UG cable. Fault-location in HVDC systems with combination of overhead lines and cables has been generally achieved by considering each line section separately. However, this practice is expensive, as it requires duplicate installation of additional hardware at both ends of each section.

In this chapter, a novel method is proposed for locating faults in an HVDC system with a combination of OH lines and UG cables by using only the terminal measurements. The method uses the travelling-wave principle and predicts the faulted line segments and the exact fault-location on the faulted line segment. Furthermore, the accuracy of detecting the arrival of travelling waves at the terminals is improved with CWT. The relative merits of using the terminal voltage and the terminal surge capacitor current for the detection of travelling waves are examined. Practical considerations such as the influences of noise, A/D conversion precision and the fault impedance on the fault-location accuracy were also investigated.

4.2 Development of the fault-location algorithm for an HVDC transmission system with three line segments

An HVDC system with three line segments is shown in Fig. 4-1. This is a common configuration that occurs when the HVDC system involves an underground or submarine cable section, (the middle cable segment) connected to the converter stations via overhead line segments.

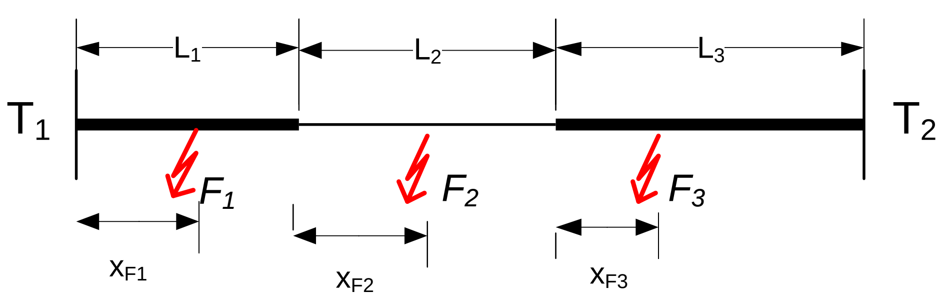

Fig. 4-1 - HVDC system with two segments of OH lines and one segment of cable

The lengths of the segments are L_1, L_2 and L_3 respectively. Faults F_1, F_2 and F_3 located on Segments 1, 2, and 3 respectively are used to explain the fault-location concept. The distance to a fault is calculated from the beginning of the faulted segment. For example, x_{F1} is the distance to fault F_1 in Segment 1 from the terminal T_1, and x_{F2} is the distance to fault F_2 from the beginning of Segment 2.

Consider the case of fault F_1. If the fault occurs at time $t=0$, the time of arrival of the travelling-wave at Terminal T_1 is given by:

$$t_{1-F1} = \frac{x_{F1}}{v_1} \qquad \text{Eq. 4-1}$$

Where v_1 is the propagation velocity of the travelling-wave in segment 1. The arrival time of the travelling-wave to terminal T_2 for the same fault is given by:

$$t_{2-F1} = \left(\frac{L_1 - x_{F1}}{v_1}\right) + \frac{L_2}{v_2} + \frac{L_3}{v_3} \qquad \text{Eq. 4-2}$$

Where v_2 and v_3 are the propagation velocities of the travelling-wave in segments 2 and 3 respectively. The difference between the arrival times Δt_{12-F1} can then be obtained as:

$$\Delta t_{12-F1} = t_{1-F1} - t_{2-F1} = \frac{2 \cdot x_{F1}}{v_1} - \frac{L_1}{v_1} - \frac{L_2}{v_2} - \frac{L_3}{v_3} \qquad \text{Eq. 4-3}$$

The distance to the fault from the beginning of segment 1 can be obtained from Eq. 4-3 as

$$x_{F1} = \left(\Delta t_{12-F1} + \frac{L_1}{v_1} + \frac{L_2}{v_2} + \frac{L_3}{v_3}\right) \times \frac{v_1}{2} \qquad \text{Eq. 4-4}$$

If Δt_{12-F1} is obtained from the measurements, the fault can be located given the propagation velocities in the three segments.

Now consider fault F_2 that occurs in the middle segment at instant $t=0$. The respective surge-arrival times at terminals T_1 and T_2 are given by Eq. 4-5 and Eq. 4-6.

$$t_{1-F2} = \frac{x_{F2}}{v_2} + \frac{L_1}{v_1} \quad \text{Eq. 4-5}$$

$$t_{2-F2} = \left(\frac{L_2 - x_{F2}}{v_2}\right) + \frac{L_3}{v_3} \quad \text{Eq. 4-6}$$

The difference between surge-arrival times $\Delta t_{12\text{-}F2}$ is

$$\Delta t_{12-F2} = \frac{2 \cdot x_{F2}}{v_2} + \frac{L_1}{v_1} - \frac{L_2}{v_2} - \frac{L_3}{v_3} \quad \text{Eq. 4-7}$$

This gives the fault-location with respect to the start of segment 2 as

$$x_{F2} = \left(\Delta t_{12-F2} - \frac{L_1}{v_1} + \frac{L_2}{v_2} + \frac{L_3}{v_3}\right) \times \frac{v_2}{2} \quad \text{Eq. 4-8}$$

Similarly, considering fault F_3 on segment 3, it is possible to show that the distance to fault F_3 from the beginning of segment 3 is given by

$$x_{F3} = \left(\Delta t_{12-F3} - \frac{L_1}{v_1} - \frac{L_2}{v_2} + \frac{L_3}{v_3}\right) \times \frac{v_3}{2} \quad \text{Eq. 4-9}$$

Where $\Delta t_{12\text{-}F3}$ is difference between the surge-arrival times at terminals T_1 and T_2 for fault F_3.

4.3 Identification of the faulty line segment

In deriving the expressions for the distance to the fault given in Eq. 4-4, Eq. 4-8 and Eq. 4-9, it was assumed that the segment where the fault is on is known. However, in practical applications, this is not known. The only measurable quantity is the difference between the surge-arrival times, Δt_{12}. Thus, it is necessary to identify the faulted segment before pinpointing the exact location of the fault. Fortunately, this can be easily achieved by following the procedure described below.

First, the value of Δt_{12} is obtained through the measurements. Then Eq. 4-4, Eq. 4-8 and Eq. 4-9 are applied to obtain three different values for the fault distance (corresponding to x_{F1}, x_{F2}, and x_{F3}). Next, the values of x_{F1}, x_{F2}, and x_{F3} are compared with the corresponding segment lengths, L_1, L_2 and L_3. It can be shown that if the calculated x_{Fi} value is between zero and the segment length, L_i, then the fault is in that segment. Furthermore, only one of the three x_{Fi} values will satisfy the above condition for a given fault. Hence, the faulted line segment can be identified without any ambiguity.

For example, consider a case where the fault is in Segment 2 (middle segment). The actual difference between the surge-arrival times (which should be equal to the measured Δt_{12}) for this case can be obtained from Eq. 4-10 as

$$\Delta t_{12} = \frac{2 \cdot x_{F2}}{v_2} + \frac{L_1}{v_1} - \frac{L_2}{v_2} - \frac{L_3}{v_3} \qquad \text{Eq. 4-10}$$

The estimated value of x_{F1}, obtained by substituting the value of Δt_{12} into Eq. 4-4, is

$$x_{F1} = L_1 + x_{F2} \times \frac{v_1}{v_2} \qquad \text{Eq. 4-11}$$

Since the ratio of propagation velocities (v_1/v_2) is always greater than zero, the estimated value of x_{F1} would be larger than L_1 for this case, indicating that the fault is not on Segment 1. Similarly, substitution of Δt_{12} from Eq. 4-10 (measured Δt_{12}) into Eq. 4-11 gives,

$$x_{F3} = (x_{F2} - L_2) \times \frac{v_3}{v_2}$$

Since (v_3/v_2) is always greater than zero, and x_{F2} is smaller than L_2, the estimated value of x_{F3} for this case would be negative indicating that the fault is not on Segment 3. It is possible to prove that for any given fault, only one of the x_{Fi} values will be in the valid range. Thus, identification of the faulted segment can be achieved. Once the faulted line segment is identified, the fault-location from a terminal can be calculated. Furthermore, the proposed method can be generalized to a transmission system with any number of heterogeneous segments.

4.4 Calibration of the system

In order to achieve good accuracy from the proposed algorithm, it is important to use accurate propagation velocity values. These values are dependent on the configuration of the OH line or UG cable in each of the segments. Although it is possible to estimate the propagation velocities from the conductor (cable) geometry, the best approach is to estimate these values using the measurements obtained for known fault locations. Such data is normally obtained during the commissioning of the line fault-location system.

A systematic method for calibrating propagation velocities of a three-segment HVDC line is proposed in this section. This approach requires conducting three test faults, one on each line segment at known locations. In order to simplify the equations, substitute variables λ_1, λ_2, and λ_3 represent the inverse of the propagation velocities.

$$\lambda_1 = \frac{1}{v_1}, \quad \lambda_2 = \frac{1}{v_2} \quad \text{and} \quad \lambda_3 = \frac{1}{v_3} \tag{Eq. 4-12}$$

The measured surge-arrival time differences corresponding to the faults on Segments 1, 2 and 3 respectively are given by

$$\Delta t_{12-F1} = \lambda_1(2x_{F1} - L_1) + \lambda_2(-L_2) + \lambda_3(-L_3) \tag{Eq. 4-13}$$

$$\Delta t_{12-F2} = \lambda_1(L_1) + \lambda_2(2x_{F2} - L_2) + \lambda_3(-L_3) \tag{Eq. 4-14}$$

$$\Delta t_{12-F3} = \lambda_1(L_1) + \lambda_2(L_2) + \lambda_3(2x_{F3} - L_3) \tag{Eq. 4-15}$$

This set of equations can be conveniently expressed in matrix form,

$$\begin{bmatrix} (2x_{F1} - L_1) & (-L_2) & (-L_3) \\ (L_1) & (2x_{F2} - L_2) & (-L_3) \\ (L_1) & (L_2) & (2x_{F3} - L_3) \end{bmatrix} \begin{bmatrix} \lambda_1 \\ \lambda_2 \\ \lambda_3 \end{bmatrix} = \begin{bmatrix} \Delta t_{12-F1} \\ \Delta t_{12-F2} \\ \Delta t_{12-F3} \end{bmatrix} \qquad \text{Eq. 4-16}$$

Solution of Eq. 4-16 with test data (known x_{Fi} and Δt_{12} values) yields λ_i values, the inversion of which gives the propagation velocities. However, it should be noted that it is not practical to create a fault in the middle of a cable segment. Propagation velocity of the cable section can be estimated from placing the fault at the far end terminal of the cable segment and therefore x_{F2} is equal to L_2.

4.5 Identification of the fault arrival time

As discussed in the second chapter, the fault transient arrival times required for the two-end synchronized measurement based fault-location method can be obtained by analyzing the CWT coefficients of the measured terminal voltage or surge capacitor current signals. Magnitudes of the detail CWT coefficients of the input signal were calculated at different scales: *a = 16, 32, 64* and *128* at each terminal. The surge-arrival point is clearly visible in the CWT coefficients of both types of input signals (terminal voltage and surge capacitor current); a sharp change occurs in all CWT coefficients at the time of the arrival of the wave front.

A threshold to identify the wave front arrival point is set about 50% above the maximum value of the corresponding signal (CWT coefficient) under the normal conditions. The safety margins are required to allow for the noise. Different threshold values are found for different scales of the CWT coefficient considered in the algorithm. The time when the magnitude of the considered CWT coefficient rises above the threshold is recognized as the time of arrival of a wave front at the terminal. From the measurements at the other end of the transmission line, the time of arrival of the surge in that terminal is determined and sent to the fault locator through a suitable telecommunication channel.

4.6 Simulated case study

A conventional two-terminal HVDC system with two OH line segments and one UG cable segment was used in simulation studies. The schematic diagram of the test network is shown in Fig. 4-2. All the simulations were carried out with PSCAD/EMTDC and the fault-location algorithm was implemented in MATLAB.

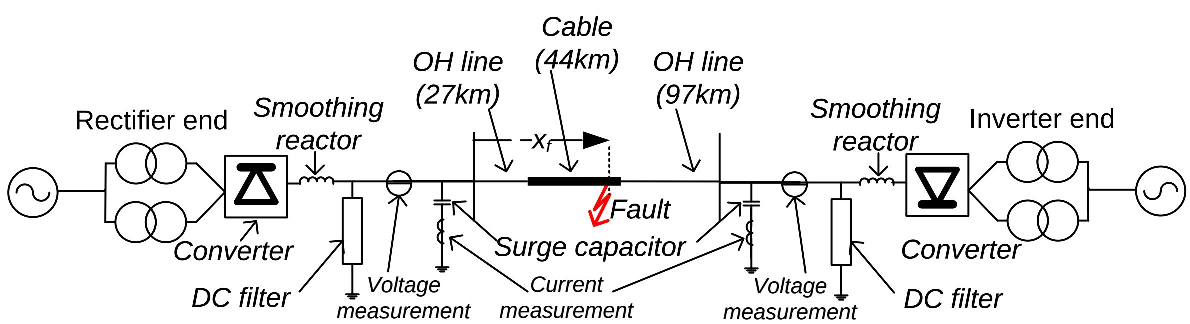

Fig. 4-2 - Three-segment test network

The HVDC transmission line consists of a 27 km OH line segment, a 44 km cable segment and a 97 km OH line segment. Tower structure and cable parameters are similar to the test networks used in Chapter 3. OH lines are represented using distributed parameter transmission line models in PSCAD/EMTDC and Cable is buried 1 m deep and cable segment data is listed in Fig. 3-2. Two identical cables with a horizontal separation of 0.4 m in the same right of way are used to connect the bi-poles. Cables are also represented using a distributed parameter model available in PSCAD/EMTDC.

The input signals were conditioned before applying the fault-location algorithm, assuming a 2 MHz sampling rate, 16-bit A/D conversion resolution, and scaling of the high voltage/current signals to a 0-20 V range before inputting to the A/D converter. This signal conditioning allows testing of the fault-location algorithm under almost realistic conditions.

4.6.1 Monitored signals

Terminal voltages and surge capacitor currents are shown in Fig. 4-3, when the test network was subjected to a short circuit fault at a location 16 km away from the rectifier terminal. Note that these measurements are normalized between 0-20 V and quantized with a 16-bit resolution at a 2 MHz sampling rate (note that 0.1 μs simulation time step corresponds to 10 MHz). The input limits are taken as 0 kV to1000 kV for voltage, and -1 kA to 1 kA for surge capacitor currents. Therefore, the values below zero are set to ‘zero’ due to saturation of the scale as seen in the voltage waveform in Fig. 4-3. This does not have any impact on the wave front detection performance since it only uses the initial change in voltage. The multiple surges in the rectifier end voltage are due to reflections from the fault point. In addition, it can be clearly noticed from Fig. 4-3 that the steepness and the magnitude of the transients decrease as they propagate to the inverter end.

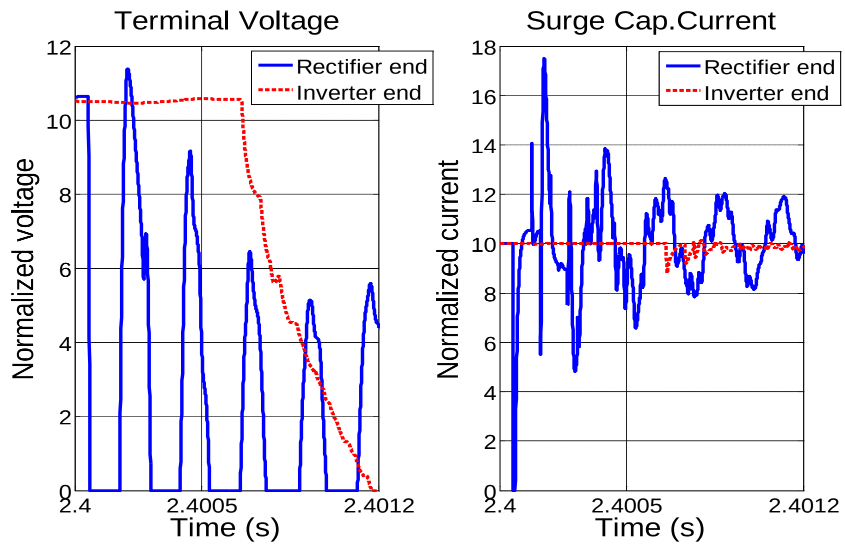

Fig. 4-3 - Monitored input signals conditioned by A/D for a fault occurred 16 km away from rectifier terminal

4.6.2 Identification: Faulty-line segment using simulation results

The proposed algorithm was verified with solid line-to-ground faults created at different locations on the transmission lines and the cable. The faulty segment was identified by calculating x_{F1}, x_{F2}, and x_{F3} using Eq. 4-4, Eq. 4-8 and Eq. 4-9. Next, the values of x_{F1}, x_{F2}, and x_{F3} are compared with the corresponding segment lengths, 27 km, 44 km and 97 km. Table 4-1 summarizes the calculated x_{F1}, x_{F2}, and x_{F3} values for different fault locations using the simulation data. As an example when the fault is 70 km away from the rectifier end, calculated values for x_{F1}, x_{F2}, and x_{F3} are 113.57 km, 42.94 km and -2.14 km respectively. Only x_{F2} lies between zero and the corresponding segment length of 44 km. Therefore, the fault is in the cable segment.

Table 4-1 - Calculated values of x_{F1}, x_{F2}, and x_{F3} for different fault locations

	Fault location (km)					
	5	26	49	70	91	167
$0 \leq x_{F1} \leq 27$	5.07	25.97	71.26	113.57	135.51	211.22
$0 \leq x_{F2} \leq 44$	-10.88	-0.51	21.95	42.94	53.82	91.38
$0 \leq x_{F3} \leq 97$	-111.14	-90.15	-44.65	-2.14	19.89	95.94

4.6.3 Fault-location results

Fault-location error calculated using Eq. 4-17 was used as a performance index.

$$\% \, error = \frac{|estimated\ fault\ location - actual\ fault\ location|}{Total\ length\ of\ the\ HVDC\ line} \qquad \text{Eq. 4-17}$$

Table 4-2 summarizes the fault-location results obtained with terminal voltage as the input. The first two faults are in the first OH line, the second two faults are in the cable, and the last two faults are the second OH line segment. Fault locations were calculated using CWT coefficients of different scales. The best results were obtained with scale-32, with a maximum error of 0.06% or 0.11 km. The highest error of 0.22% was observed with scale-128.

Table 4-2 - Predicted fault-location and estimation errors with terminal voltage

	Scale							
	16		32		64		128	
Actual fault loc.	Est. fault loc.	Error (%)	Est. fault loc.	Error (%)	Est. fault loc.	Error (%)	Est. fault loc.	Error (%)
5.00	5.15	0.09	5.07	0.04	5.09	0.05	5.28	0.17
26.00	25.89	0.06	25.97	0.02	25.73	0.16	25.64	0.22
49.00	49.00	0.00	48.95	0.03	48.96	0.02	48.99	0.00
70.00	70.04	0.02	69.94	0.03	69.98	0.01	70.09	0.05
91.00	90.97	0.02	90.89	0.06	90.98	0.01	91.21	0.13
167.00	166.75	0.15	166.94	0.03	166.88	0.07	166.68	0.19

Table 4-3 - Predicted fault-location and estimation errors with surge capacitor current

	Scale							
	16		32		64		128	
Actual fault loc.	Est. fault loc.	Error (%)	Est. fault loc.	Error (%)	Est. fault loc.	Error (%)	Est. fault loc.	Error (%)
5.00	4.96	0.03	4.96	0.03	5.13	0.08	5.13	0.08
26.00	26.07	0.04	25.99	0.00	25.91	0.06	25.98	0.01
49.00	49.01	0.01	49.01	0.01	49.07	0.04	49.06	0.04
70.00	69.96	0.02	69.96	0.02	70.17	0.10	70.08	0.05
91.00	90.94	0.04	91.01	0.01	91.23	0.14	91.08	0.05
167.00	167.03	0.02	167.03	0.02	166.70	0.18	166.89	0.07

Table 4-3 summarizes the fault-location results with surge capacitor current as the input. Again, the best results were obtained with scale-32, with maximum error of 0.03% or 0.04 km. The highest error of 0.18% was again observed with scale-128. According to the results, both the surge capacitor current and terminal voltage measurements results in similarly accurate fault-location predictions.

4.7 Fault-location with noisy inputs

In order to examine the robustness of the proposed fault-location algorithm, fault-location performance was tested with input signals contaminated with noise. As an example, Fig. 4-4 shows rectifier terminal voltage and surge capacitor current contaminated with noise. In Fig. 4-4 (a), rectifier end voltage with added 0.001 pu white noise is compared with the clean signal. In Fig. 4-4 (b), the same signal with 0.01 pu white noise is shown. Fig. 4-4 (c) and (d) compare the rectifier end surge capacitor current with 0.001 kA and 0.01 kA noise respectively with the clean signal.

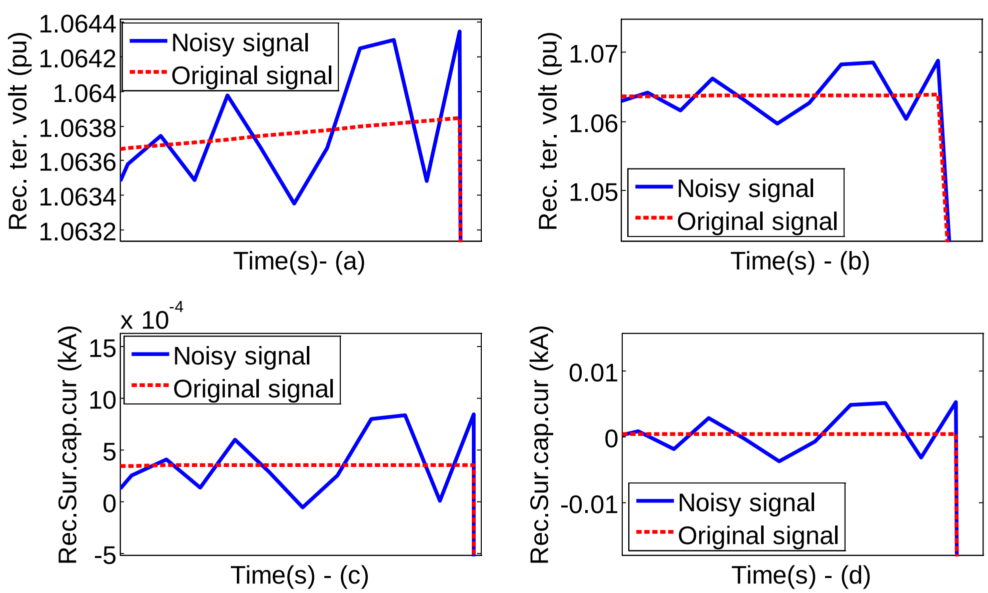

Fig. 4-4 - Surge capacitor current and terminal voltage with added white noise

Results of the fault-location algorithm using the terminal voltages contaminated with 0.001 pu of noise are listed in Table 4-4. Table 4-5 shows the corresponding results with 0.01 pu noise. Although the accuracy decreases with the noise level, it is possible to locate the faults with satisfactory accuracy, even with noisy inputs. The best results are obtained with scale-32 and the corresponding maximum error with 0.01 pu noise was 0.17%.

Table 4-4 - Predicted fault-location and estimation errors with terminal voltage contaminated with 0.001 pu noise

	Scale							
	16		32		64		128	
Actual fault loc.	Est. fault loc.	Error (%)	Est. fault loc.	Error (%)	Est. fault loc.	Error (%)	Est. fault loc.	Error (%)
5.00	5.24	0.14	5.15	0.09	5.34	0.20	5.28	0.17
26.00	25.81	0.11	25.82	0.11	25.65	0.21	25.64	0.22
49.00	49.01	0.01	49.04	0.02	49.03	0.02	48.99	0.00
70.00	70.07	0.04	70.11	0.07	70.15	0.09	70.09	0.05
91.00	91.13	0.08	91.17	0.10	91.20	0.12	91.21	0.13
167.00	166.62	0.23	166.83	0.10	166.56	0.26	166.68	0.19

Table 4-5 - Predicted fault-location and estimation errors with terminal voltage contaminated with 0.01 pu noise

	Scale							
	16		32		64		128	
Actual fault loc.	Est. fault loc.	Error (%)	Est. fault loc.	Error (%)	Est. fault loc.	Error (%)	Est. fault loc.	Error (%)
5.00	5.43	0.25	5.15	0.09	5.66	0.39	5.37	0.22
26.00	25.71	0.17	25.72	0.17	25.49	0.30	25.34	0.39
49.00	49.08	0.05	49.02	0.01	49.10	0.06	49.02	0.01
70.00	70.19	0.11	70.05	0.03	70.36	0.21	70.19	0.11
91.00	91.36	0.21	91.15	0.09	91.64	0.38	91.45	0.27
167.00	166.27	0.43	166.74	0.15	166.18	0.49	166.51	0.29

Performance of the fault-location algorithm with noise contaminated surge capacitor currents are given in Table 4-6 and Table 4-7. The observations are similar to those obtained with the voltage measurements. These results again confirm (i) robustness of the proposed method against the noise, (ii) suitability of both input signals for detection of surges, (iii) there is no significant difference between the performance with two input quantities even under noisy situations.

Table 4-6 - Predicted fault-location and estimation errors with surge capacitor current contaminated with 0.001 kA noise

	Scale							
	16		32		64		128	
Actual fault loc.	Est. fault loc.	Error (%)	Est. fault loc.	Error (%)	Est. fault loc.	Error (%)	Est. fault loc.	Error (%)
5.00	4.96	0.03	5.21	0.12	5.05	0.03	5.13	0.08
26.00	26.07	0.04	25.91	0.06	25.98	0.01	25.98	0.01
49.00	49.01	0.01	49.07	0.04	49.02	0.01	49.06	0.04
70.00	69.96	0.02	70.14	0.08	70.04	0.02	70.08	0.05
91.00	91.01	0.01	91.23	0.14	91.03	0.02	91.08	0.05
167.00	167.10	0.06	166.78	0.13	166.89	0.06	166.89	0.07

Table 4-7 - Predicted fault-location and estimation errors with surge capacitor current contaminated with 0.01 kA noise

	Scale							
	16		32		64		128	
Actual fault loc.	Est. fault loc.	Error (%)	Est. fault loc.	Error (%)	Est. fault loc.	Error (%)	Est. fault loc.	Error (%)
5.00	4.97	0.02	5.22	0.13	5.39	0.23	5.24	0.14
26.00	26.05	0.03	25.89	0.06	25.74	0.16	25.73	0.16
49.00	48.98	0.01	49.00	0.00	49.06	0.04	49.01	0.01
70.00	69.94	0.03	70.07	0.04	70.25	0.15	70.07	0.04
91.00	90.95	0.03	91.12	0.07	91.40	0.24	91.13	0.08
167.00	167.01	0.00	166.83	0.10	166.50	0.30	166.62	0.23

4.8 Fault-location performance for high impedance faults

The performance of the fault-location algorithm is tested with high impedance line-to-ground faults. Table 4-8 summarizes the results of the algorithm for high impedance dc line faults. Results are shown for faults with two different fault resistance values, 10 Ω and 100 Ω. Note that the voltage measurements were assumed to be contaminated with a 0.001 pu noise while current measurements were assumed to be contaminated with 0.001 kA. Only the results obtained using Scale-32 CWT coefficients are shown as Scale-32 CWT coefficients were consistently giving the best results. Based on the results in Table 4-8, it can be concluded that the proposed method works well even with the high impedance faults.

Table 4-8 - Predicted fault-location and estimation errors for high impedance faults using scale-32 CWT coefficients

	Voltage				Surge Cap Current			
	10 Ω		100 Ω		10 Ω		100 Ω	
Actual fault loc.	Est. fault loc.	Err. (%)	Est. fault loc.	Err. (%)	Est. fault loc.	Err. (%)	Est. fault loc.	Err. (%)
5.00	5.15	0.09	5.08	0.05	5.21	0.12	5.21	0.12
26.00	25.82	0.11	25.74	0.15	25.91	0.06	25.91	0.06
49.00	49.04	0.02	49.00	0.00	49.07	0.04	49.07	0.04
70.00	70.08	0.05	70.08	0.05	70.17	0.10	70.17	0.10
91.00	91.17	0.10	91.09	0.06	91.23	0.14	91.23	0.14
167.00	166.83	0.10	166.90	0.06	166.78	0.13	166.78	0.13

4.9 Theoretical extension of the algorithm to an 'n'-segment HVDC transmission system

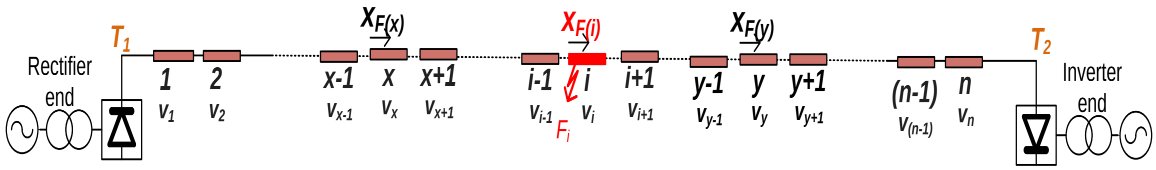

Fig. 4-5 - HVDC system with "n" number of line segments where fault is in i^{th} segment

Fig. 4-5 illustrates an HVDC scheme with "n" different transmission segments which have segment lengths of L_1, L_2, .., L_{n-1}, L_n and propagation velocities of v_1, v_2, .., v_{n-1}, v_n. In order to derive an expression for the fault-location in this general case, consider a case where a fault in Segment "i".

If x_{Fi} is calculated in terms of the surge-arrival time difference for the fault F_i

$$x_{Fi} = \left(\Delta t_{12-Fi} - \frac{L_1}{v_1} - \frac{L_2}{v_2} - \cdots - \frac{L_{x-1}}{v_{x-1}} - \frac{L_x}{v_x} - \frac{L_{x+1}}{v_{x+1}} \ldots - \frac{L_{i-1}}{v_{i-1}} + \frac{L_i}{v_i} + \frac{L_{i+1}}{v_{i+1}} \ldots + \frac{L_{y-1}}{v_{y-1}} + \frac{L_y}{v_y} + \frac{L_{y+1}}{v_{y+1}} \ldots + \frac{L_n}{v_n}\right) \times \frac{v_i}{2} \qquad \text{Eq. 4-18}$$

Since the actual fault-location is initially unknown and only the surge-arrival time difference is available; one may assume the fault is in segment "x" and calculate the fault-location x_{Fx} using the surge-arrival time difference as,

$$x_{Fx} = \left(\Delta t_{12-Fi} - \frac{L_1}{v_1} - \frac{L_2}{v_2} - \cdots - \frac{L_{x-1}}{v_{x-1}} + \frac{L_x}{v_x} + \frac{L_{x+1}}{v_{x+1}} \ldots + \frac{L_{i-1}}{v_{i-1}} + \frac{L_i}{v_i} + \frac{L_{i+1}}{v_{i+1}} \ldots + \frac{L_{y-1}}{v_{y-1}} + \frac{L_y}{v_y} + \frac{L_{y+1}}{v_{y+1}} \ldots + \frac{L_n}{v_n}\right) \times \frac{v_x}{2} \qquad \text{Eq. 4-19}$$

If x_{Fx} rewrites in terms of x_{Fi}, *(actual fault-location)*

$$x_{Fx} = \left(\left[\frac{2x_{Fi}}{v_i} + \left\{\frac{L_x}{v_x} + \frac{L_{x+1}}{v_{x+1}} \dots + \frac{L_{i-1}}{v_{i-1}}\right\}\right.\right.$$

$$\left.- \left\{\frac{L_i}{v_i} + \frac{L_{i+1}}{v_{i+1}} \dots + \frac{L_{y-1}}{v_{y-1}} + \frac{L_y}{v_y} + \frac{L_{y+1}}{v_{y+1}} \dots + \frac{L_n}{v_n}\right\}\right] + \frac{L_x}{v_x} + \frac{L_{x+1}}{v_{x+1}} \dots \qquad \text{Eq. 4-20}$$

$$\left. + \frac{L_{i-1}}{v_{i-1}} + \frac{L_i}{v_i} + \frac{L_{i+1}}{v_{i+1}} \dots + \frac{L_{y-1}}{v_{y-1}} + \frac{L_y}{v_y} + \frac{L_{y+1}}{v_{y+1}} \dots + \frac{L_n}{v_n}\right) \times \frac{v_x}{2}$$

$$x_{Fx} = \left(\left[\frac{2x_{Fi}}{v_i} + 2\left\{\frac{L_x}{v_x} + \frac{L_{x+1}}{v_{x+1}} \dots + \frac{L_{i-1}}{v_{i-1}}\right\}\right]\right) \times \frac{v_x}{2}$$

$$x_{Fx} = L_x + \underbrace{\left(\left[\frac{2x_{Fi}}{v_i} + 2\left\{\frac{L_{x+1}}{v_{x+1}} \dots + \frac{L_{i-1}}{v_{i-1}}\right\}\right]\right) \times \frac{v_x}{2}}_{\geq 0}$$

$$x_{Fx} \geq L_x \qquad \text{Eq. 4-21}$$

Similarly, one could assume the fault is in segment "*y*" and calculate the fault-location x_{Fy} using the surge-arrival time difference as,

$$x_{Fy} = \left(\Delta t_{12-Fi} - \frac{L_1}{v_1} - \frac{L_2}{v_2} - \dots - \frac{L_{x-1}}{v_{x-1}} - \frac{L_x}{v_x} - \frac{L_{x+1}}{v_{x+1}} \dots - \frac{L_{i-1}}{v_{i-1}} - \frac{L_i}{v_i}\right. \qquad \text{Eq. 4-22}$$

$$\left. - \frac{L_{i+1}}{v_{i+1}} \dots - \frac{L_{y-1}}{v_{y-1}} + \frac{L_y}{v_y} + \frac{L_{y+1}}{v_{y+1}} \dots + \frac{L_n}{v_n}\right) \times \frac{v_y}{2}$$

$$x_{Fy} = \left(\left[\frac{2x_{Fi}}{v_i} - \left\{\frac{L_i}{v_i} + \frac{L_{i+1}}{v_{i+1}} + \cdots + \frac{L_{y-1}}{v_{y-1}} + \frac{L_y}{v_y} + \frac{L_{y+1}}{v_{y+1}} \ldots + \frac{L_n}{v_n}\right\}\right] - \frac{L_i}{v_i} - \frac{L_{i+1}}{v_{i+1}} \ldots \right.$$
$$\left. - \frac{L_{y-1}}{v_{y-1}} + \frac{L_y}{v_y} + \frac{L_{y+1}}{v_{y+1}} \ldots + \frac{L_n}{v_n}\right) \times \frac{v_y}{2}$$

$$x_{Fy} = \left(\left[\frac{2x_{Fi}}{v_i} - 2\left\{\frac{L_i}{v_i} + \frac{L_{i+1}}{v_{i+1}} \ldots + \frac{L_{y-1}}{v_{y-1}} + \frac{L_y}{v_y} + \frac{L_{y+1}}{v_{y+1}} + \cdots + \frac{L_n}{v_n}\right\}\right]\right) \times \frac{v_y}{2}$$
$$x_{Fx} = \left(\left[\underbrace{\frac{x_{Fi} - L_i}{v_i}}_{\leq 0} - \left\{\frac{L_{i+1}}{v_{i+1}} \ldots + \frac{L_{y-1}}{v_{y-1}} + \frac{L_y}{v_y} + \frac{L_{y+1}}{v_{y+1}} + \cdots + \frac{L_n}{v_n}\right\}\right]\right) \times v_y$$

$$x_{Fx} \leq 0 \qquad \text{Eq. 4-23}$$

Therefore, Eq. 4-21 and Eq. 4-23 show the calculated fault locations are not within the respective line length. In this case, only x_{Fi} should lie between ‘zero’ and L_i. Therefore, this method can be extended for an HVDC system with *n*-number of segments. All other possibilities (x_{F1}, x_{F2}, … x_{Fi-1}, x_{Fi+1}, … x_{Fn}) calculated using the corresponding time difference, $\Delta t_{12\text{-}Fi}$, will lie outside their valid ranges.

4.10 Concluding remarks

An algorithm to locate faults on an HVDC transmission system consisting of segments of cables and overhead lines using only the terminal measurements was proposed in this Chapter. The proposed algorithm that uses the two-terminal travelling-wave fault-location principle has the ability to correctly identify the faulted line segment using only the measurements at two ends.

Application of the proposed fault-location method to an HVDC system consisting of two overhead line segments and one cable segment was demonstrated through simulations. The simulation results verified the correct operation of the fault-location algorithm. According to the simulation results, it is possible to achieve a fault-location accuracy of ± 400 m for the test system considered. Further simulations showed that the proposed method performs well under the presence of measurement noise even for the high impedance faults. The analysis, which considered the scaling and quantization effects of the A/D conversion, indicated that either the terminal voltage or the surge capacitor current could be used as the input signal, and in both cases, Scale-32 CWT coefficients (calculated at 2 MHz sampling rate) are the best for detecting surge-arrival time.

The proposed method eliminates the need for the installation of LFL detection stations at the ends of each OH line section, and provides an indication of the location of the fault even when it is inside the cable section. Although the method is described using a three section HVDC transmission system, it can be generalized to an *n*-section HVDC transmission system.

Chapter 5

Fault-location in star-connected multi-terminal HVDC schemes

5.1 Introduction

Multi-terminal HVDC (MTHVDC) technology based on voltage-source converters (VSC) is expected to be widely used for the interconnection of on-shore wind farms like the Atlantic wind connection [35], as well as in underground urban sub-transmission systems as proposed in [36], and off shore renewable generation systems as discussed in [5] and [37]. Multi-terminal HVDC systems which have more than two converters connected to a common HVDC system can have different topologies such as point to point, general ring and star topologies [5][37].

When a line fault occurs in a multi-terminal HVDC scheme, the primary protection must activate and isolate the faulted line segment. Several methods to identify the faulty line in a multi-terminal VSC HVDC network with mesh topology are proposed in [5] and [19]. These methods, which are based on the current and voltage measurements at the converter terminals, have been primarily developed for protection purposes. However, in case of a permanent dc line fault, determination of the exact fault-location is essential for carrying out the repairs. If this can be achieved without any additional tests, repair crews can be dispatched immediately ensuring faster network restoration.

Consider a star network topology, where the fault-location can be achieved by using the existing two-terminal travelling-wave based fault locators with synchronized measurements, if fault locators are placed at all the terminals and at the common point. However, installing a fault locator at the star point requires additional equipment as well as communication infrastructure, and therefore incurs additional costs.

Several algorithms based on the travelling-wave principle have been proposed for fault-location in ac transmission networks [38] - [45]. The ‘teed’ circuit-protection algorithms proposed in [38] and [40] relies on the secondary reflections to locate the faulty line. Therefore, the accuracy of the fault-location can be degraded due to multiple and superimposed reflections and refractions of travelling waves, although such algorithms are advantageous when synchronized measurements are not available. In those algorithms, wave fronts are identified using auto and cross correlation. The benefits of applying wavelet transform to identify the wave front arrival time were explained in chapter 2 and 3. In ac transmission systems, post fault voltages and currents of the line within the first 5ms are used to find the fault-location in [41]. This may not be feasible in HVDC systems, due to the presence of fast acting protection. In [42] and [43], discrete wavelet transform is used to identify the wave front arrival time and Dijkstra’s shortest path algorithm is adapted to identify the fault-location. The advantage of using continuous wavelet transform over discrete wavelet transform to identify the wave-front arrival time is discussed in Chapter 2. The method proposed to use in ac network fault-location in [45] also uses discrete wavelet transform to identify the fault arrival time and uses line length comparison criterion to identify the faulty segment.

In this chapter, the novel method to locate dc line faults in a star connected multi-terminal HVDC system is proposed. This method is based on the two-terminal travelling-wave principle and only requires the measurement of the initial surge-arrival times at all the terminals. This algorithm is initially derived for a three-terminal network. However, theoretically, the algorithm can be extended to a star connected multi-terminal HVDC network with any number of terminals.

5.2 Development of the algorithm for fault-location method in star connected three terminal HVDC transmission system

A three-terminal HVDC system with a star topology is shown in Fig. 5-1 (a). The three VSCs are labelled as *A*, *B* and *C*. These converters are connected to a common point *D* via three dc lines (*AD*, *BD* and *CD*). The lengths of the dc lines are L_1, L_2 and L_3 respectively.

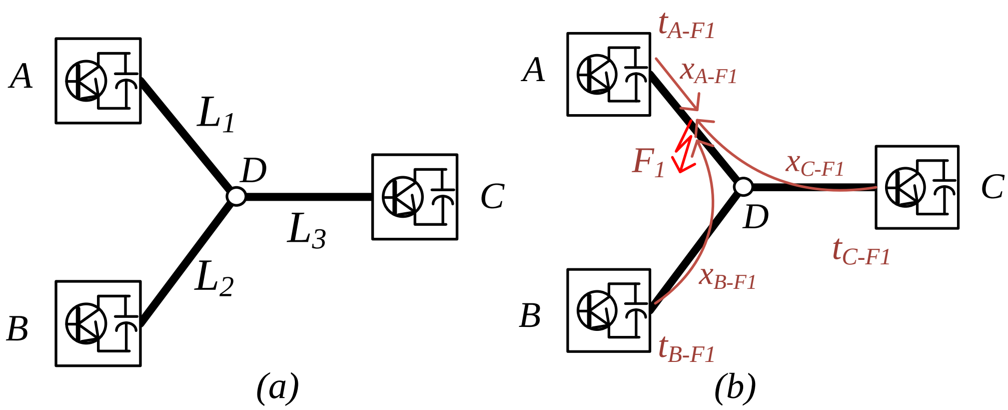

Fig. 5-1 - (a) Star connected three-terminal HVDC system (b) dc line fault F_1 inside line *AD*

An arbitrary dc line fault is shown in Fig. 5-1(b). The distance to the fault is calculated from each converter terminal. For example, $x_{A\text{-}F1}$, $x_{B\text{-}F1}$ and $x_{C\text{-}F1}$ are the distances to fault F_1 from terminals *A*, *B* and *C* respectively. Assume that the fault occurs at time $t=0$, and that the time of arrival of the initial travelling-wave at terminals *A*, *B* and *C* are given by $t_{A\text{-}F1}$, $t_{B\text{-}F1}$ and $t_{C\text{-}F1}$ respectively. Each of these travel times can be expressed in terms of the dc transmission line lengths and $x_{A\text{-}F1}$ as follows:

$$t_{A-F1} = \left(\frac{x_{A-F1}}{v_1}\right) \qquad \text{Eq. 5-1}$$

$$t_{B-F1} = \left(\frac{L_1 - x_{A-F1}}{v_1}\right) + \left(\frac{L_2}{v_2}\right) \qquad \text{Eq. 5-2}$$

$$t_{C-F1} = \left(\frac{L_1 - x_{A-F1}}{v_1}\right) + \left(\frac{L_3}{v_3}\right) \qquad \text{Eq. 5-3}$$

Where v_1, v_2 and v_3 are the travelling-wave propagation velocities of the dc transmission line sections *AD*, *BD* and *CD* respectively. In obtaining Eq. 5-1 to Eq. 5-3, it is assumed that the fault is inside the *AD* line. By subtracting Eq. 5-2 from Eq. 5-1, we can obtain an expression for the difference between surge-arrival times at terminals *A* and *B*:

$$\Delta t_{AB-F1} = t_{A-F1} - t_{B-F1} = \frac{2 \cdot x_{A-F1}}{v_1} - \frac{L_1}{v_1} - \frac{L_2}{v_2} \qquad \text{Eq. 5-4}$$

Similarly, by subtracting Eq. 5-3 from Eq. 5-1, the difference between surge-arrival times at terminals *A* and *C* can be obtained as:

$$\Delta t_{AC-F1} = t_{A-F1} - t_{C-F1} = \frac{2 \cdot x_{A-F1}}{v_1} - \frac{L_1}{v_1} - \frac{L_3}{v_3} \qquad \text{Eq. 5-5}$$

Two estimations for the distance to the fault from terminal *A* can be obtained in terms of $\Delta t_{AB\text{-}F1}$ and $\Delta t_{AC\text{-}F1}$.

$$x_{A-F1} = \left(\Delta t_{AB-F1} + \frac{L_1}{v_1} + \frac{L_2}{v_2}\right) \times \frac{v_1}{2} \qquad \text{Eq. 5-6}$$

$$x_{A-F1} = \left(\Delta t_{AC-F1} + \frac{L_1}{v_1} + \frac{L_3}{v_3}\right) \times \frac{v_1}{2} \qquad \text{Eq. 5-7}$$

If $\Delta t_{AB\text{-}F1}$ and $\Delta t_{AC\text{-}F1}$ can be obtained through GPS based measurements, then the fault can be located with known propagation velocities. Note that the values of $\Delta t_{AB\text{-}F1}$ and $\Delta t_{AC\text{-}F1}$ can be negative depending on the line lengths and the fault-location. Regardless, the distance to the fault from terminal '*A'* will always be correctly given if the time differences are computed as in Eq. 5-4 and Eq. 5-5.

In the above case the fault was inside the dc line Section *AD*. Now consider fault F_2 which is in the line Section *BD* as indicated on Fig. 5-2 (a). Again, assume that the fault occurs at the instant $t=0$.

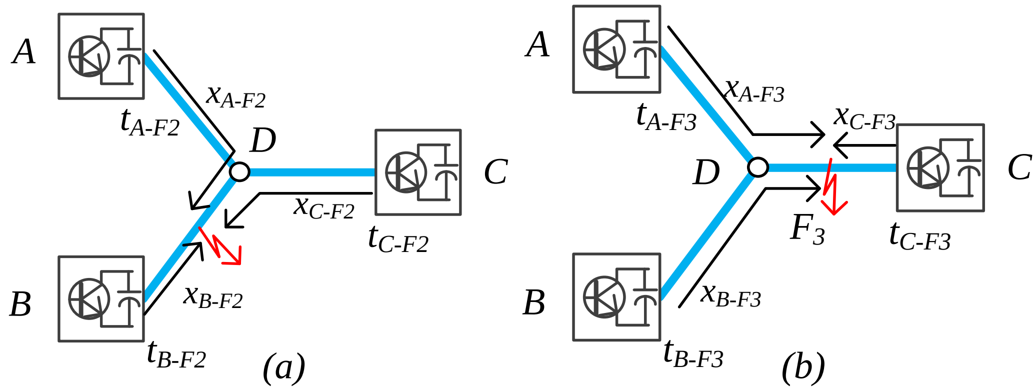

Fig. 5-2 - (a) dc line fault F_2 inside the *BD* line (b) dc line fault F_3 inside the *CD* line

Following the same convention for notations, the respective surge-arrival times at terminals *A*, *B* and *C* can be expressed by Eq. 5-8, Eq. 5-9 and Eq. 5-10.

$$t_{B-F2} = \left(\frac{x_{B-F2}}{v_2}\right) \quad \text{Eq. 5-8}$$

$$t_{A-F2} = \left(\frac{L_2 - x_{B-F2}}{v_2}\right) + \left(\frac{L_1}{v_1}\right) \quad \text{Eq. 5-9}$$

$$t_{C-F2} = \left(\frac{L_2 - x_{B-F2}}{v_2}\right) + \left(\frac{L_3}{v_3}\right) \quad \text{Eq. 5-10}$$

As in the previous case, two estimations for the distance to the fault from terminal *B* can be obtained in terms of $\Delta t_{BA\text{-}F2}$ and $\Delta t_{BC\text{-}F2}$, which are the differences between the initial surge-arrival times at terminals *B* and *A*, and terminals *B* and *C*.

$$x_{B-F2} = \left(\Delta t_{BA-F2} + \frac{L_2}{v_2} + \frac{L_1}{v_1}\right) \times \frac{v_2}{2} \quad \text{Eq. 5-11}$$

$$x_{B-F2} = \left(\Delta t_{BC-F2} + \frac{L_2}{v_2} + \frac{L_3}{v_3}\right) \times \frac{v_2}{2} \quad \text{Eq. 5-12}$$

Similarly, for a fault on the dc line Section *CD* as in Fig. 5-2 (b), two estimations for the distance to the fault from terminal *C* can be obtained as:

$$x_{C-F3} = \left(\Delta t_{CA-F3} + \frac{L_3}{v_3} + \frac{L_1}{v_1}\right) \times \frac{v_3}{2} \quad \text{Eq. 5-13}$$

$$x_{C-F3} = \left(\Delta t_{CB-F3} + \frac{L_3}{v_3} + \frac{L_2}{v_2}\right) \times \frac{v_3}{2} \qquad \text{Eq. 5-14}$$

Where $\Delta t_{CA\text{-}F3}$ and $\Delta t_{CB\text{-}F3}$ are the differences between the initial surge-arrival times at terminals *C* and *A*, and terminals *C* and *B* respectively.

5.3 Identification: Correct faulty dc line

In deriving the expressions Eq. 5-6 - Eq. 5-7 and Eq. 5-11 - Eq. 5-14 for the distance to a fault, it was assumed that the faulted dc line section is known. However, in a practical fault-location problem, this is unknown. The only measurable quantities are the differences between the surge-arrival times. Thus, it is necessary to identify the faulted dc line before being able to pinpoint the exact location of the fault. This can be achieved by the procedure described below.

When a fault is detected, two estimations for the fault-location are calculated using Eq. 5-6 and Eq. 5-7, assuming that the fault is inside dc line Section *AD*. Then two more estimations for the fault-location are calculated using Eq. 5-11 and Eq. 5-12, assuming that the fault is inside dc line Section *BD*. Finally, two more fault-location values are calculated using the surge-arrival time difference measurements by using Eq. 5-13 and Eq. 5-14, assuming that the fault is inside dc line Section *CD*. Next, the pair of calculated fault-location values under each assumption are compared with each other for consistency. For example, if the assumption that the fault is inside the dc line Section *AD* is correct, then the fault distances calculated from Eq. 5-6 and Eq. 5-7 have to be the same. Furthermore, for this fault, the fault distances calculated from Eq. 5-11 and Eq. 5-12 will not be the same, since the underlying assumptions for Eq. 5-11 and Eq. 5-12 are not true.

The same is true regarding the fault distances estimated from Eq. 5-13 and Eq. 5-14. Hence, the faulted line segment can be identified without any ambiguity.

Fig. 5-3 shows the method used to identify the faulty dc line in detail and how the fault-location is calculated. Assume the surge-arrival times at the three terminals t_A, t_B and t_C in Fig. 5-3 are known. Moreover, all the terminal measurement devices are assumed identical and hence the errors due to time delays in these devices can be assumed to be cancelled when calculating the time differences. This is one attractive feature in the proposed algorithm. Then using Eq. 5-15 to Eq. 5-20, three pairs of possible fault locations are calculated by using six different wave-front arrival time differences.

$$x_{A1} = \left(\Delta t_{AB} + \frac{L_1}{v_1} + \frac{L_2}{v_2}\right) \times \frac{v_1}{2} \qquad \text{Eq. 5-15}$$

$$x_{A2} = \left(\Delta t_{AC} + \frac{L_1}{v_1} + \frac{L_3}{v_3}\right) \times \frac{v_1}{2} \qquad \text{Eq. 5-16}$$

$$x_{B1} = \left(\Delta t_{BA} + \frac{L_2}{v_2} + \frac{L_1}{v_1}\right) \times \frac{v_2}{2} \qquad \text{Eq. 5-17}$$

$$x_{B2} = \left(\Delta t_{BC} + \frac{L_2}{v_2} + \frac{L_3}{v_3}\right) \times \frac{v_2}{2} \qquad \text{Eq. 5-18}$$

$$x_{C1} = \left(\Delta t_{CA} + \frac{L_3}{v_3} + \frac{L_1}{v_1}\right) \times \frac{v_3}{2} \qquad \text{Eq. 5-19}$$

$$x_{C2} = \left(\Delta t_{CB} + \frac{L_3}{v_3} + \frac{L_2}{v_2}\right) \times \frac{v_3}{2} \qquad \text{Eq. 5-20}$$

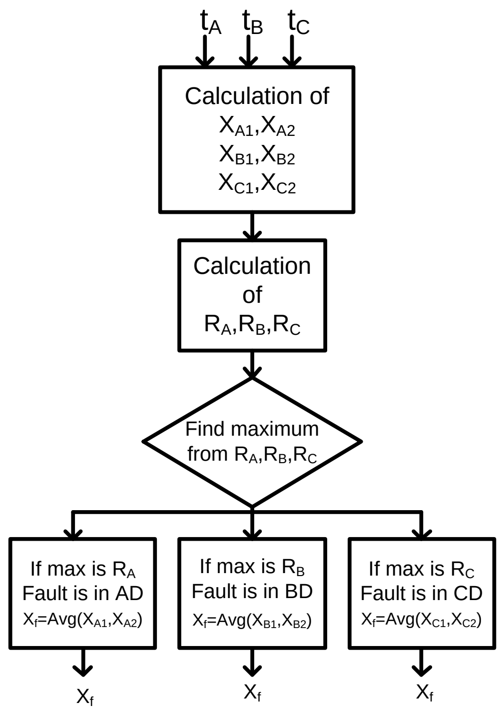

Fig. 5-3 - Faulty segment identification and fault calculation method

In calculating each pair of fault locations, the assumption is that the fault is in the line segment directly connected to the considered terminal. For example, in calculating x_{C1} and x_{C2}, it is assumed that fault is in line section *CD*. Then the ratio between the smaller and the larger values of the estimated fault location is calculated for each pair:

$$R_A = \frac{minimum(|x_{A1}|, |x_{A2}|)}{maximum(|x_{A1}|, |x_{A2}|)} \qquad \text{Eq. 5-21}$$

$$R_B = \frac{minimum(|x_{B1}|, |x_{B2}|)}{maximum(|x_{B1}|, |x_{B2}|)} \qquad \text{Eq. 5-22}$$

$$R_C = \frac{minimum(|x_{C1}|, |x_{C2}|)}{maximum(|x_{C1}|, |x_{C2}|)} \qquad \text{Eq. 5-23}$$

The ratio R_T (where $T = A, B, or\ C$) is equal to one when the two calculated values are equal, that is when the underline assumption is true as pointed out above. This ratio is less than one for the remaining two cases. However in actual situations, the ratio for the correct pair is not exactly equal to one but a value closer to one due to numerical and measurement errors. Therefore, the terminal with the highest R_T values is considered as the terminal closest to the fault. Then the fault-location (x_f) is calculated by taking the average value of the two possible fault-location values of the corresponding selected terminal as shown in Eq. 5-24.

$$X_f = 0.5(X_{T^*1} + X_{T^*2}) \qquad \text{Eq. 5-24}$$

5.4 Calibration of the system

The accuracy of fault-location prediction is dependent on the accuracy of the propagation velocity. Even though the theoretical value for the propagation velocity can be estimated from the conductor geometry, the best approach is to estimate these values using the measurements obtained during the commissioning of the line fault-location system.

A systematic method for calibrating propagation velocities of a three-terminal HVDC system is proposed in this section. This approach requires conducting three test faults, one on each line segment at known locations. In order to simplify the equations, substitute variables λ_1, λ_2, and λ_3 represent the inverse of the propagation velocities.

$$\lambda_1 = \frac{1}{v_1}, \quad \lambda_2 = \frac{1}{v_2} \quad \text{and} \quad \lambda_3 = \frac{1}{v_3} \qquad \text{Eq. 5-25}$$

The measured surge-arrival time differences corresponding to the faults on segments 1, 2 and 3 respectively are given by:

$$\Delta t_{AB-F1} = \lambda_1(2x_{F1} - L_1) + \lambda_2(-L_2) + \lambda_3(0) \quad \text{Eq. 5-26}$$

$$\Delta t_{BA-F2} = \lambda_1(-L_1) + \lambda_2(2x_{F2} - L_2) + \lambda_3(0) \quad \text{Eq. 5-27}$$

$$\Delta t_{CB-F3} = \lambda_1(0) + \lambda_2(-L_2) + \lambda_3(2x_{F3} - L_3) \quad \text{Eq. 5-28}$$

This set of equations can be expressed in matrix form,

$$\begin{bmatrix} (2x_{F1} - L_1) & (-L_2) & 0 \\ (-L_1) & (2x_{F2} - L_2) & 0 \\ 0 & (-L_2) & (2x_{F3} - L_3) \end{bmatrix} \begin{bmatrix} \lambda_1 \\ \lambda_2 \\ \lambda_3 \end{bmatrix} = \begin{bmatrix} \Delta t_{AB-F1} \\ \Delta t_{BA-F2} \\ \Delta t_{CB-F3} \end{bmatrix} \quad \text{Eq. 5-29}$$

Solution of Eq. 5-29 with test data (with known x_{Fi} and Δt values) yields λ_i values, inversion of which give the propagation velocities. Often it is not practical to place test faults in the middle of lines, especially if they are cables. In such situations, the test faults can be placed at the terminals and the star point. For example, if the first fault is placed at the terminal A, then $x_{F1}=0$, and if the second fault is placed at the star point $x_{F2}=L_2$. Moreover, we can use the same data obtained for the second fault as inputs in equation Eq. 5-28 and hence $x_{F3}=L_3$.

5.5 Identification of the fault arrival time

According to simulations it was found that for a dc line fault on a VSC based HVDC system, a steep wave front appears on the dc line current. Nevertheless, at the moment it is not economical to install high bandwidth transducers to measure series dc line currents. However, if it is measurable, dc line current can be used to detect the arrival of the wave fronts.

Technically, VSC HVDC systems do not require a dc smoothing reactor for its functionality. Therefore, to the dc line, a VSC converter appears as an ideal voltage source due to the large dc bus capacitor. Thus, a clear surge will not be visible in the terminal voltage (*or in the surge capacitor current, if one is connected*) [46]. However, in practice, an inductor is installed between the dc bus and the converter to reduce the high rate of change of currents through Insulated-gate bipolar transistors (IGBT) during a dc line fault. Investigations in [46] showed that current measurements through a surge capacitor can be used to detect wave fronts in VSC based HVDC schemes provided that a small series inductor is present between the line and converter terminal as shown in Fig. 5-4.

Therefore initial travelling-wave arrival times can be obtained by analyzing the CWT coefficients of the measured terminal surge capacitor current signals.

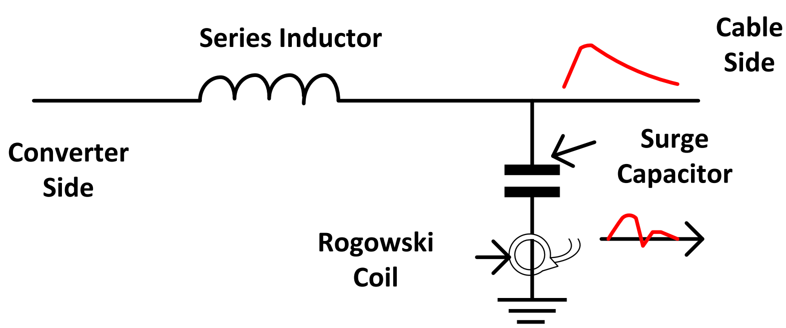

Fig. 5-4 - Surge detection system for VSC HVDC systems (Redrawn from [46])

Therefore, the CWT based surge-arrival time identification method discussed in Chapter 2 can be applied to VSC based HVDC systems.

5.6 Simulated case study

5.6.1 Simulation model

A star connected three-terminal VSC based HVDC system was used in simulation studies. The schematic diagram of the test network is shown in Fig. 5-5 (a). All the simulations were carried out with PSCAD/EMTDC and the fault-location algorithm was implemented in MATLAB.

The HVDC transmission line consists of three Over Head (OH) line segments of 27 km, 44 km and 97 km in lengths. The tower structure is shown in Fig. 5-6. OH lines are represented using distributed parameter transmission line models in PSCAD/EMTDC.

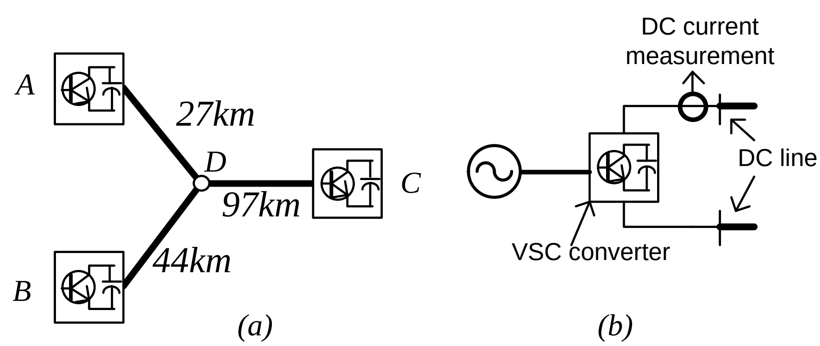

Fig. 5-5 - (a) Test network topology & line length (b) Measured terminal dc line current

The voltage source converters are simulated using detailed models that include IGBT switches and controllers. The ac power system connected to each converter was represented using equivalent sources.

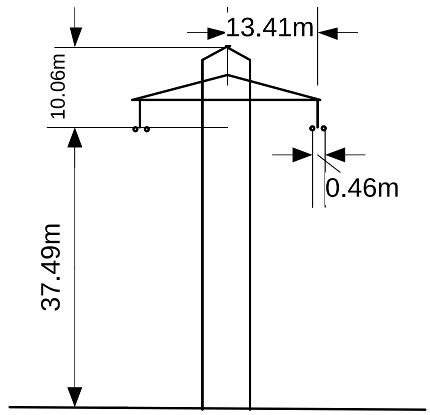

Fig. 5-6 - Tower structure for OH line segments

Even though current through the surge capacitor can be used to identify the surge-arrival time as explained in section 5.5, in this chapter series line currents were used to capture the wave front. It was found that either input would give the surge-arrival time with equal accuracy and in the following study; it was assumed that a transducer with high bandwidth is used to monitor the dc line currents as shown in Fig. 5-5 (b). The actual measurement scheme is not very important, as the main objective of this study is to validate the fault-location algorithm.

Short circuit faults were applied at different locations on the dc network. Simulations were performed in PSCAD/EMTDC with a solution time step of 0.1 μs to ensure all important high frequency components are present in the signals and the signals appear as analog signals to the simulated signal conditioning unit. The input signals (dc line currents) were conditioned before applying to the fault-location algorithm, assuming a 2 MHz sampling rate, 16-bit A/D conversion resolution, and scaling of the current signals to a 0-20 V range before inputting to the A/D converter. This signal conditioning allows testing of the fault-location algorithm under the conditions similar to those existing in a hardware implementation. The sampling frequency of 2 MHz was chosen to achieve a high time precision, which directly imposes a limit on the theoretical accuracy.

5.6.2 Simulation results

Series dc line currents measured at terminals *A*, *B* and *C* are shown in Fig. 5-7(a), when the test network was subjected to a short circuit fault in line *BD*, 10 km away from terminal *B*. The input limits are taken as -50 kA to50 kA. It can be clearly noticed from Fig. 5-7 (a) that the steepness and magnitude of the transients decreases as they propagate to the *A* and *C* terminals. In Fig. 5-7(b) a zoomed view of the same signal is shown. In this case, the fault happened 10 km away from the B terminal. Terminal surge-arrival time differences used to calculate the fault-location are shown as Δt_{AB}, Δt_{BC} and Δt_{BC}.

In Fig. 5-7(c) magnitudes of the CWT coefficients of the input signals at scale 32 are plotted. Sharp changes occur in CWT coefficients at times t_A, t_B and t_C corresponding to terminals *A*, *B* and *C* respectively. They are coincident with the wave front arrival times at respective terminals. Multiple surges observed at terminal *B* are due to reflections, since the fault is close to terminal *B*.

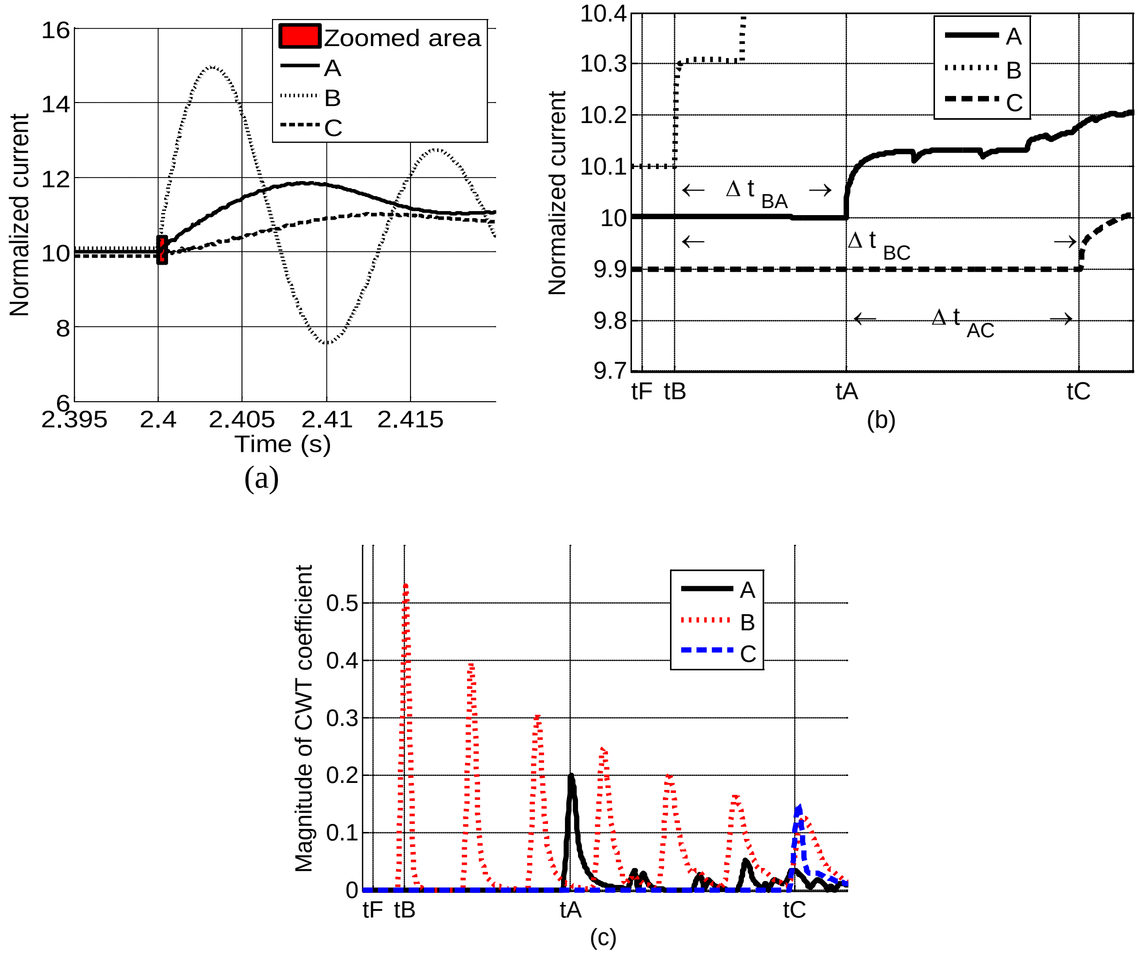

Fig. 5-7 - (a) Monitored dc line current signals conditioned by A/D, (b) Zoomed view of the signals, and (c) the corresponding Scale-32 CWT coefficients for a fault occurred in line BD, 10 km away from B terminal

Table 5-1 - Calculated values of x_{T1}, x_{T2}, R_T and X_F for different fault locations

AFL	XA1	XA2	XB1	XB2	XC1	XC2	RA	RB	RC	XF
0.5km AD	0.49	0.53	70.49	44.03	123.42	96.97	0.94	0.62	0.79	0.51
13km AD	13.02	13.05	57.97	44.03	110.92	96.97	1.00	0.76	0.87	13.03
26km AD	26.07	26.10	44.93	44.03	97.90	96.97	1.00	0.98	0.99	26.08
0.5km BD	70.54	27.08	0.49	0.57	96.93	140.38	0.38	0.87	0.69	0.53
5km BD	66.04	27.08	4.99	5.06	96.93	135.89	0.41	0.99	0.71	5.03
10km BD	61.02	27.00	10.01	10.01	97.00	130.95	0.44	1.00	0.74	10.01
30km BD	41.07	27.08	29.94	30.02	96.93	110.96	0.66	1.00	0.87	29.98
1km CD	26.97	123.15	44.03	140.11	1.05	1.02	0.22	0.31	0.97	1.03
25km CD	26.97	99.15	44.03	116.13	25.00	24.97	0.27	0.38	1.00	24.98
75km CD	26.97	49.05	44.03	66.06	75.00	74.96	0.55	0.67	1.00	74.98
96km CD	27.04	28.05	43.96	45.01	95.95	95.99	0.96	0.98	1.00	95.97
0km AD	-0.07	-0.075	71	44	124	97	0.98	0.62	0.78	-0.07
Star point	27.00	27.00	44.00	44.00	97.00	97.00	1.00	1.00	1.00	

5.6.3 Identification of the faulty line segment using the simulation results

The proposed algorithm was verified with solid line-to-ground faults created at different locations on the three transmission line segments. The faulty segment was identified according to the method shown in Fig. 5-3. Scale 32 CWT coefficients were used for detecting waveform arrival times. The values of x_{T1} and x_{T2} (where T denotes terminals A, B or C) are compared for all three terminals. Table 5-1 summarizes the calculated x_{T1}, x_{T2}, and R_T values for all three terminals A, B and C for different fault locations using the simulation data.

As an example, when the fault is in line *BD*, 10 km away from the *B* terminal, calculated values for R_A, R_B, and R_C are 0.44, 1.00 and 0.74 respectively. The maximum R_T value corresponds to terminal B and therefore the faulty segment can be identified as *BD*. The fault-location is calculated by taking the average value of x_{B1} and x_{B2} as 10.01 km from the terminal *B*.

In Table 5-1, the fault at 0 km on *AD* was a fault in the converter *A*. The algorithm correctly recognized that this is a fault in segment *AD* (value of R_A was the highest) and gave the fault-location as -0.07 km, indicating that the fault is behind the measurement point.

The last row in Table 5-1 shows a fault on the star point. In this case, all x_T values are valid and all R_T values become equal to ‘one’. For a fault closer to the star point such as 26 km *AD*, all R_T values become close to ‘one’. In practice, this can potentially lead to incorrect recognition of the faulted segment due to various sources of inaccuracies due to GPS timing errors, data acquisition time and bit resolutions, noise, etc. However, even in this case, the fault-location indicated by the algorithm would be physically close to the actual fault-location; despite it being on the wrong segment. Such erroneous recognition of the faulted segment can be tolerated in fault-location, which is not intended for providing primary protection for the lines or bus bars.

5.7 Theoretical extension of the algorithm to star-connected network with *n*-number of terminals

The fault-location method proposed in this paper can be extended to a star connected VSC HVDC system with *'n'* number of terminals.

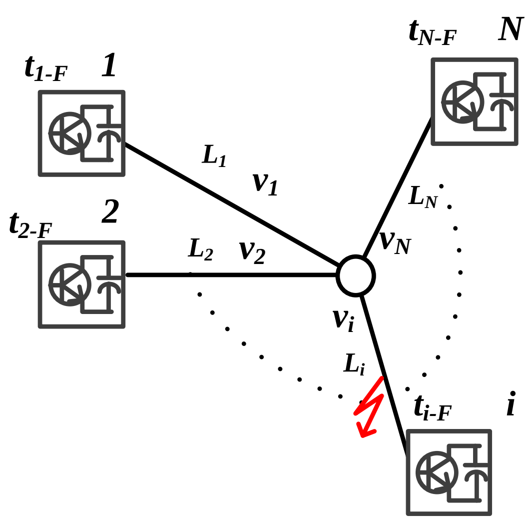

Fig. 5-8 - *N*-terminal VSC HVDC system with all dc lines connect to a common point

Arbitrarily the dc line fault was placed in line section i, x_{i-F} distance away from terminal i as shown in Fig. 5-8. The distances to the fault from each terminal are denoted as, x_{i-F}, x_{2-F} and x_{N-F} which are the distances to the fault from terminals *1*, 2 and *N* respectively. If the fault occurs at time t=0, the time of arrival of the initial travelling-wave at

Terminals *1, 2, … i … N* are given by $t_{i\text{-}F}$, $t_{2\text{-}F}$,… $t_{i\text{-}F}$ … $t_{N\text{-}F}$ respectively. Each of these times can be written in terms of the dc line lengths and $x_{u\text{-}F}$ as follows:

$$t_{1-F} = \left(\frac{L_i - x_{i-F}}{v_i}\right) + \left(\frac{L_1}{v_1}\right) \qquad \text{Eq. 5-30}$$

$$t_{2-F} = \left(\frac{L_i - x_{i-F}}{v_i}\right) + \left(\frac{L_2}{v_2}\right) \qquad \text{Eq. 5-31}$$

$$\vdots$$

$$t_{i-F} = \left(\frac{x_{i-F}}{v_i}\right) \qquad \text{Eq. 5-32}$$

$$\vdots$$

$$t_{N-F} = \left(\frac{L_i - x_{i-F}}{v_i}\right) + \left(\frac{L_N}{v_N}\right) \qquad \text{Eq. 5-33}$$

Where v_1, v_2 … v_i … v_N are the travelling-wave propagation velocities, and L_1, L_2, … L_i … L_N are line lengths of the dc line sections 1, 2, … *i*, …*N* respectively. For a system with *N* terminals, it is possible to obtain *N*-1 expressions for the surge-arrival time difference between the surge given terminal and the terminal connected to the faulted line segment:

$$\Delta t_{1i-F} = t_{1-F} - t_{i-F} = \frac{2 \cdot x_{i-F}}{v_i} - \frac{L_i}{v_i} - \frac{L_1}{v_1} \qquad \text{Eq. 5-34}$$

$$\Delta t_{2i-F} = t_{2-F} - t_{i-F} = \frac{2 \cdot x_{i-F}}{v_i} - \frac{L_i}{v_i} - \frac{L_2}{v_2} \qquad \text{Eq. 5-35}$$

$$\vdots$$

$$\Delta t_{Ni-F} = t_{N-F} - t_{i-F} = \frac{2 \cdot x_{i-F}}{v_i} - \frac{L_i}{v_1} - \frac{L_N}{v_N} \qquad \text{Eq. 5-36}$$

Using the above equations, N-1 expressions can be obtain for the distance to the fault from the terminal i as

$$x_{i-F} = \left(\Delta t_{1i-F} + \frac{L_i}{v_i} + \frac{L_1}{v_1}\right) \times \frac{v_1}{2} \qquad \text{Eq. 5-37}$$

$$x_{i-F} = \left(\Delta t_{2i-F} + \frac{L_i}{v_i} + \frac{L_2}{v_2}\right) \times \frac{v_2}{2} \qquad \text{Eq. 5-38}$$

$$\vdots$$

$$x_{i-F} = \left(\Delta t_{Ni-F} + \frac{L_i}{v_i} + \frac{L_N}{v_N}\right) \times \frac{v_1}{2} \qquad \text{Eq. 5-39}$$

If $\Delta t_{1i\text{-}F}$, $\Delta t_{2i\text{-}F}$ … $\Delta t_{Ni\text{-}F}$ can be obtained through measurements then the fault can be located with known propagation velocities and dc line segment lengths. N sets of similar expressions can be derived by changing the faulted segment from 1 to N. Therefore for an N line segments case, there will be $N.(N\text{-}1)$ different equations.

Since the faulted line segment is unknown initially, possibility of the fault in any of the N line segments is considered and for each case, (N-1) possible values for the distance to the fault from the terminal directly connected to the considered line segment are computed. If the fault is actually on the i^{th} line segment, then all (N-1) estimated fault distances, ($x_{i\text{-}F}$ values) should be the same (in practice they are not exactly the same, but lie very close to each other). Furthermore, estimated fault locations using any other equation set will not be consistent. Hence the faulted line segment can be identified without any ambiguity. In addition, the fault-location can be taken as the average of the (N-1) estimated values for the identified faulted segment. The generalized method is shown in Fig. 5-9 which is derived from the method explained in section 5.3.

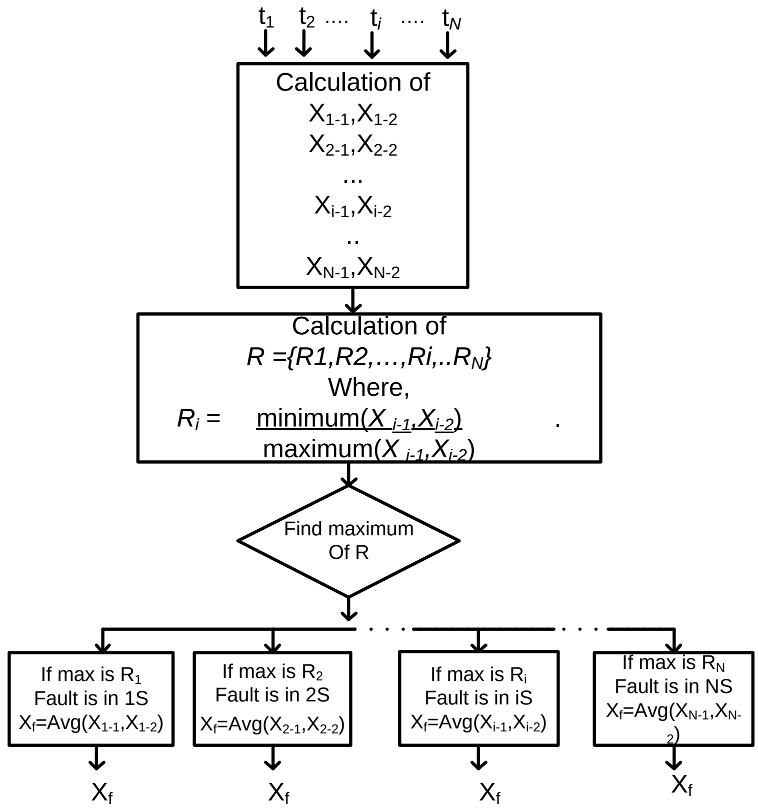

Fig. 5-9 - Faulty segment identification and fault calculation method for network with '*N*' terminals

Generally, a simple star connected topology is not considered reliable, since any fault in the centre node would force all converters out of service. The preferred topology is a star connected network with a switching ring at the center. Since the fault-location calculation is based on the initial travelling-wave arrival times, the proposed method would not be affected by the possible reflections and refractions at the ring. Typically, the length of a switching ring would be much shorter compared to the line distances, therefore a system with a switching ring can be effectively treated as a star connected network as far as the fault-location is concerned.

5.8 Concluding remarks

An algorithm to locate faults on star-connected multi-terminal VSC HVDC transmission lines using only the terminal measurements was proposed. The proposed algorithm that uses the travelling-wave fault-location principle has the ability to correctly identify the faulted line segment using only the measurements at the converter ends.

Application of the proposed fault-location method to a 3-terminal VSC HVDC system consisting of overhead line segments was demonstrated through simulations. The simulation results verified the correct operation of the fault-location algorithm. According to the simulation results, it is possible to achieve fault-location accuracy of ± 300 m for the test system considered using dc line currents.

The proposed method eliminates the need for the installation of repeater stations at the junction of the multi-terminal HVDC network. Although derivations and simulations were carried out considering a three-terminal dc network, the concept can be theoretically expanded to an N terminal network, as shown in Section 5.7.

Chapter 6

Implementation and field validation of a travelling-wave arrival-time measurement scheme

6.1 Introduction

As pointed out in the earlier chapters, the main factor that affects the accuracy of fault-location is the accuracy of measuring the fault generated travelling-wave arrival times. It is important to ensure that instrumentation employed for these measurements perform properly under substation environments rich in electromagnetic noise. A number of commercial dc line fault-location systems that use the travelling-wave principle have been developed and some of the details have been published in literature (E.g. [20], [21] and [47]). However, none of them has clearly explained the method of capturing the wave-fronts arrival times. In this chapter, a method for detecting the arrival of fault transients using the surge capacitor currents is proposed. In this scheme a Rogowski coil functions as the sensor, and its output voltage is continuously monitored using a data acquisition (DAQ) system. A GPS clock signal is provided to the DAQ system to time synchronize the measurements.

A prototype of the proposed travelling-wave arrival time measurement system was implemented and field-tested at the Nelson River HVDC Scheme in Manitoba, Canada [66].The practical problems such as bandwidth capability, noise level and the output voltage magnitudes involved in the application of a Rogowski coil as the transducer are solved with a successful field implementation. In the following sections, the important steps in the development of the experimental setup are described. Furthermore, the field data gathered during the 23rd of July 2012 to the 4th of September 2012 are analysed and compared with the existing fault locator results. However, the main objective of the experimental setup is to validate the usage of the transducer and the data acquisition system. The experiments were not designed to compare with the existing fault locator even though some results of the existing setup are used to validate the experimental unit.

In Chapters 2 and 3, the Continuous Wavelet Transform coefficient of the surge capacitor current measurements was used to detect the travelling-wave arrival times. However, during the field tests, it was found that the Rogowski coil sensor output voltage could be directly used for detecting the travelling-wave arrival times with high accuracy. Comparison of the results obtained with direct measurements to the results obtained with the CWT based method discussed in Chapter 3 showed that both approaches result in a similar level of accuracy.

6.2 Arrangement of the surge-arrival time measurement system

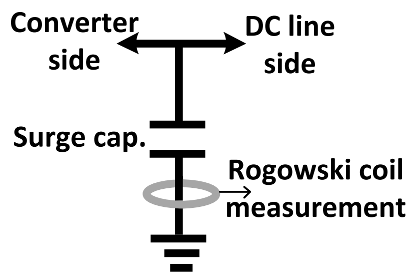

Fig. 6-1 - Wave-front detection system

The simplified arrangement of the wave-front detection system is shown Fig. 6-1. The surge capacitor is typically used in conventional HVDC converter stations to protect the converter station equipment from surges travelling along the dc line. Additionally, the current going through the surge capacitor can be used to capture the wave-front and this method has been used before in [20], [21] and [47] to acquire the wave-fronts. In this arrangement, the transducer is located on the ground potential and it is not directly connected to the HVDC system. Therefore, the measurement system requires lower insulation protection and has negligible interaction with the HVDC system. Installation of the measuring system does not require a complete shutdown of the system and it is very easy to mount around the ground wire because the used transducer is a clamp on type flexible Rogowski coil.

6.3 Rogowski coil

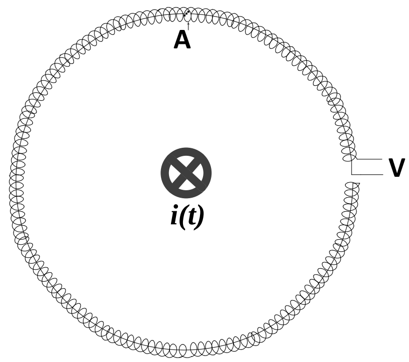

Fig. 6-2 - Flexible Rogowski coil

Rogowski coils have been proposed for ac network fault-location applications ([48]-[50]). However, the application of Rogowski coils in dc line fault-location systems is not clearly mentioned in any of the published literature. Thus, the application of Rogowski coils for surge-arrival time detection in HVDC substation environments with high frequency noise is explored in this chapter.

The arrangement of a Rogowski coil is shown in Fig. 6-2. The sensor is made from a helical coil with the lead from one end returning through the centre of the coil to the other end. Voltage (V_0) induced in the coil is proportional to the rate of change of the current [46] in the conductor (I) which runs through the Rogowski coil.

$$Vo = \frac{-AN\mu_0}{l} \times \frac{dI}{dt} \qquad \text{Eq. 6-1}$$

Where N is the number of helical turns, l is the length of the winding, A is the area of one loop and μ_0 is the permeability of free space.

A Rogowski coil is mainly used for measuring ac currents or current transients. Some applications of Rogowski coils as mentioned in [51], [52], [53] and [54] include power quality monitoring, measurements in lightning test equipment, relay protection, switchgear, and generators/motors operations. As the output voltage is proportional to the rate of change of the primary current, in order to obtain a signal proportional to the current, the output voltage needs to be integrated. Thus, in current measurement applications, Rogowski coil sensors come with an associated integrator. However, there is no need for measuring the actual current in the primary wire in the fault-location applications. Since identification of the travelling-wave arrival time is the main purpose of the transducer, this can be achieved without the integrator. The Rogowski coil terminal voltage is approximately proportional to the second derivative of the dc line terminal voltage. Hence, the Rogowski coil voltage produces a very sharp transient signal when a voltage wave arrives at the terminal and it facilitates easy detection of wave-front arrival.

Advantages of Rogowski coils in current measurements are clearly listed in [53] and the most important advantages relevant to transient current detection are:

1) they have a very wide bandwidth, extending from typically 0.1 Hz to about 1 GHz,
2) they have excellent transient response capability,
3) they have the capability of measuring large currents without saturating because of its nonmagnetic core,
4) they are easy to use due to their flexibility and light weight,
5) they have a lower price compared to conventional high bandwidth hall effect sensors and optical CTs, and
6) they are very safe because there is no direct electrical connection to the main circuit.

Due to these reasons, it is ideal for fault-location application in HVDC systems.

6.4 Layout of the prototype measurement unit

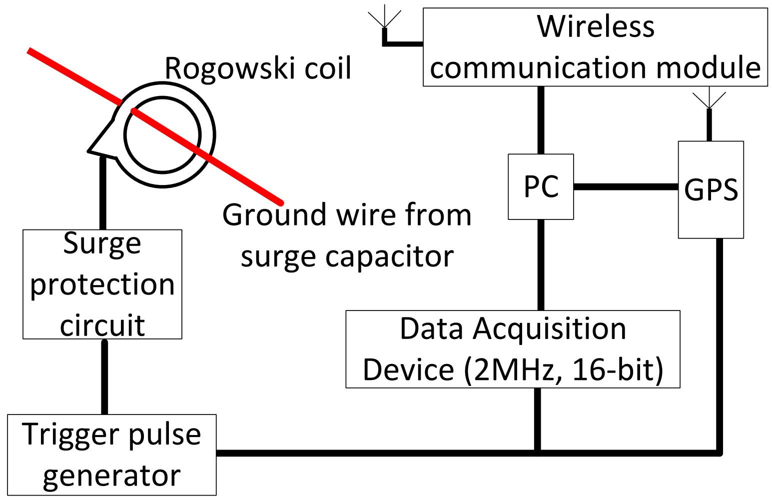

Fig. 6-3 - Layout of the experimental setup at one converter station

Fig. 6-3 shows the simplified block diagram of the proposed fault-location system. When a transient current flows through the grounding wire of the surge capacitor, a voltage is induced at the terminals of the Rogowski coil. This voltage signal then goes through the surge protection circuit, which will condition the signal and protect the rest of the electronics from over voltages. The trigger-pulse generator consists of fast acting op-amps and fast acting TTL pulse generating electronics. When the input Rogowski voltage rises above a predefined threshold due to the arrival of a surge, it generates trigger pulses to both the data acquisition system and the GPS time tagging system at the same time. This wave-front initiated pulse triggers the data acquisition system, which will capture the voltage signal at 2 MHz sampling frequency and 16-bit resolution. Also when triggered, the GPS module time stamps the Rogowski voltage sample acquired at the triggering point with ±100 ns time accuracy. The captured waveform and the time tag data is saved to the computer. Wireless communication modules are used to access data remotely.

6.4.1 Specifications of the Rogowski coil

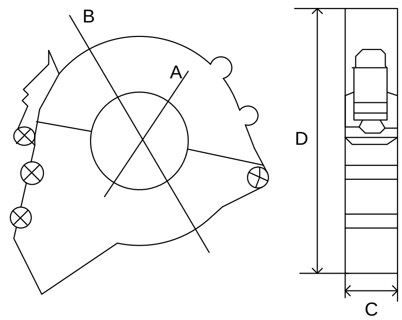

Model No	A(min)	B(max)	C(max)	D(max)
TSR 35	35.0 mm	83.0 mm	20.9 mm	99.5 mm

Model No	Rated Current	Self Inductance	Mutual Inductance	DC Resistance
TSR 35	1000A	0.54 mH	0.40 µH	49 Ω

Fig. 6-4 - Technical details of the selected Rogowski coil (Redrawn from [56])

A clamped-on Rogowski coil is selected since it is easier to install with minimum interference to the existing wirings. *Taehwatrans* part number TSR35L [56] is selected after considering the trade-off between the availability and high mutual inductance. The specifications are shown in Fig. 6-4. This device does not contain an integrator circuit since there is no need to measure the actual current in the primary wire in the proposed fault-location method. Identification of the travelling-wave arrival time is the main purpose of the transducer. To improve the accuracy, it is important to see a sharper change and measurable voltage at the Rogowski coil terminals. Generally, higher mutual inductance would produce higher voltage output at the terminal and smaller self-inductance would provide sharper rise time.

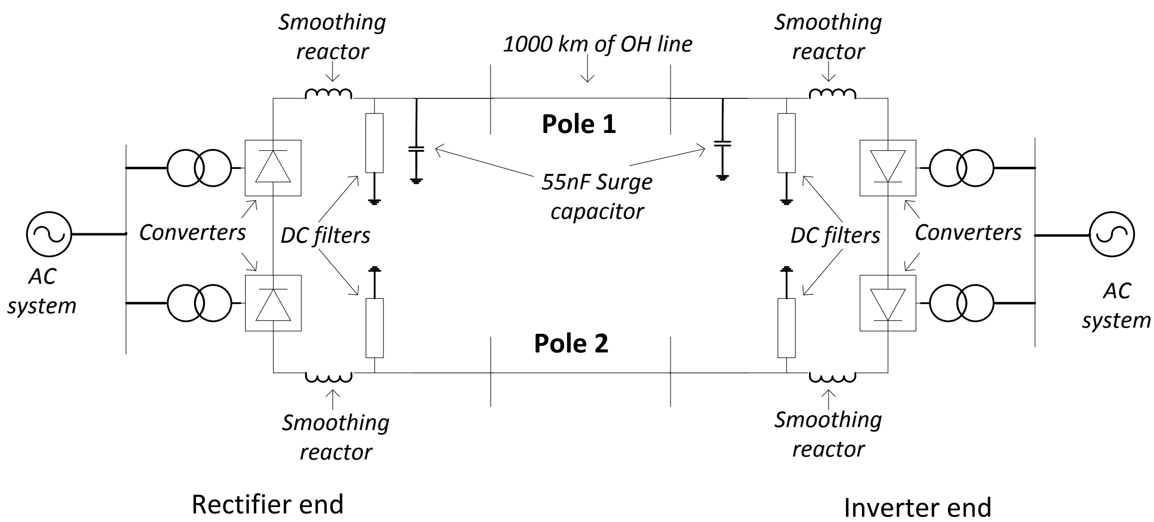

Fig. 6-5 - Test network modeled in PSCAD/EMTDC

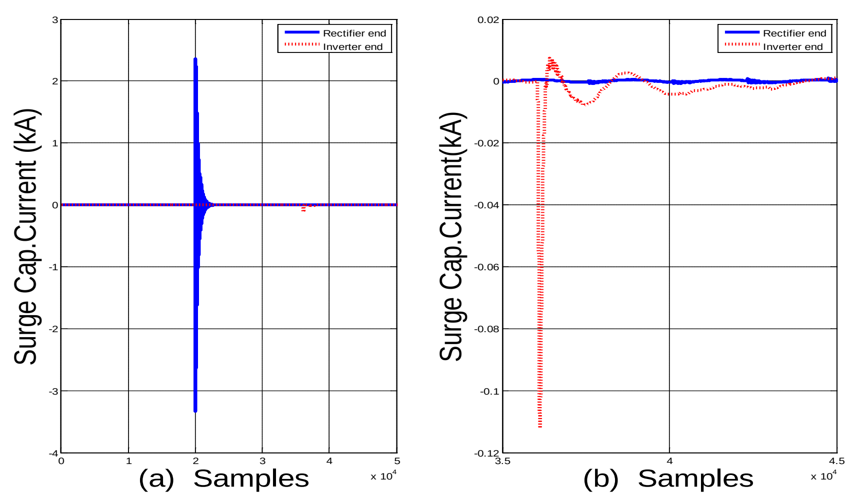

Fig. 6-6 - Surge capacitor current after applying a fault 1 km from rectifier (a) complete view of the two end surge capacitor currents (b) zoomed in view to show the inverter end surge capacitor current

Before the selection of model TSR35L, a comparison of the response of different Rogowski coil models listed in [56] was carried out using simulations. The relevant parameters (mutual and self-inductances) of the different Rogowski coils are listed in Table 6-1. The Rogowski coils were modelled in MATLAB and a HVDC system with a 1000 km long overhead line was modelled in PSCAD/EMTDC. The test network used for simulation is shown in Fig. 6-5 and it is a modified version of the Cigre benchmark test network. Fig. 6-6 shows the monitored surge capacitor current after applying a solid line to ground fault 1 km away from the inverter side. The transient currents through the surge capacitor current closer to the fault are larger and the currents observed at the other end are comparatively smaller. The smaller current waveform measured at the far end (somewhat close to the worst case current) is applied to the Rogowski coil models and the output voltages are shown in Fig. 6-7.

According to Fig. 6-7(b), the TFR Rogowski coil gives sharper change and the largest peak among the compared models and it also has highest mutual inductance as listed in Table 6-1. Therefore, it is the ideal device to use in the experimental fault locator. The second best coil is TSR 145 as it gives the second best ‘peak’ and the second best ‘rise time’. However these Rogowski coils were not available to order from the manufacturer at the time of development. According to the availability, the third best Rogowski coil (TSR 35) was selected.

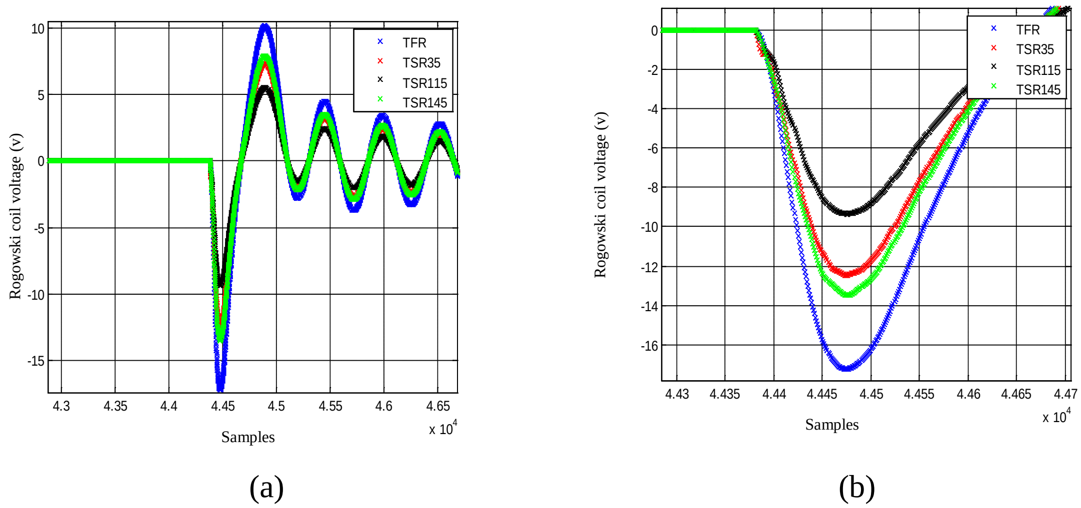

Fig. 6-7 - Comparison of Rogowski coil output voltages (a) Complete view (b) Zoomed in view to clearly show the first slope

Table 6-1 - Self and mutual inductance values of different Rogowski coils

Part No	Mutual Inductance	Self Inductance
TSR 35	0.40 µH	0.54 mH
TSR 115	0.30 µH	1.20 mH
TSR 145	0.43 µH	1.70 mH
TFR 1	0.55 µH	3.50 mH

The Rogowski coil installed on the surge capacitor grounding wire at the Dorsey converter station is shown in Fig. 6-8.

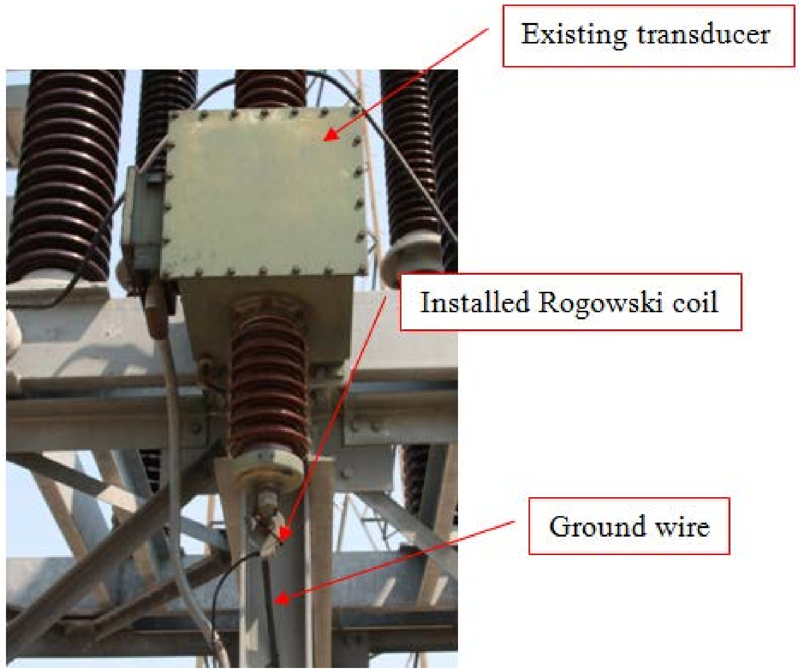

Fig. 6-8 - Installed Rogowski coil at Dorsey converter station

6.4.2 Surge protection unit and trigger pulse generating circuit

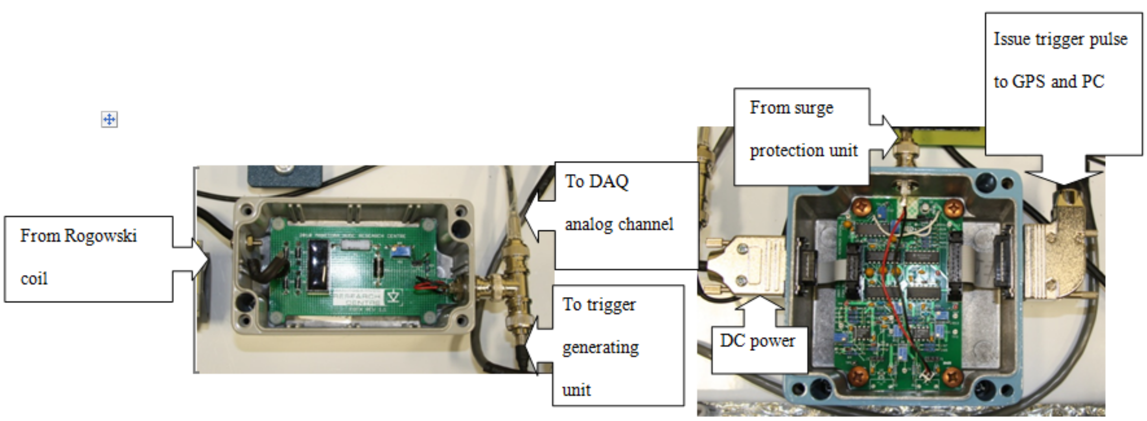

(a) - Surge protection unit

(b) - Trigger pulse generating unit

Fig. 6-9 – (a) Surge-protection and (b) trigger-pulse generating circuits as appear in the experimental unit

Fig. 6-9 *(a)* and Fig. 6-9 *(b)* show the surge protection unit and the trigger pulse generating unit installed in the experimental fault locator. As shown in Fig. 6-9 (a) the input to the surge protection unit is the Rogowski coil voltage; and its output is connected to the analog input channel of the data acquisition (DAQ) hardware and the trigger generating unit.

Main purposes of the surge protection unit are:

(1) Protect DAQ hardware and other circuits from over voltages - Protection is achieved by two high speed Zener diodes at two voltage steps.

(2) Rectify the voltage signal arriving from the Rogowski coil - Using full diode bridge. Rectification is required to ensure the fault locator operation for faults occurring at both poles of Nelson River HVDC system.

As shown in Fig. 6-9 (b) the input to the trigger pulse generating unit is the output of the surge protection unit, which is connected to both the DAQ trigger port and the trigger port of the GPS unit.

Main purposes of the trigger generating unit are:

(1) Generate trigger pulse to the GPS unit and the DAQ hardware at the same time when the Rogowski coil voltage is larger than a threshold. This will ensure the time tag given from the GPS unit perfectly matches with the trigger point of the DAQ unit.

(2) Hold the trigger pulse for 40 ms to make the system immune to the miss-triggers.

6.4.3 Data acquisition hardware

Fig. 6-10 - Multifunction Data Acquisition hardware NI USB-6361 from National Instruments

National Instrument USB-6361 data acquisition hardware [57] is used in the experimental unit. This hardware allows 2 MS/s sampling rate with 16-bit resolution when using a single analog channel. It also supports digital edge triggering and hence analog data is captured when the trigger pulse generating unit issues a 5 V step pulse. Pre-trigger samples can also be captured with this DAQ.

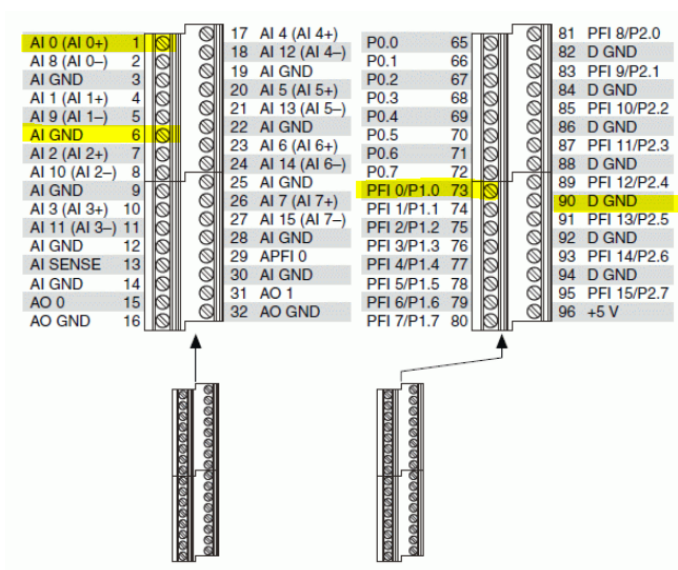

Fig. 6-11 - Pin layout of NI USB 6361

As shown in Fig. 6-11, pin no 1 and 6 are connected to the Surge Protection Unit output and pin no. 73 and 90 are connected to the Trigger pulse generating unit output.

6.4.4 Specifications: GPS (Global Positioning System)

Fig. 6-12 - GPS unit: EVK-6T-0 u-blox 6 Evaluation Kit with Precision Timing

U-blox evaluation kit with precision timing (EVK-6T-0) is selected to time stamp the Rogowski coil voltage measurement. As shown in Fig. 6-12, it has an active antenna unit which is mounted outside the cubical in order to make sure enough satellite signals are picked up at the installation site. This GPS unit is powered by a 5 V supply connected to a USB (Universal Serial Bus) port as can be seen in Fig. 6-13 front panel. The serial port shown in Fig. 6-13 rear panel is used to communicate with the PC and to send the trigger signal to get the time stamp. The details of the pin assignment for this serial port are given in Table 6-2.

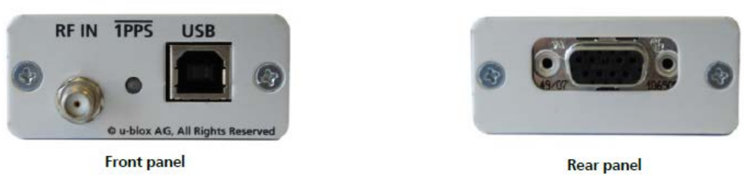

Fig. 6-13 - Front and real panels of the GPS unit

Communication with the GPS is based on UBX protocol described in [58]. First the GPS unit's software (u-centre) [59] needs to be installed in the Computer. Then the GPS unit is initialized: the changes to the default values are described in Appendix B.

Table 6-2 - Serial communication pin assignment

Pin No	Assignment
1	GPS Time Pulse Output
2	GPS Transmit Data
3	GPS Receive Data
4	GPS External Trigger
5	Ground
6	GPS Time Pulse Output 2
7-9	Not Used

6.4.5 Specifications: Personal computer and the wireless communication module

Wireless Communication module

Fig. 6-14 - IPn3G - 3G Cellular Ethernet/Serial/USB Gateway

A 3G cellular Ethernet gateway (Cellular Radio IPn3G *-3G Cellular Ethernet/Serial/USB Gateway* from *Microhard Corp*) is used to provide internet access to the computer deployed in the field which is shown in Fig. 6-14. The details of this device can be found in [63] and a separate *Yagi* type antenna is mounted in order to capture signals from the weak cellular network at the station yard. Subscriber Identification Module (SIM) with a data plan was purchased from Manitoba Telecommunication Services (MTS). The SIM is inserted to the Cellular gateway and a PC is connected to the Cellular gateway via an Ethernet port.

Computer

Fig. 6-15 - ARK-3360F Embedded Box PC from AdvanTech

Embedded box PC model ARK-3360F shown in Fig. 6-15 from Advantech [64] is used as the Personal Computer in the experimental unit and Windows 7 Professional 64 bit operating system was installed. Serial port (COM 6) is used to communicate with the GPS unit and one USB port is used to supply power to the GPS unit. The Ethernet port is connected to the wireless gateway. Another USB port is connected to the DAQ hardware. The GPS unit's software *u-centre* version 7.02, *National Instrument Measurement and Automation Explorer* version 4.7 with *NI-DAQmx 9.1,* and the software developed to capture the Rogowski coil waveforms are installed in the computer.

6.4.6 Software for capturing waveforms

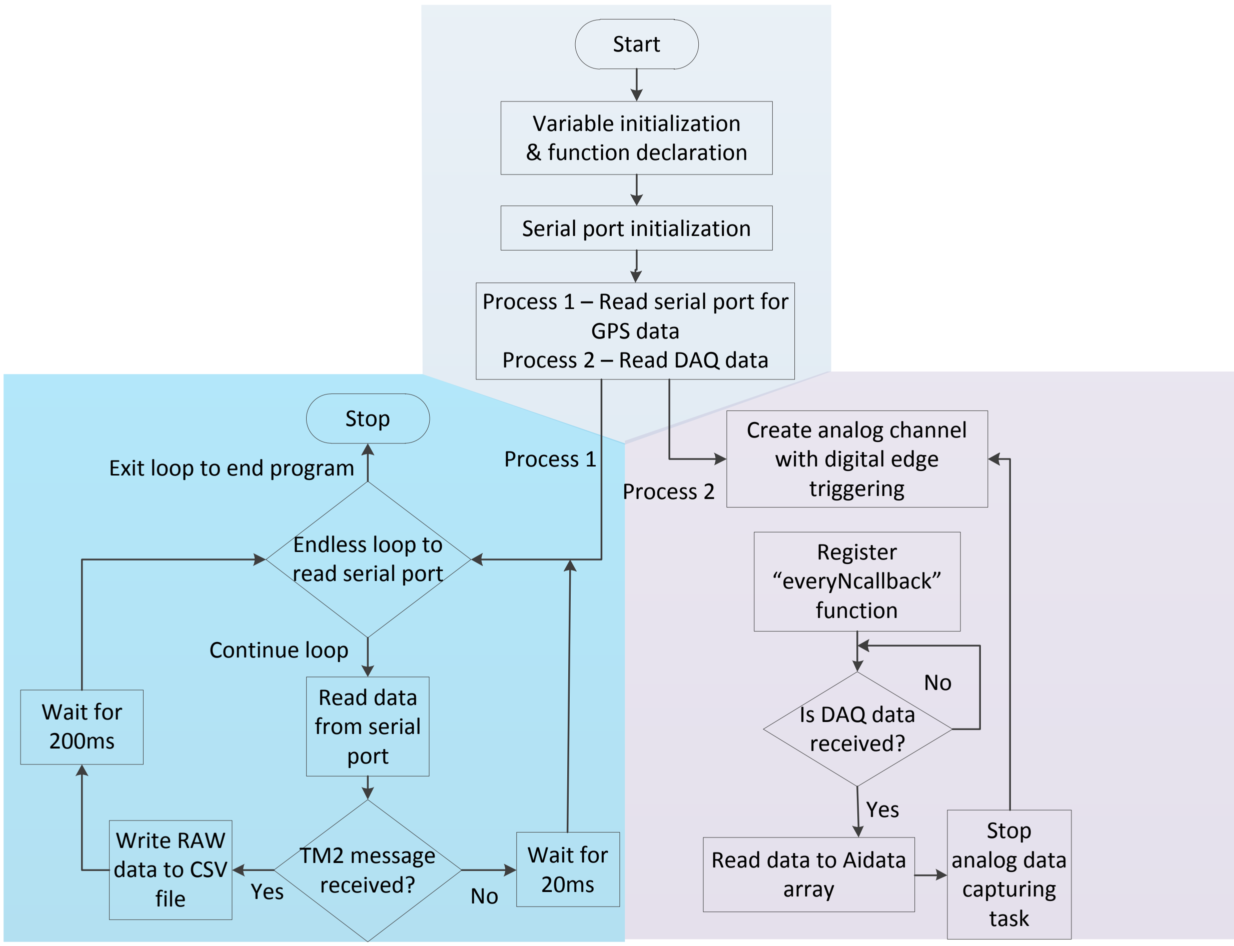

Fig. 6-16 - Simplified flow diagram of the developed software

Data capturing software was written in Microsoft Visual C and C++. A simplified flow diagram of the software is shown in Fig. 6-16. The program will read 10000 samples from the DAQ when the data is available at the DAQ buffer and the first 3000 samples are pre-trigger samples. This corresponds to a 5 ms time period at 2 MHz sampling rate. This is more than enough to capture the first travelling-wave surges for any fault that happened within the 895 km long OH line.

The data is written to a Comma Separated File (CSV) with the name format of "*Data*_Station Name_*Week No_Second No in msec_nanosec*.csv". At Station Name either Dorsey or Radisson (two converter stations in the Nelson River HVDC scheme) is shown according to the unit. Time format is based on GPS time standard as described above. The CSV file contains five columns: No, AI data, Week No, ms, and ns. The first column shows the sample number in ascending order of time. Pre-trigger data are contained up to the 3000th sample. At the 3000th sample, the trigger pulse is received from the trigger generating unit. The AI data column contains measured values by the DAQ in volt. Time tags read from the GPS is shown in the next three columns (Week No, ms and ns) at the 3000th sample point.

6.4.7 Rogowski coil placement at the converter station

Two prototype wave front arrival time measurement units were constructed with the support of Manitoba HVDC Research Centre [65]. They were installed at the Nelson River HVDC Transmission System operated by Manitoba Hydro. This HVDC transmission system transfers electric power generated by several hydroelectric power stations along the Nelson River in Northern Manitoba across the wilderness to the populated areas in the south of Manitoba [66] as shown in Fig. 6-17. The Nelson River HVDC scheme consist of two bi-poles and there are two parallel dc circuits sharing the same right of way, as indicated in Fig. 6-17 and Fig. 6-18.

Experimental fault locators were installed at the Radisson (Rectifier) and Dorsey (Inverter) converter stations on two ends of the negative conductor of Bipole-1. The length of the dc line between the converter stations is 895 km. In the Nelson River HVDC system, the presence of a surge capacitor is explained in [55] and its existing fault locator is installed on the ground side of the surge capacitor.

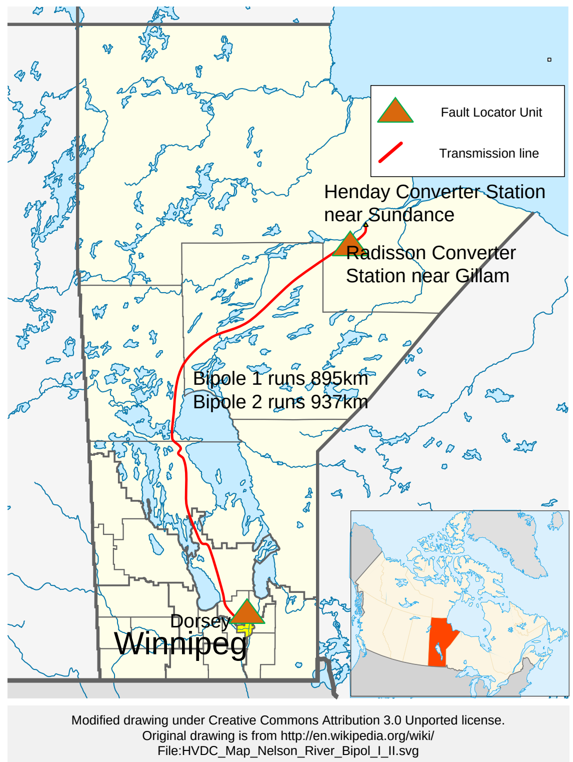

Fig. 6-17 - Map of the Nelson River HVDC Transmission System with installed locations of the fault locators

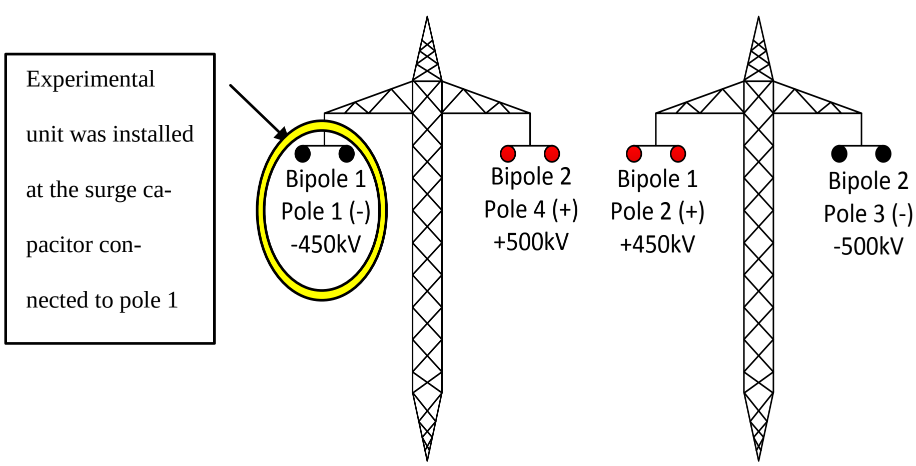

Fig. 6-18 - Placement of the experimental unit in Nelson River HVDC line (Under normal operation of Nelson River system)

6.5 Summary of the recorded events

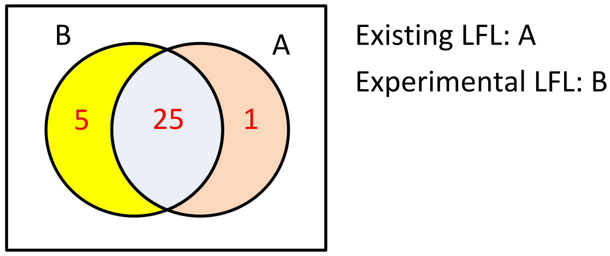

Fig. 6-19 - Venn diagram view of recorded events

The distribution of the number of events recorded in the experimental unit and the operational fault locator between the 23rd of July and the 4th of September in 2012 are shown in Fig. 6-19. During this time period, only temporary dc line faults were recorded. Thus the actual location of any of the events could not be verified by physical observation. However, locations of 25 events were verified with the existing operational fault locator. A histogram of the distance to fault-location from Dorsey station of the 25 verified events are shown in Fig. 6-20. About 52% of the events occurred between 550 km to 700 km from Dorsey station. No events were recorded within 400 km from Dorsey station. Similarly no events were recorded beyond 825 km from Dorsey station.

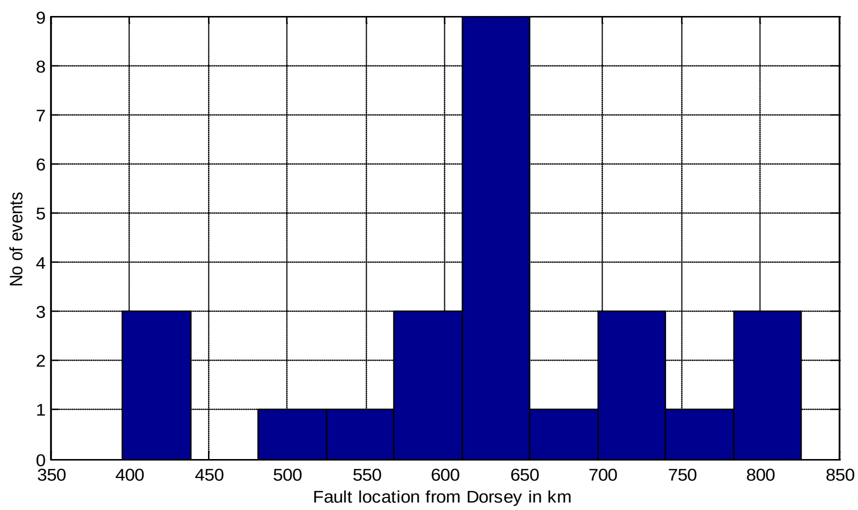

Fig. 6-20 - Histogram view of the fault-location from Dorsey in Kilometers

The waveforms captured during event 1 are shown in Fig. 6-21. This temporary fault happened about 825 km from Dorsey station and the event was verified with the operational fault-location unit. It is evident from Fig. 6-21 that this event generated Rogowski coil voltages which are easily measurable from the DAQ units at both ends, even though the fault was close to the Radisson end of the line. Table 6-3 compares the fault locations determined by the prototype unit and the operational unit. The mismatch in the measured surge-arrival time difference is 646 ns. The difference in the estimated fault-location is 0.09 km for this particular event.

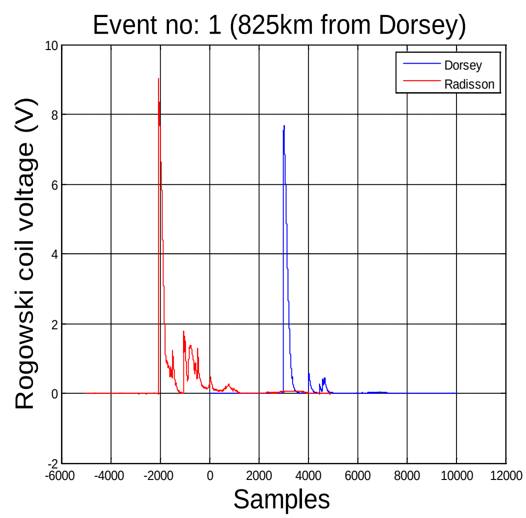

Fig. 6-21 - Captured waveform from the experimental unit (First recorded event)

Table 6-3 - Comparison of fault-location & surge-arrival time difference of event 1

Fault-location in km from Dorsey		***Wave-front arrival time difference between two units (nsec)***
Operational unit	*Experimental unit*	
826.25	826.16	646.0057

Voltages of all the captured waveforms from the experimental unit are shown on a colour map in Fig. 6-22. In the colour maps, the horizontal axis represents the sample numbers and the sampling process was done at a 2 MHz sampling rate. The vertical axis shows the event number in ascending order of time and the colour scale represents the Rogowski coil voltage in volts.

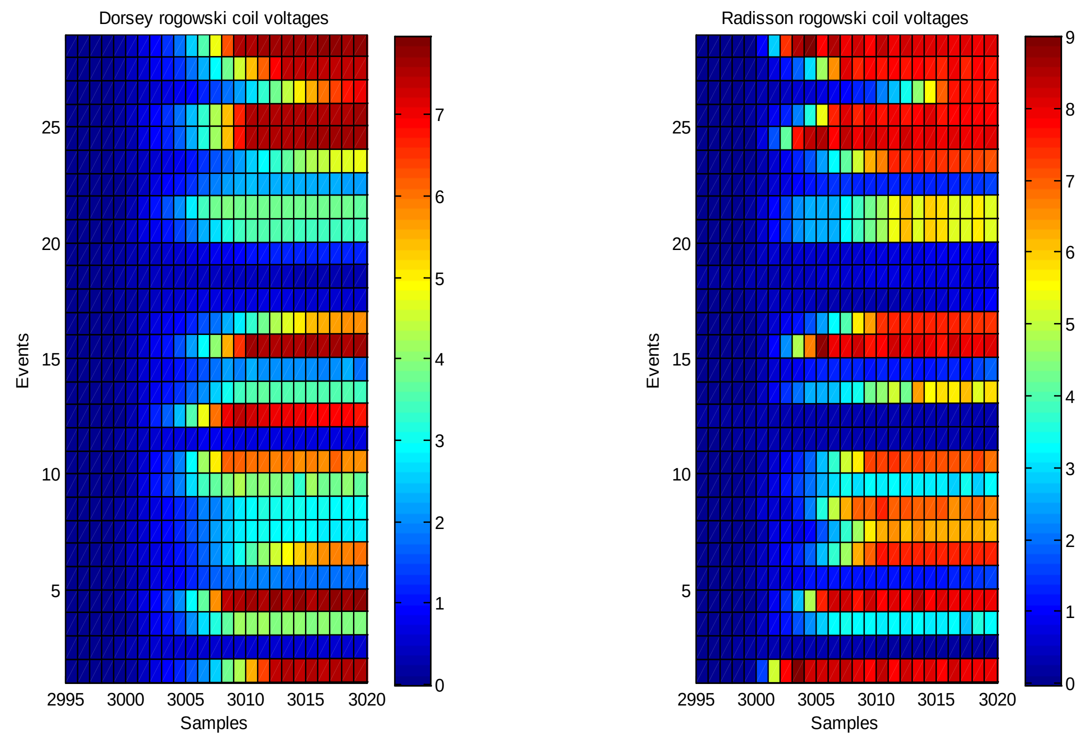

Fig. 6-22 - Colour map view of captured Rogowski coil voltages in volts

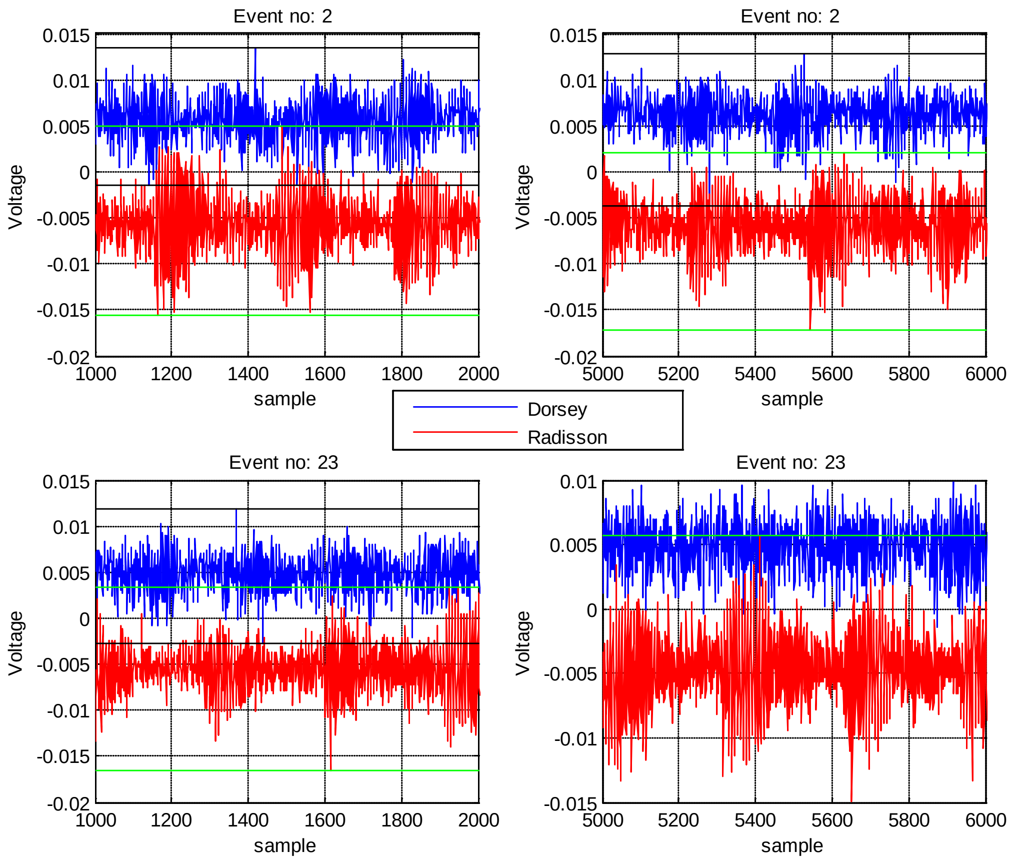

Fig. 6-23 - Captured Rogowski coil pre fault voltages for selected events

Noise level present in the system can be observed with pre-fault voltages and the noise level can be varied due to many factors like the operating conditions, weather conditions and external communication interferences etc. However, for the Nelson River System during the observed periods, the noise levels were within ±20 mV range as can be seen in Fig. 6-23. Noise level is smaller compared to the voltage peak which appeared at the wave-front arrival point. According to Fig. 6-22, rise time of the signal is within 10 samples (At 2 MHz rate this value is equal to 5 μs time period) for most of the cases. Therefore the proposed Rogowski coil transducer is suitable in the Nelson River HVDC dc line fault-location application.

6.5.1 Lightning strike caused event

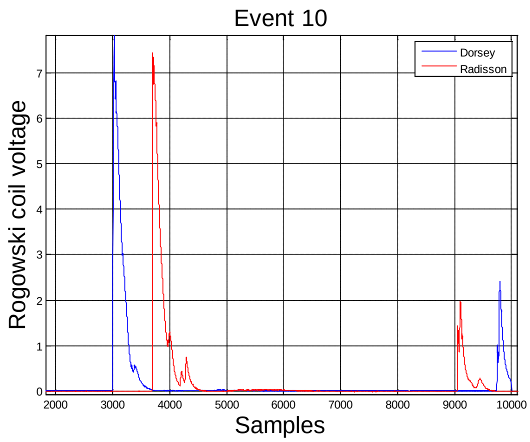

(a) - Rogowski coil voltages at two stations with synchronized samples

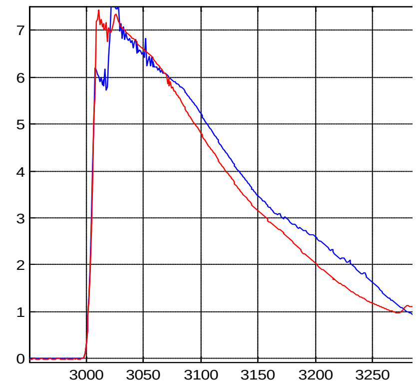

(b) - First peak of the Rogowski coil voltages at two stations with unsynchronized samples

Fig. 6-24 - Captured voltages for event 10

Table 6-4 - Comparison of fault-location & surge-arrival time difference of event 10

Fault-location in km from Radisson		***Wave-front arrival time difference between two units (nsec)***
Operational unit	*Experimental unit*	
499.025	499.009	108

Captured waveforms of event 10 are shown in Fig. 6-24. The event was verified with the operational unit. The comparison details are shown in Table 6-4. The difference between the surge-arrival time differences of the operational unit and the experimental unit is 108 ns. Therefore the fault is verified. It happened about 499 km from Radisson station. A lightning strike was located around that time at about 497.3 km from Radisson. The location of the lightning strike as indicated by the lightning locator is shown in Fig. 6-25. The red circle shown on the map is the 90% confidence limit for the lightning location according to Manitoba Hydro's lightning locator. The error in lightning fault-location is approximately ±0.87 km.

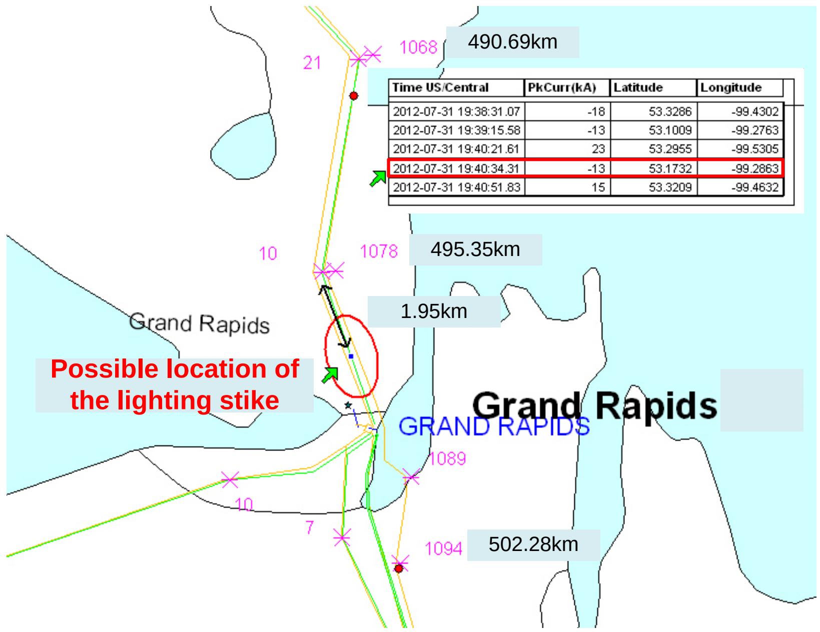

Fig. 6-25 - Fault-location on the map obtained with Manitoba Hydro's lightning strike locator

Therefore this event is an example case of a lightning strike caused disturbance. As can be seen in Fig. 6-24 (b), the captured waveform contains a sharp edge rising to about 7 V, making it easier to identify the surge-arrival time with less error.

6.5.2 Identification of a disturbance occurred in pole 3

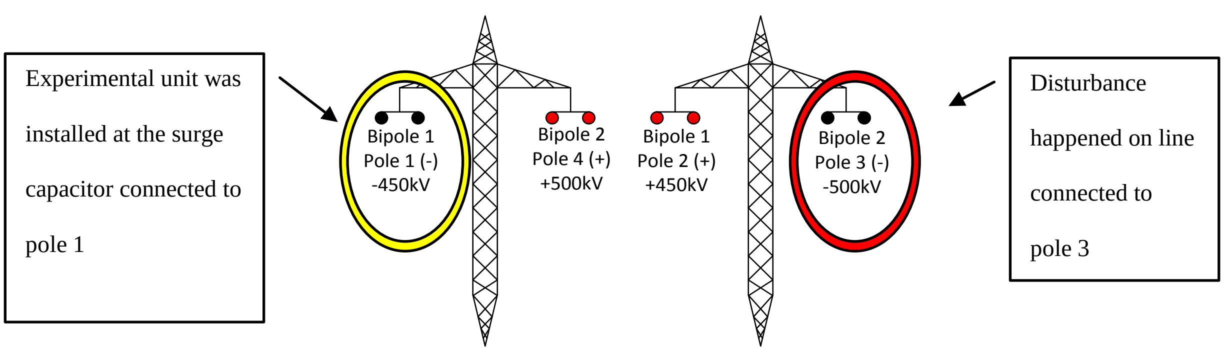

Fig. 6-26 - Nelson River HVDC system dc tower operation under normal condition

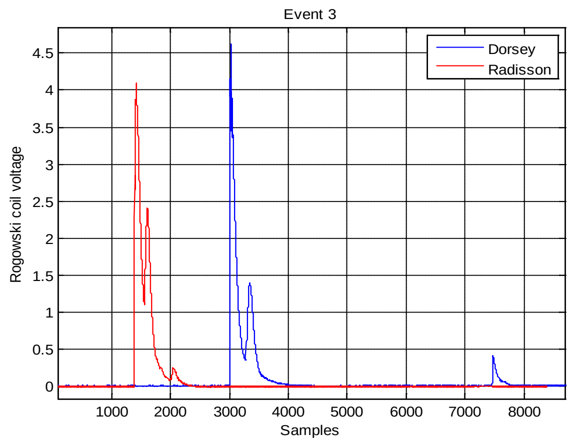

Fig. 6-27 - Event 3 occurred on pole 3

During the normal operation pole 3 is located towards the right side edge of the right of way and pole 1 is located at the left side edge of the right of the way as shown in Fig. 6-26. The experimental unit is installed on pole 1. Due to mutual coupling even a fault occurring in pole 3 can induce transient voltages on pole 1 and these transients create a voltage at the Rogowski coil terminal which can be observed in the experimental unit. An example event is shown in Fig. 6-27. As can be seen the peak voltages are relatively lower compared to the disturbances that occurred on pole 1. However this event is still clearly recognizable. It was verified as a pole 3 disturbance with Sequence Event Recorder (SER) data and also with the operational unit data.

6.6 Simulation study

The simulation study presented in this section is carried out with two objectives. The first is to compare the wave-front arrival times directly obtained from the Rogowski coil measurements with those obtained using the wavelet coefficients of the surge capacitor current. The practical measurements showed that surge-arrival time can be measured with good accuracy even from the direct comparison of the Rogowski coil output with a threshold. If the accuracy of the wave-front arrival times directly obtained using the Rogowski coil is comparable with those obtained through wavelet coefficients, the use of direct measurements is preferable.

The second objective of the simulation study is to validate the application of Rogowski coils based measurement scheme for extra-long dc transmission lines. Thus the test HVDC network used for simulations contains a 2400 km long OH line, which is much longer than the 895 km line of the Nelson River System. However, the simulation model of the measurement scheme in the fault locator is similar to the experimental setup installed at the Nelson River HVDC system.

6.6.1 Test network

A conventional two-terminal HVDC system with a 2400 km long overhead transmission line was used in simulation studies. The schematic diagram of the test network is shown in Fig. 6-28. All the simulations were carried out with PSCAD/EMTDC and the wavelet transform calculations and Rogowski coil modeling were performed in MATLAB. The surge capacitors used in the simulation model are of 0.055 μF capacity, which is smaller than the 0.55 μF used in the Nelson River HVDC scheme. This combination of small surge capacitors and the extra-long transmission line represents an extremely difficult case in terms of the detection of surges. The surge capacitor currents were monitored for dc line short circuit faults applied at different locations. Simulations were performed in PSCAD/EMTDC with a solution time step of 0.1 μs to ensure all high frequency components are present in the signals. This arrangement of the fault locator is similar to the experimental setup installed at the Nelson River system.

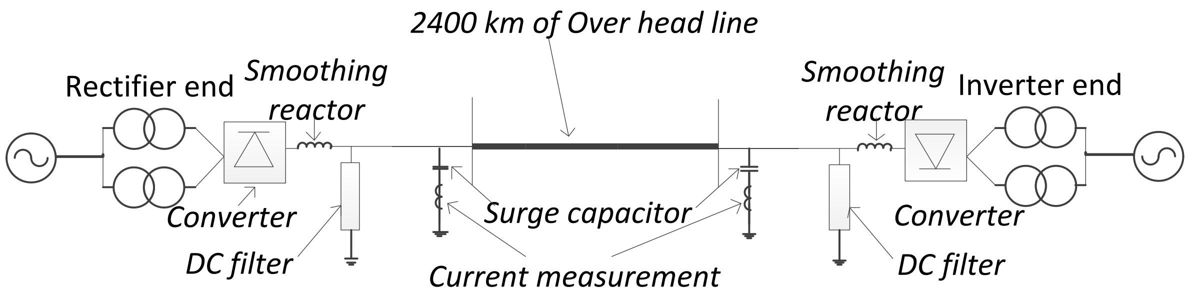

Fig. 6-28 - Simulation model

6.6.2 Rogowski coil simulation model

The Electro Magnetic Transient (EMT) type Rogowski coil model proposed in [28] is used in this study. The equivalent circuit of the simulation model is shown in Fig. 6-29. The induced voltage is proportional to the rate of change of primary conductor current times the mutual inductance of the Rogowski coil. The load impedance is the impedance of the DAQ seen by the Rogowski coil, which is mostly resistive and large. In [28], this model based on the electromagnetic transient program (EMTP) [29] concepts has been verified through laboratory experiments. The parameters of the Rogowski coil used in the experimental unit were used in simulation study.

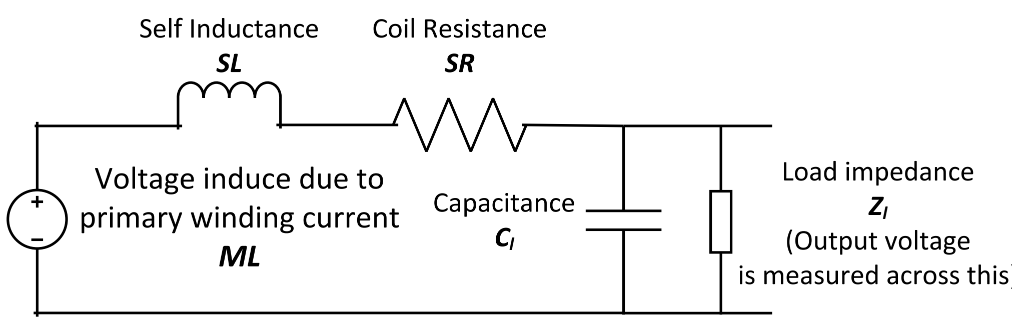

Fig. 6-29 - Equivalent circuit of the Rogowski coil

6.6.3 Simulation results

The surge capacitor currents when a permanent dc line fault occurred at 1 km away from the rectifier terminal are shown in Fig. 6-30. This can be considered as a worst case scenario since the fault occurred close to one terminal and the travelling-wave arriving at the far end (in this case the inverter terminal) is subjected to an immense amount of attenuation. Thus the magnitude of the inverter side surge capacitor currents is significantly smaller than that at the rectifier end, and the surge capacitor current itself cannot be used to obtain the surge-arrival time with sufficient accuracy. Therefore application of a signal conditioning method such as CWT or use of a suitable transducer such as a Rogowski coil is required to enhance the visibility of the surge-arrival time.

Approximately 20 mV noise was observed in the Rogowski coil measurements during the field experiment in the Nelson River system. If a similar noise level is assumed, a signal with a magnitude significantly higher than 20 mV is needed to recognize the arrival of a wave-front. Plot (g) in Fig. 6-31 shows the variation of inverter side Rogowski coil voltage calculated with the model described in Section 6.6.2 using the inverter surge capacitor current shown in Fig. 6-30 as the input. It is clear that the peak voltage is well above 3 V. Therefore, even a dc line fault occurred that 2399 km away from the terminal is recognizable using the proposed Rogowski coil based measurement scheme.

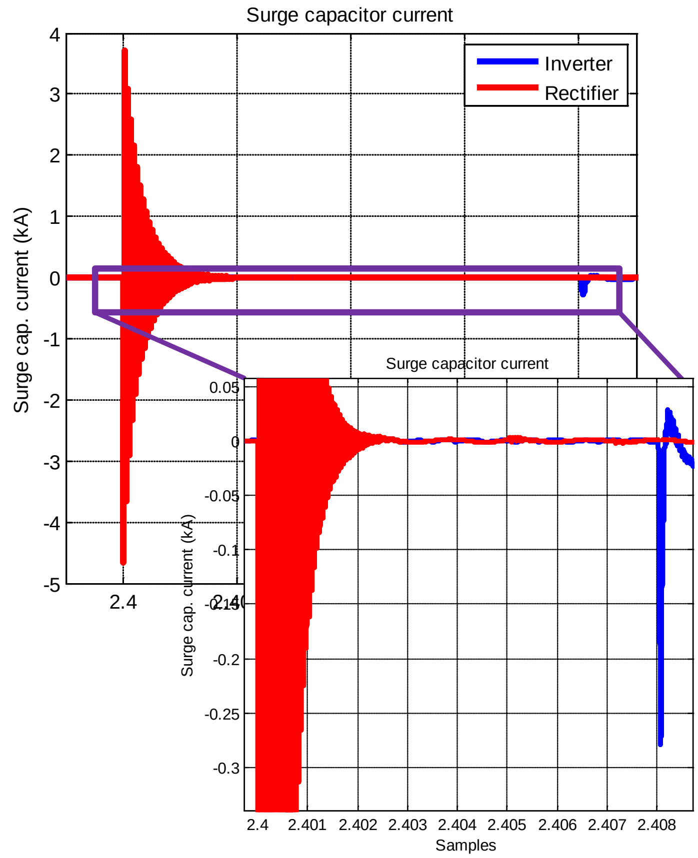

Fig. 6-30 - Surge capacitor currents after dc line fault occurred 1 km from the rectifier end. In the second graph y-axis is expanded to show the details of inverter side waveform

In Fig. 6-31, (a) to (f) plots show the variations of the continuous wavelet transform coefficient magnitude values calculated using the inverter side surge capacitor current shown in Fig. 6-30. Each coefficient (scale 2, 4, and 8) represents a different frequency band with scale 2 corresponding to the highest frequency. In Fig. 6-31, plots (g)-(h) show the variations of the magnitude of the Rogowski coil output voltages (obtained using the Rogowski coil model) for the same surge capacitor current signals. CWT coefficient values are measured in amperes and the Rogowski coil outputs are measured in voltage. However, once captured through a DAQ, the initial sharp change in these signals is used to identify the travelling-wave arrival time. Therefore, the shape of these waveforms is the most important feature with respect to travelling-wave based fault-location.

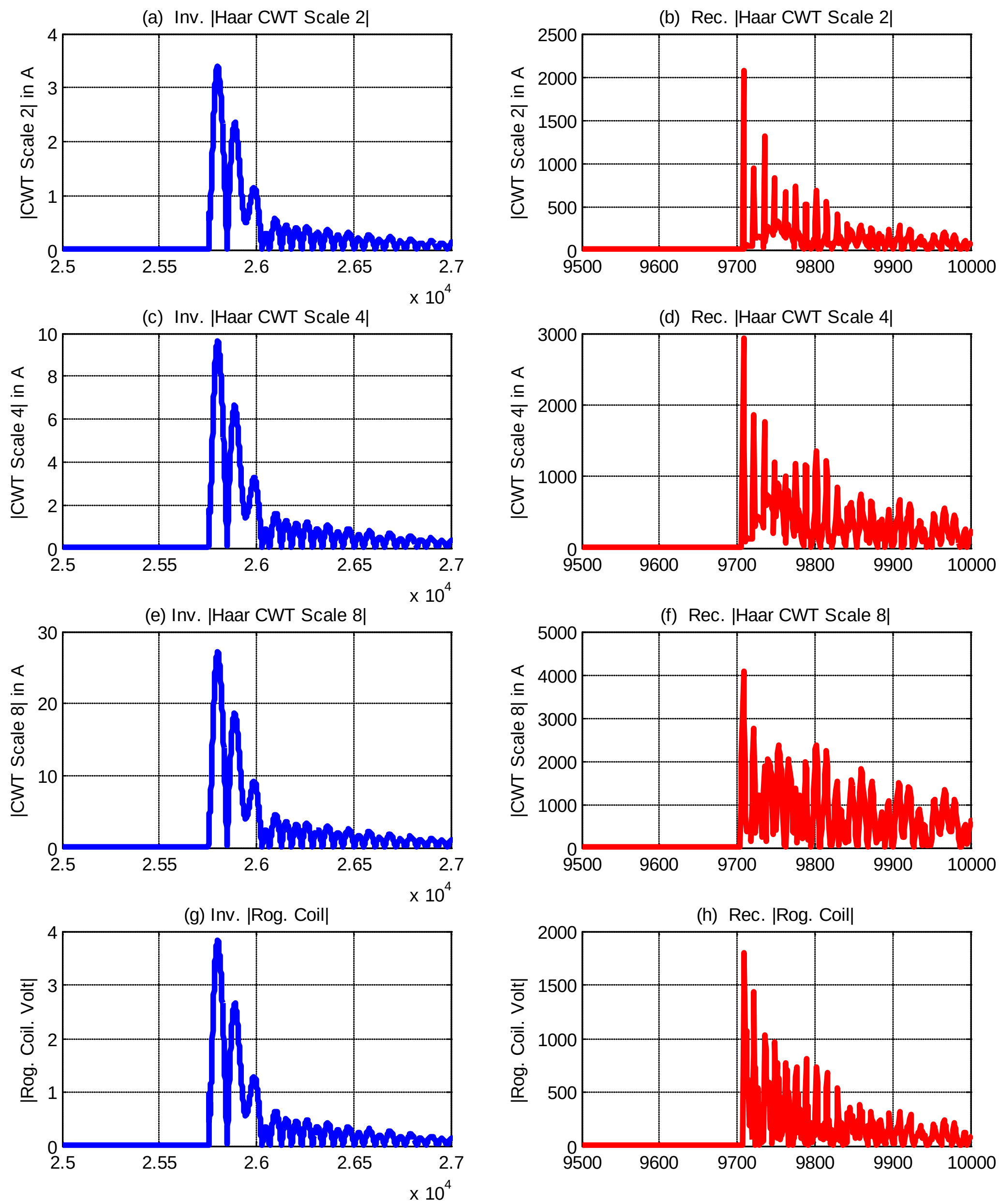

Fig. 6-31 - CWT coefficient magnitudes and Rogowski coil voltage magnitude obtained from surge capacitor currents at the terminals for ground fault occurred on the dc line 1 km from the rectifier station.

According to the observation data, it is clear that the shape of the magnitude of the Rogowski coil voltage is very similar to the wavelet coefficient magnitude variation.

6.6.4 Rogowski coil and 'Haar' wavelet transform

Rogowski coil output voltage is approximately proportional to the rate of change of surge capacitor current. When finding the Haar wavelet transform coefficients, it takes the sums and differences of every pair of numbers in the input vector and divides them by square root of 2 as described in Appendix-A. Then, the process is repeated on the resultant vector of the summed terms. Therefore coefficient value is proportional to the rate of change in the input signal for the considered scale. Thus Rogowski coil output voltage and the Haar wavelet transform coefficient magnitudes both indicate a change in the surge capacitor current.

This can be explained further using the Rogowski coil transfer function. The transfer function of the Rogowski coil can be derived using equivalent circuit shown in Fig. 6-29 as:

$$\frac{ML.Z_l.(2\pi.f.\boldsymbol{j})}{SL.C_l.Z_l.(2\pi.f.\boldsymbol{j})^2+(SL+SR.C_l.Z_l.(2\pi.f.\boldsymbol{j})+(SR+Z_l)} \qquad \text{Eq. 6-2}$$

Where, *ML* is the Mutual inductance, Z_l is the load impedance, *SL* is the self-inductance, *SR* is the coil resistance and C_l is the capacitance. The frequency response of the transfer function given in Eq. 6-2 is shown in Fig. 6-32, and as can be seen the combined characteristic of the sensor and the sampling system is approximately equivalent to a band-pass filter with 300 kHz to 1 MHz band frequency. The wavelet transform can also be considered as a band-pass filtering process, with each scale corresponding to a different pass band. For example, scale 2 responses shown in Fig. 6-31 (a) and (b) contains frequencies from 500 kHz to 1 MHz, since the sampling rate was 2 MHz. Therefore both the

Rogowski coil output and the scale-2 continuous wavelet transform coefficients contain similar frequency components in the surge capacitor currents.

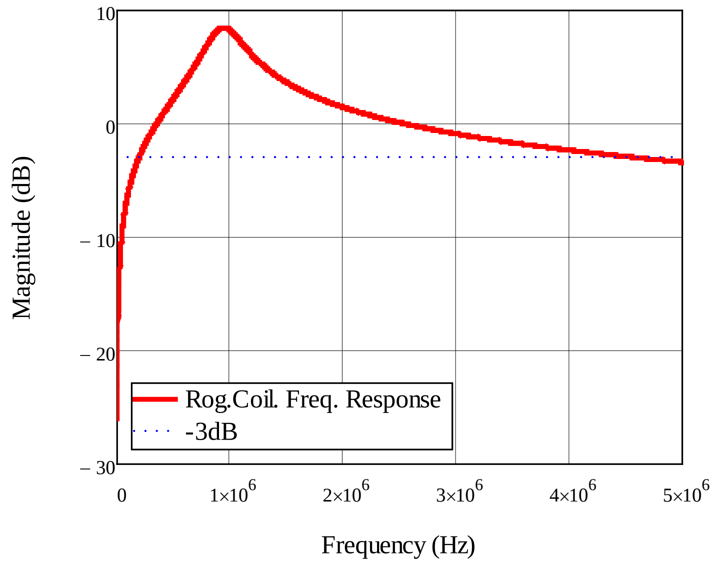

Fig. 6-32 - Frequency response of the Rogowski coil

6.6.5 Fault-location results

Table 6-5 compares the fault locations calculated using the direct Rogowski coil voltages measurements and the scale-2 CWT coefficients of the surge capacitor currents, for different line-to-ground faults on the dc line in the test network.

It is clearly seen from the results that both methods give a similar accuracy of fault-location (difference within ±50 m for the cases simulated). Thus it can be concluded that both methods provide similar results in the detection of wave-front arrival times. Therefore, if the proposed surge-arrival time measurement scheme is used, there is no need for further processing of the input signals using the continuous wavelet transform. Furthermore, the simulation shows that surge-arrival times can be detected even for an overhead transmission line as long as 2400 km, although the signals are very small.

Table 6-5 - Comparison of fault locations

Actual fault-location from Rectifier (km)	Predicted fault-location errors (meters) using different methods	
	Rog. Coil	**CWT Scale 2**
1.00	157.90	157.90
10.00	197.03	197.03
100.00	140.07	140.07
157.00	64.15	64.15
251.00	-33.52	-33.52
333.00	-9.06	-9.06
850.00	14.01	14.01
1111.00	-46.60	-46.60
1200.00	0.00	0.00
1323.00	-38.01	-38.01
1400.00	-18.68	-18.68
2040.00	-108.32	-108.32
2100.00	-121.39	-121.39
2240.00	-127.00	-127.00

6.7 Concluding remarks

This chapter demonstrated the successful application of a Rogowski coil as a transducer to identify the fault initiated travelling waves on bi-pole 1 of the Nelson River HVDC transmission line. Two experimental units were installed at the Dorsey and Radisson converter stations. It also validated DAQ specifications for this application.

Design details of the experimental DAQ system and recorded events are discussed in detail. The implemented system provided accurate fault locations for all the events recording during the period at accuracy of ± 500 m when compared with the existing fault locator. It was verified that the experimental system could detect faults that occurred on the other DC line in the same right of way. The noise in the system was lower (± 20 mV) compared to the wave-front observed in the recorded events (>3 V). The wave-fronts are clearly visible as a sharp change in voltage. The Rogowski coil voltage itself can be used to identify the wave-front arrival time using a pre-defined threshold.

A simulation model is used to validate the application of the Rogowski coil in an extra-long (2400 km) overhead transmission system. It is found that the Rogowski coil can be used to calculate the fault in an extra-long HVDC system within ±200 m accuracy. Accuracy of the results is similar to the CWT based method results. The reason for this is simulated Rogowski coil wave form magnitudes have the same waveform signatures as the CWT coefficient magnitudes. This is expected because the Rogowski coil has a similar frequency bandwidth as one of the wavelet transform coefficients.

Chapter 7

Conclusions and contributions

This chapter presents the conclusions of the research, summarizes the main contributions and proposes directions for future research in the area of HVDC line fault-location.

7.1 Conclusions

In this thesis, travelling-wave based dc line fault-location, specifically the synchronized two ended method, was investigated in detail with the objective of extending the range of applications to emerging situations such as very long transmission lines and cables, multi-segment transmission lines, and multi-terminal HVDC systems.

Recognizing the fact that the accuracy of the surge-arrival time difference measurement is the most critical aspect that influences the accuracy of fault-location, the possibility of using wavelet transform coefficients of the potential input signals to identify the arrival of travelling waves was examined through simulation studies. While the use of DWT coefficients as suggested by some previous literature can be helpful in the detection of wave fronts, the use of CWT coefficients, as proposed in this thesis, clearly results in more accurate, robust, and reliable fault-location performance compared to the DWT based methods. This is due to the fact that CWT retains the maximum time resolution regardless of the scale of coefficients, which is very important in determining the wave front arrival times.

Fault-location in extra-long dc transmission lines and cables was examined through simulations. These studies indicated that faults can be successfully located in a conventional LCC type HVDC system with a 2400 km OH line or a 300 km of UG cable, only using the terminal measurements. It was also found that both line terminal voltages and the surge capacitor currents can perform equally well as the inputs to the fault-location algorithm. The analysis considered the effects of signal conditioning, particularly the scaling of inputs to a 0-20 V range and the A/D conversion of input signals at a 2 MHz sampling rate and a 16-bit resolution.

The overall accuracy of fault-location can be improved if the appropriate propagation velocity is determined for the particular CWT scale being used, by using the data from a test fault performed at a known location. Investigation of the impact of noise showed that the accuracy of the proposed method can be reduced with the amount of noise present in the measurements. However, the impact of noise can be reduced by using CWT coefficients of higher scales (Scales 16 and 32 at 2 MHz sampling rate) without undue effect on the fault-location accuracy.

In this research, a novel algorithm was developed to locate the faults in HVDC transmission lines with multiple segments, using only the terminal measurements. A theoretical derivation of the algorithm was presented and its application was validated using a three segment (OH line/UG Cable/OH line) dc transmission system simulated in PSCAD/EMTDC. Using the proposed algorithm, it is possible to correctly identify the faulted segment as well as the exact fault-location using only the terminal measurements.

Therefore the need for installation of fault-location equipment at the segment boundaries is eliminated. Although the algorithm development and validation considered a three segment dc transmission system, the proposed fault-location algorithm can be generalized to a dc transmission system with any number of segments as long as the measurement of the surge-arrival time difference is practical.

Furthermore, a new fault-location algorithm was developed for VSC based star connected multi-terminal HVDC schemes. The proposed algorithm is also based on the travelling-wave fault-location principle and it has the ability to correctly identify the faulted line segment and fault-location using only the measurements at the converter station ends. This was validated for a 3-terminal VSC HVDC system consisting of overhead line segments through simulation studies. The proposed method eliminates the need for the installation of repeater stations at the junction of the multi-terminal HVDC network. Although derivations and simulations were carried out considering a three-terminal dc network, the concept can be expanded to general network with any number of terminals as long as surge-arrival time measurements are available at the converter stations.

Finally, an experimental measurement system was developed for identifying the arrival of fault initiated travelling waves. This measurement system that uses a Rogowski coil as a transducer was field tested on the dc line connecting Dorsey and Radisson converter stations of the Nelson River HVDC transmission system in Manitoba, Canada. The field measurements showed that the proposed measurement scheme can accurately detect the surge-arrival times, even without the post processing of the signals, in this nearly 1000 km long overhead transmission system. The noise in the practical measurements was very low (± 20 mV) compared to the magnitudes of the wave-fronts observed in the recorded events (>3 V), and the wave-fronts were clearly distinguishable. Furthermore, it was verified that the experimental system could detect the faults that occurred on a parallel dc line in the same right of way, using the induced transients. A simulation model was used to investigate the applicability of the Rogowski coil based measurement system for fault-location on an extra-long overhead transmission system. It was found through the simulation studies that the proposed measurement scheme, which directly uses the output of the Rogowski coil transducer to detect surge-arrival times, can determine the fault locations in a 2400 km long HVDC system line with a ± 200 m accuracy. This accuracy is similar to the results obtained using the CWT coefficients of the surge capacitor currents. Further analysis showed that the Rogowski coil output waveforms have a waveform signature similar to that of the CWT coefficients.

It is hoped that the outcomes of the thesis would be beneficial to the power industry, as the developed algorithms could be incorporated to enhance the capabilities of the existing dc line fault locators. The knowledge gained through the project was dispersed through scientific publications.

7.2 Contributions

Main contributions of the research are:

1. Development of an improved method to detect the travelling-wave arrival times using the continuous wavelet transform coefficients. This can improve the accuracy and reliability of travelling-wave based fault-location compared to discrete wavelet transform based method.
2. Assertion that the dc line terminal voltages and the surge capacitor currents are the most suitable input signals for detecting the travelling waves in both overhead line and cable based HVDC transmission systems that use line commutated con-

verters. The same signals will work for voltage source converter based HVDC systems if a small series reactance is present at the dc line terminals; otherwise the dc line current can be used as an input signal although measurement is practically difficult.

3. Development of a new algorithm for fault-location in classical two-terminal HVDC schemes with multiple segments of OH lines and UG cables using only the measurements at two ends. The algorithm is simple to implement and independent of the method of measurement of travelling-wave arrival times. This finding has significant potential to reduce the cost of fault-location in HVDC transmission systems with multiple segments in comparison to the current technology that uses repeater stations at segment boundaries.
4. Development of a new algorithm for fault-location in star connected multi-terminal HVDC schemes using only measurements at the converter terminals. This algorithm is also simple to implement and independent of the travelling-wave arrival time measurement method. This finding will enable efficient fault-location in multi-terminal HVDC grids that are being considered for various applications such as the harnessing of offshore wind resources.
5. Development of a robust measurement scheme for the detection of travelling-wave arrival times using Rogowski coils, and validation of its practicality through field tests in a real HVDC transmission system. .

These contributions led to the following publications in journals and conferences.

- O. M. K. K. Nanayakkara, A. D. Rajapakse, and R. Wachal, "Fault Location in HVDC Transmission Lines Using Discrete Wavelet Transform," presented at the *Cigre Canada Conference on Power Systems 2010*, Vancouver, Canada, 2010.

- K. Nanayakkara, A. D. Rajapakse, and R. Wachal, "Fault location in extra long HVDC transmission lines using continuous wavelet transform," presented at the *International Conference on Power Systems Transients* (*IPST), Delft, the Netherlands*, 2011.

- O. M. K. K. Nanayakkara, A. D. Rajapakse, and R. Wachal, “Location of dc Line Faults in Conventional HVDC Systems With Segments of Cables and Overhead Lines Using Terminal Measurements,” *IEEE Transactions on Power Delivery*, vol. 27, no. 1, pp. 279–288, Jan. 2012.

- O. M. K. K. Nanayakkara, A. D. Rajapakse, and R. Wachal, “Travelling-Wave-Based Line Fault Location in Star-Connected Multiterminal HVDC Systems,” *IEEE Transactions on Power Delivery*, vol. 27, no. 4, pp. 2286 –2294, Oct. 2012.

7.3 Suggestions for future research

This research is based on fault-location in dc lines that are used to deliver electrical power. In some HVDC systems, the grounding electrode is located at a remote destination and the operators may require the location of faults and discontinuities in the line connecting to the ground electrode. Since there is no current flowing in the electrode lines under normal operation, the methods proposed in this thesis are not applicable. Further investigations are necessary to develop suitable methods for electrode line fault-location.

With the advancement of telecommunication technology, the physical size of GPS units and DAQ systems are becoming more miniature and their accuracies are improving. Field-programmable gate array (FPGA) technology is developing at a rapid rate and there is a potential to develop compact dc line fault locators by combing a FPGA unit, a GPS unit, a wireless communication unit, and a Rogowski coil transducer into a single module which can be easily deployed in the converter station yard.

It was revealed that the Rogowski coil can be used to detect travelling waves at high accuracy in HVDC systems. Therefore Rogowski coils can be used in travelling-wave based relays as the main transducer instead of a standard current transformer. The proposed multi-terminal fault-location algorithm can be adapted to locate faults in the teed ac transmission networks.

Appendix A: Wavelet Transform

A.1 Introduction

Main challenge in travelling-wave based fault-location is the determination of the precise times of arrival of travelling waves by analyzing the high frequency content of a measured input signal. Short-Time Fourier transform (STFT) is a modified version of classical Fourier transform which uses a window function to provide time-frequency analysis. Although STFT can be used to observe singularity point in a monitored signal, there are still limitations when it comes to fault location applications due to the fixed resolution arising from the fixed width of the window function.

Wavelet transform is similar to STFT and it provides time-frequency analysis by changing the location and scaling of a mother wavelet, which is the window function in Wavelet transform. Wavelet transform can capture short-duration, high frequency and long-duration, low frequency information simultaneously and therefore useful for singularity detection with noisy signals as explained in Section 3.5.

The continuous wavelet transform (CWT) is a correlation between the analyzed signal and a wavelet at different scales and hence provides similarity between the input-signal with the mother wavelet at the scale being used. The CWT was computed by selecting the scale of the analysis window, multiplying it by the input signal, and integrating the product over the time. This is repeated after shifting the window in time by one sample time at each step, Discrete Wavelet Transform (DWT) coefficients are usually sampled from the CWT on a dyadic grid so the scaling and shifting is based on power of two. In this appendix, shape of Haar wavelet and calculation steps of the Haar wavelet transform are explained.

A.2 Haar wavelet

The Haar transform is the simplest of the wavelet transforms and it finds inner product between the input signal and the shifted and scaled versions of the Haar mother wavelet. Haar wavelet coefficients basically calculate the difference (gradient) in the input signal at each scale level. Fig. A-1 shows the Haar mother wavelet shape and its shifting process and Fig. A-2 shows a comparison of Haar wavelet shapes at scales 2, 4 and 8. Mathematical function of the Haar wavelet is shown in Eq. A-1.

$$\psi(t) = \begin{cases} 1 & 0 \le t < 1/2, \\ -1 & 1/2 \le t < 1, \\ 0 & \text{otherwise.} \end{cases} \qquad \text{Eq. A-1}$$

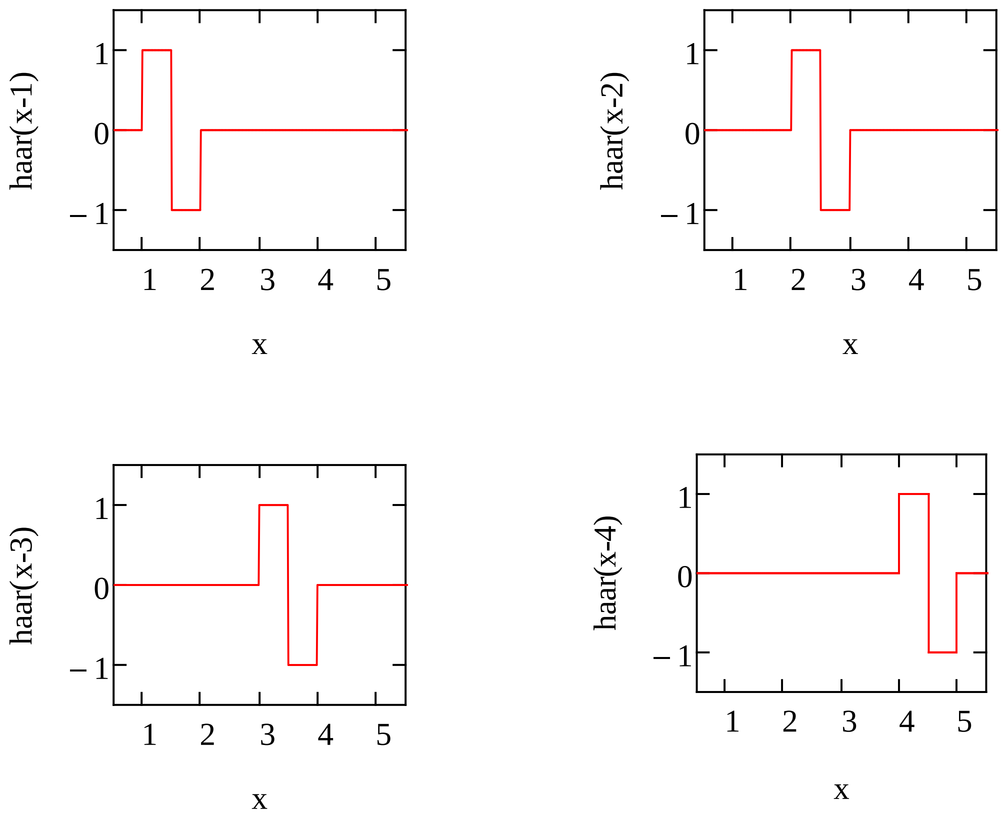

Fig. A-1 - Haar wavelet and its shifting process

As the scale goes up, the width of the Haar wavelet increases and hence the Haar wavelet transform gives lower frequency variations in the input signal. Fig. A-3 compares an example waveform of the surge capacitor current after a fault with the original Haar mother wavelet and scale 32 version of the Haar wavelet. The original Haar mother wavelet is more sensitive to sudden variations of the signal and gives more time resolution. However, it is more likely to respond to high frequency noise in the case of practical signal. On the other hand scale 32 is could be robust against high frequency noise. As the scale is increasing, the wavelet will become less sensitive to sudden changes. Thus a suitable scale-should be selected as a compromise between these two aspects.

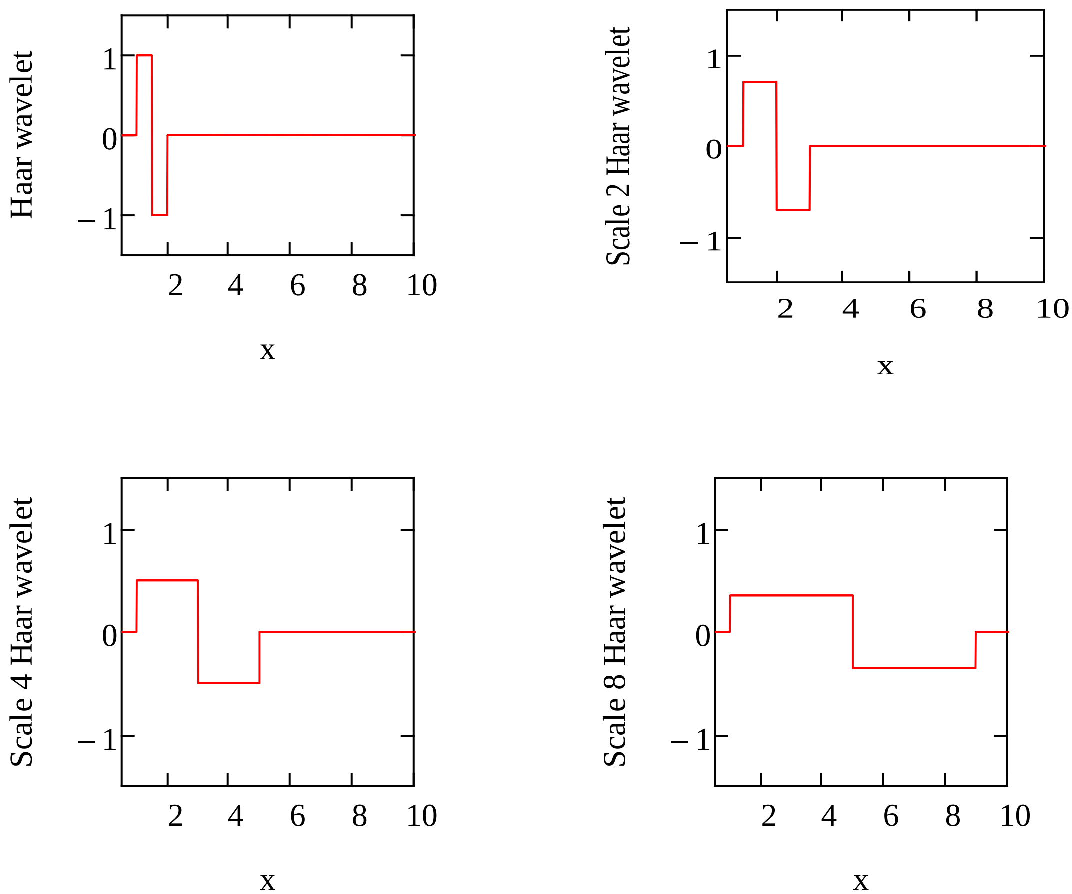

Fig. A-2 - Haar wavelets at different scales

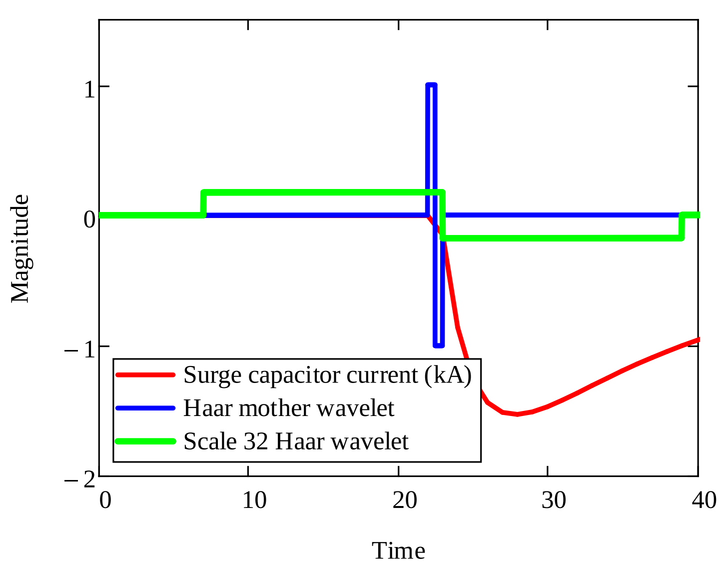

Fig. A-3 – Comparison of Haar wavelet and its scale 32 version with an example surge capacitor current signal

A.3 Example calculation of Haar wavelet coefficients

Steps to calculate *Haar* wavelet transform of an array of *n* samples is as follows:

Consider the array as *n/2* pairs with samples *i* and *i+1* together where *i* is an even sample number.

- Calculate addition of each pair (i^{th} + $(i+1)^{th}$) and divide that value by √2. These values will be the approximate coefficients.
- Calculate difference between i^{th} *and* $(i+1)^{th}$ samples for each pair and divide that value by √2. These values will be the detail coefficients.
- Consider the approximate coefficients as inputs and repeat the process to get next level of detail coefficients.

Example calculation:

The input signal is given in the first column of Table A-1 and in Fig. A-4. Following the above mentioned steps, the Haar wavelet approximate and detail coefficients (Fig. A-5) are calculated for the input signal.

Table A-1 – Example of calculated Haar wavelet coefficients

	Level 1		Level 2		Level 3
Input signal	Approximate coefficient	Detail coefficient	Approximate coefficient	Detail coefficient	Detail coefficient
1					
2	2.121320344	-0.70710678			
3					
1	2.828427125	1.414213562	3.5	-0.5	
2					
3	3.535533906	-0.70710678			
4					
0	2.828427125	2.828427125	4.5	0.5	-0.70710678

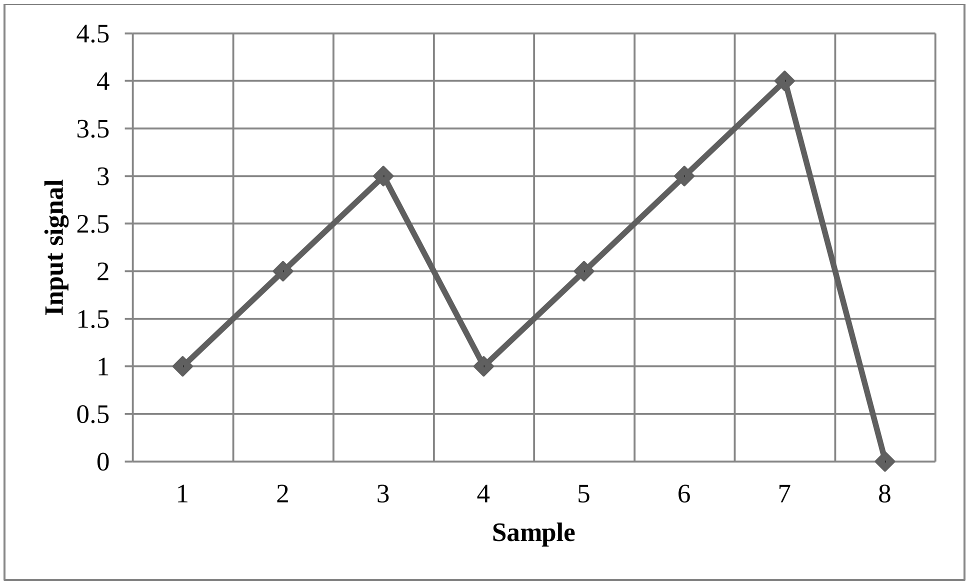

Fig. A-4 – Input signal used in example calculation

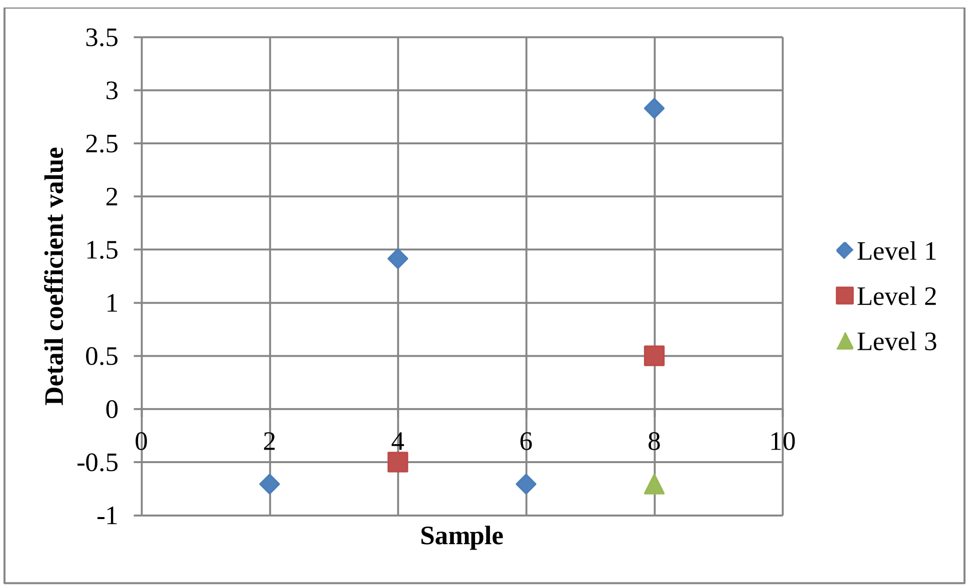

Fig. A-5 – Calculated Haar detail coefficients at 3 levels

Appendix B: Steps to set up GPS unit

B.1 Enable TIM-TM2 messages in the UART port

- As shown in Fig. B-1, set the values to the highlighted settings. This will enable UBX message time mark TIM-TM2. Therefore the time when the trigger pulse is received at external interrupt pin (Pin 4 in UART port of the GPS) is broadcasted through the UART TXD pin. (Pin 2 in UART port of the GPS)

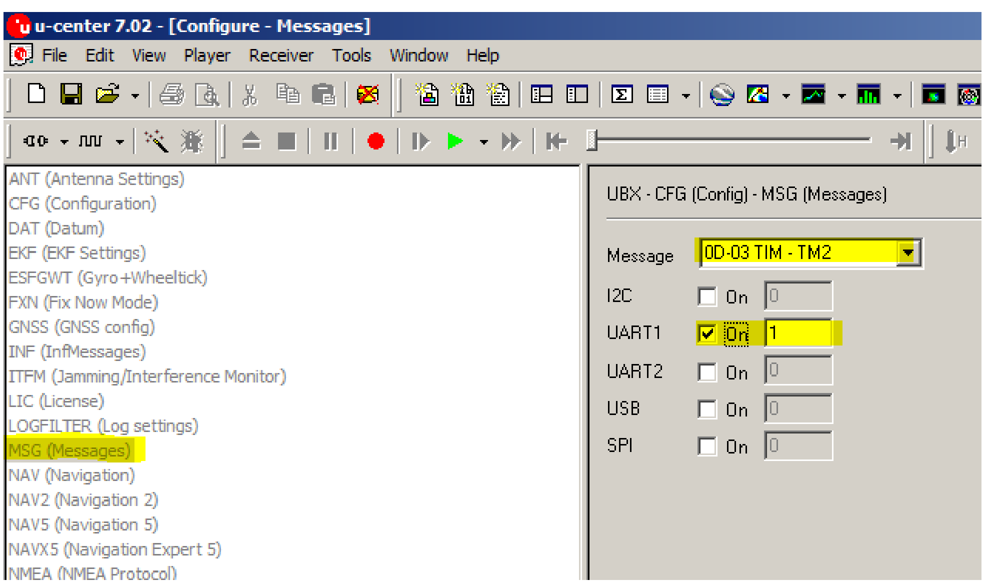

Fig. B-1 - Configure GPS message protocol

B.2 Configuration of the GPS unit's UART port data transmitting protocol settings

- Highlighted set values are used to configure the UART port as shown in Fig. B-2 .

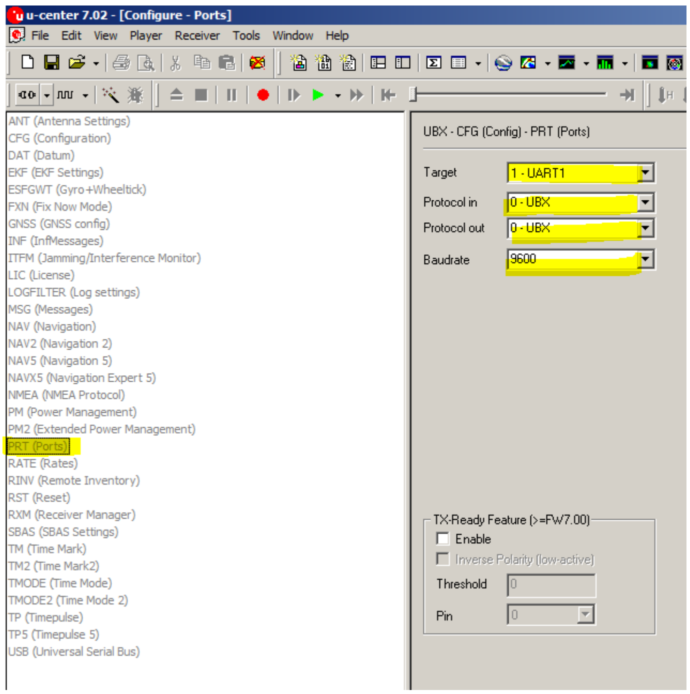

Fig. B-2 - Configure port protocol settings

B.3 Enable TIM-TM2 type messages in the GPS unit

- This message gives the time when the trigger pulse is received at the external interrupt pin (Pin 4 in UART port of the GPS).

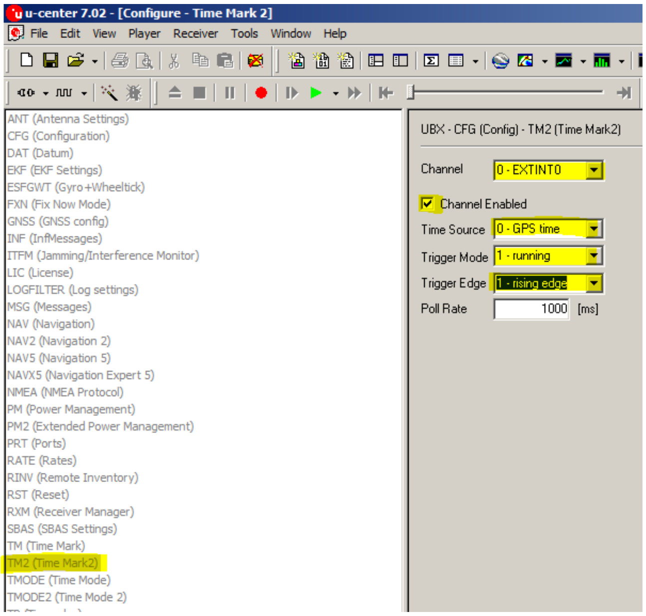

Fig. B-3 - Enable TIM-TM2 messages

B.4 Location calibration of the GPS unit

- At the installation site after mounting the GPS antenna and the unit in the field, the GPS unit needs to be calibrated for the location.

-As shown in Fig. B-3, the location of the GPS unit can be calibrated by running survey-in. Once the location is fixed the unit automatically changes the time mode to "2 - Fixed mode" and shows the fixed time mode true position (ECEF). Time taken for this process is dependent on the satellite signal strength.

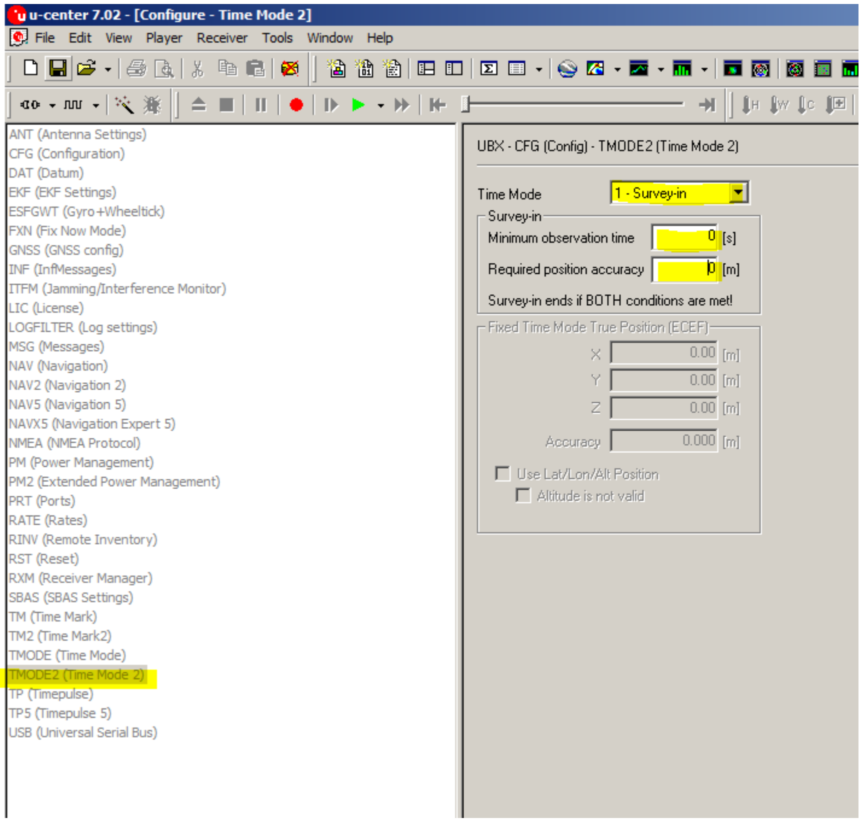

Fig. B-4- GPS survey-in

GPS time format is used in both the GPS unit and the developed software. The GPS time count began at 00:00:00 of 06 January 1980 in Coordinated Universal Time (UTC) [61]. It usually represented in week no portion and seconds portion. The U-blox GPS time mark message (TIM TM2) gives trigger time in three parts: Week No, milliseconds and nanoseconds. At the moment GPS time is ahead by 16 seconds to the UTC time [62].

References

[1] S. Patel. (2007, April), “The Age of the 800-kV HVDC,” *IEEE power & energy magazine* [Online] Available: http://www.powermag.com/issues/departments/global_monitor/The-Age-of-the-800-kV-HVDC_2450.html

[2] B. Backwell. (2009, July), “ABB wins contract for world's longest HVDC link,” *Recharge* [Online] Available: http://www.rechargenews.com/energy/wave_tidal_hydro/article184870.ece

[3] T. Westerweller and J. Price, “Crossing the divide [Basslink HVDC interconnector],” *Power Engineer*, vol. 20, pp. 42-45 , Oct. 2006

[4] “ABB NorNed - ABB HVDC Reference Projects in Europe (HVDC References),” *ABB* [Online].Available: http://www.abb.com/industries/ap/db0003db004333/4ada587c75f8d975c125774a00422545.aspx.

[5] L. Tang and B. T. Ooi, “Locating and Isolating dc Faults in Multi-Terminal dc Systems”, *IEEE Transactions on Power Delivery*, vol. 22,no. 3, pp. 1877-1884, July 2007.

[6] “ABB HVDC Light - HVDC (Power T&D Solutions),” *ABB* [Online]. Available: http://www.abb.ca/industries/us/9AAC30300394.aspx.

[7] “HVDC MaxSine® | ALSTOM GRID,” *Alstom* [Online]. Available: http://www.alstom.com/grid/products-and-services/engineered-energy-solutions/hvdc-transmission-systems/HVDC-MaxSine/

[8] “HVDC PLUS (VSC Technology) - Siemens,” *Siemens* [Online]. Available: http://www.energy.siemens.com/hq/en/power-transmission/hvdc/hvdc-plus

[9] M. G. Bennett, N.S. Dhaliwal and A.Leirbukt, “A survey of the reliability of hvdc systems throughout the world during 2009-2010,” presented at the Cigre B4 2012, Paris, France, 2012.

[10] M. D. Heffernan, J. Arrillaga, K.S. Turner and C.P. Arnold “Recovery from Temporary H.V.D.C. Line Faults,” *IEEE Transactions on Power Apparatus and Systems*, vol. PAS-100, no. 4, pp. 1864–1870, April 1981.

[11] C. W. Taylor and S. Lefebvre, “HVDC controls for system dynamic performance,” *IEEE Transactions on Power Systems*, vol. 6, no. 2, pp. 743–752, May 1991.

[12] PSE POLNOC HVDC SwePol Link, “www.pse-swepollink.pl.” [Online]. Available: http://www.pse-swepollink.pl/awariee.html.

[13] M.M. Saha, J.J. Izykowski and E. Rosolowski, *Fault location on power networks,* Springer, 2010.

[14] J. Suonan, Shuping Gao, Guobing Song, Zaibin Jiao and Xiaoning Kang, “A Novel Fault-Location Method for HVDC Transmission Lines,” *IEEE Transactions on Power Delivery*, vol. 25, no. 2, pp. 1203–1209, April 2010.

[15] M. Shukr, D.W.P. Thomas and P. Zachetta, “VSC-HVDC transmission line faults location using active line impedance estimation,” *IEEE International Conference on Energy (ENERGY CON),* pp. 244–248, Sept. 2012.

[16] M. Ramesh and A. J. Laxmi, “Fault identification in HVDC using artificial intelligence - Recent trends and perspective,” *International Conference on Power, Signals, Controls and Computation (EPSCICON),* pp. 1–6, Jan. 2012.

[17] T. Westerweller and J.J. Price, “Basslink HVDC interconnector-system design considerations,” *The 8th IEE International Conference on ac and dc Power Transmission (ACDC 2006),* pp. 121–124, 2006.

[18] S. Sasaki, “Suppression of Abnormal Overvoltages on a Metallic Return HVDC Overhead Line/Cable Transmission System,” *IEEE Transactions on Power Apparatus and Systems*, vol. PAS-94, no. 5, pp. 1925–1934, Sept/Oct 1978.

[19] L. Tang and B. Ooi, “Protection of VSC-Multi-Terminal HVDC against dc Faults”, *Power Electronics Specialists Conference* 2002, Vol. 2, pp. 719-724, 2002.

[20] T.W. Radford, “HVDC line fault locator upgrade”, in *Proc. HVDC operating conference*, pp. 189-200, 1987.

[21] P. Chen, Bingyin Xu and Jing Li, “A Travelling Wave Based Fault Locating System for HVDC Transmission Lines,” *Proceedings in PowerCon 2006 Conference*, pp. 1–4, 2006.

[22] D. Naidoo and N.M. Ijumba, “HVDC Line Protection for the Proposed HVDC Systems”, *Proc. of 2004 International Conference on Power System Technology - POWERCON 2004*, Singapore, pp. 1327-1332, Nov. 2004.

[23] M. Gilany, D.K Ibrahim and E.S.T. Eldin, “Travelling-Wave-Based Fault-Location Scheme for Multiend-Aged Underground Cable System”, *IEEE Transactions on Power Delivery*,Vol.22,no. 1, pp.82-89, Jan 2007.

[24] C. H. Lee, Y.J. Wang and W.L. Huang "A Literature Survey of Wavelets in Power Engineering Applications", *in Proceedings of Science Council, ROC (A)*, Vol. 24, pp 249-258, 2000.

[25] M.B. Dewe, S. Sankar. and J. Arrillaga "The application of satellite time references to HVDC fault location," *IEEE Transactions on Power Delivery*, vol. 8, no. 3, pp. 1295-1302, July 1993.

[26] R.A. Keswani, "Identification of Fault in HVDC Converters Using Wavelet Based Multi-Resolution Analysis," *2008 First International Conference on Emerging Trends in Engineering and Technology*, Nagpur, Maharashtra, India, pp. 954-959, 2008.

[27] P.K. Murthy, J.Amarnath, S. Kamakshiah and B.P. Singh, "Wavelet Transform Approach for Detection and Location of Faults in HVDC System," *IEEE Region 10 and the Third international Conference on Industrial and Information Systems 2008(ICIIS 2008)*, pp. 1-6, 2008.

[28] L. Shang, G. Herold, J. Jaeger, R. Krebs and A. Kumar, "High-speed fault identification and protection for HVDC line using wavelet technique," *Power Tech Proceedings 2001(IEEE Porto)*, pp. 5, vol.3, 2001.

[29] A. Borghetti, S. Corsi, C.A. Nucci, M. Paolone, L. Peretto and R. Tinarelli, "On the use of continuous-wavelet transform for fault location in distribution power systems," *International Journal of Electrical Power & Energy Systems*, vol. 28, pp. 608-617, Nov. 2006.

[30] IEEE Std C37.114-2004, "IEEE Guide for Determining Fault Location on ac Transmission and Distribution Lines", 2005

[31] F.H. Magnago and A. Abur, "Fault location using wavelets," *IEEE Transactions on Power Delivery*, vol. 13, no. 4, pp. 1475–1480, Oct 1998.

[32] M. Szechtman, T. Wess and C.V. Thio, "A benchmark model for HVDC system studies," *International Conference on AC and DC Power Transmission 1991*, pp.374-378, 17-20 Sep 1991.

[33] E.W. Kimbark, *Direct Current Transmission*, Vol. 1, John Wiley & Sons, 1971.

[34] T. Westerweller and J.J. Price "Basslink HVDC interconnector-system design considerations," *The 8th IEE International Conference on ac and dc Power Transmission 2006 (ACDC 2006)*, pp. 121–124, 2006.

[35] "Atlantic Wind Connection." [Online]. Available: http://atlanticwindconnection.com.

[36] H. Jiang and A. Ekstrom, “Multiterminal HVDC systems in urban areas of large cities,” *IEEE Transactions on Power Delivery*, vol. 13, no. 4, pp. 1278–1284, Oct. 1998.

[37] J. Zhu and C. Booth, “Future multi-terminal HVDC transmission systems using Voltage source converters,” in Universities Power Engineering Conference (UPEC), 2010 45th International, pp. 1–6, 2010.

[38] S. Rajendra, and P. G. McLaren, “Travelling-wave techniques applied to the protection of teed circuits: Multi-phase/multi-circuit system,” *IEEE Transactions on Power Apparatus and Systems*, vol. 104, no. 12, pp. 3351–3557, Dec. 1985.

[39] O. Gomis-Bellmunt, Jun Liang, Janaka Ekanayake, Rosemary King and Nicholas Jenkins, “Topologies of multiterminal HVDC-VSC transmission for large offshore wind farms”, *Electric Power System Research*, Vol. 81, pp. 271-28, Feb. 2011.

[40] C. Y. Evrenosoglu, and A. Abur, “Fault Location for Teed Circuits with Mutually Coupled Lines and Series Capacitors,” *IEEE Transactions on Power Delivery*, vol. 20, no. 2, pp. 1115-1121, Apr. 2005.

[41] A. O. Ibe, and B. J. Cory, “A travelling wave based fault locator for two and three terminal networks,” *IEEE Transactions on Power Delivery*, vol. 1, no. 2, pp. 283–288, Apr. 1986.

[42] Z. Galijasevic and A. Abur, “Fault area estimation via intelligent processing of fault-induced transients,” *IEEE Transactions on Power Systems*, vol. 18, no. 4, pp. 1241 – 1247, Nov. 2003.

[43] A. Elhaffar and M. Lehtonen, “Multi-End Travelling Wave Fault Location based on Current Travelling Waves”, *Power Systems Computation Conference (PSCC)*, Glasgow, Scotland, 2008.

[44] C. Nan, Zeng Xiangjun, Tang Xin, Wang Yuanyuan and Liu Zhanglei, “Software for Power Grid Fault Location with Travelling-wave,” *International Conference on Power System Technology (PowerCon) 2006*, pp. 1 –5, 2006.

[45] M. da Silva, M. Oleskovicz and D.V. Coury, “A Fault Locator for Three-Terminal Lines Based on Wavelet Transform Applied to Synchronized Current and Voltage Signals,” in *Transmission Distribution Conference and Exposition: Latin America, TDC ’06*. IEEE/PES, pp. 1 –6, 2006.

[46] K. P. A.N. Pathirana, A. Rajapakse, K. Nanayakkara and R. Wachal, “Detecting fault generated surges in dc line of VSC HVDC schemes for travelling wave based

fault location," *presented at the 2012 CIGRÉ Canada Conference*, Montréal, Québec, Canada, Sep. 2012.

[47] P. F. Gale, P.V. Taylor, P. Naidoo, C. Hitchin and D. Clowes, "Travelling wave fault locator experience on Eskom's transmission network," *Seventh International Conference on (IEE)Developments in Power System Protection*, pp. 327 –330, 2001.

[48] L. A. Kojovic, "Rogowski sensor for power grid travelling wave based fault location," *IET 9th International Conference on Developments in Power System Protection (DPSP 2008)*, pp. 438 –443, 2008.

[49] Z. S. Zhang, D.M. Xiao and Y. Li, "Rogowski air coil sensor technique for on-line partial discharge measurement of power cables," *IET Science, Measurement Technology*, vol. 3, no. 3, pp. 187 –196, May 2009.

[50] X. Minjiang, Gao Houlei, Zhao Baoguang, Wang Chengzhang and Tian Chun, "Analysis on transfer characteristics of Rogowski coil transducer to travelling wave," *2011 International Conference on Advanced Power System Automation and Protection (APAP)*, vol. 2, pp. 1056 –1059, 2011.

[51] D. E. Shepard and D. W. Yauch, *An Overview of Rogowski Coil Current Sensing Technology*. Grove City, OH: LEM Dyn Amp Inc.

[52] Some Applications of Rogowski Coils, Rocoil Limited, North Yorkshire,U.K.[Online].Available: http://homepage.ntlworld.com/rocoil/Applications.pdf

[53] I. A. Metwally, "Self-Integrating Rogowski Coil for High-Impulse Current Measurement," *IEEE Transactions on Instrumentation and Measurement*, vol. 59, no. 2, pp. 353 –360, Feb. 2010.

[54] D. A. Ward and J. L. T. Exon, "Using Rogowski coils for transient current measurements", *Engineering Science and Education Journal*, vol. 2, no. 3, pp. 105 –113, Jun. 1993.

[55] L. A. Bateman, R.W. Haywood and R.F. Brooks, "Nelson River dc Transmission Project," *IEEE Transactions on Power Apparatus and Systems*, vol. PAS-88, no. 5, pp. 688 –694, May 1969.

[56] "Clamp-On Weather Proof Rogowski Coil | taehwatransus.com." [Online]. Available: http://taehwatransus.com/products/clamp-on-weather-proof-rogowski-coil/.

[57] "NI USB-6361 - National Instruments." [Online]. Available: http://sine.ni.com/nips/cds/print/p/lang/en/nid/209073.

[58] u-blox AG ,"u-blox 5 NMEA, UBX Protocol Specification.". [Online]. Available: http://elmicro.com/files/sparkfun/u-blox5_protocol_specifications.pdf

[59] u-centre GPS evaluation software, u-blox AG. [Online]. Available: http://www.u-blox.com/images/Support/Support_Products/EvaluationSoftware/u-centersetup-7.0.2.1.zip

[60] u-blox AG , "EVK-6 evaluation kits." [Online]. Available: http://www.u-blox.com/en/evaluation-tools-a-software/gps-evaluation-kits.html.

[61] "GPS Week Number Rollover — Naval Oceanography Portal." [Online]. Available: http://www.usno.navy.mil/USNO/time/gps/gps-week-number-rollover.

[62] "GPS Information: SA, DGPS, Leap Seconds, etc. — Naval Oceanography Portal." [Online]. Available: http://www.usno.navy.mil/USNO/time/gps/gps-information-sa-dgps-leap-seconds-etc.

[63] Microhard Systems Inc.,"IPn3G." [Online]. Available: http://www.microhardcorp.com/brochures/IPn3G.Brochure.Rev.2.31.pdf

[64] "Intel® Atom™ N450/D510 High Value Fanless Embedded Box PC with 3 GigaLAN and Isolated COM Ports - ARK-3000 Series: High Performance Fanless Embedded Box PCs - Advantech." [Online]. Available: http://www.advantech.com/products/ARK-3360F/mod_DB130BFD-5684-4598-B1BC-01877C5F8160.aspx#

[65] Manitoba HVDC Research Centre, Winnipeg, Manitoba, Canada [Online]. Available: https://hvdc.ca

[66] Wikipedia contributors, "Nelson River DC Transmission System," Wikipedia, the free encyclopedia. Wikimedia Foundation, Inc., 11-Aug-2012. [Online]. Available: http://en.wikipedia.org/wiki/Nelson_River_DC_Transmission_System